AD_____

Award Number: W81XWH-08-1-0365

TITLE: Onboard SPECT for Localizing Functional and Molecular Targets in Metastatic Breast Cancer

PRINCIPAL INVESTIGATOR: Justin R. Roper

CONTRACTING ORGANIZATION:
Duke University
Durham, NC 27710

REPORT DATE:
August 2010

TYPE OF REPORT:
Final

PREPARED FOR: U.S. Army Medical Research and Materiel Command
Fort Detrick, Maryland 21702-5012

REPORT DOCUMENTATION PAGE

Form Approved
OMB No. 0704-0188

1. REPORT DATE *(DD-MM-YYYY)*	**2. REPORT TYPE**	**3. DATE COVERED** *(From - To)*
30/07/2010	Final	01/07/2008 - 30/06/2010

4. TITLE AND SUBTITLE
Onboard SPECT for Localizing Functional and Molecular Targets in Metastatic Breast Cancer

5a. CONTRACT NUMBER

5b. GRANT NUMBER
W81XWH-08-1-0365

5c. PROGRAM ELEMENT NUMBER

6. AUTHOR(S)
Justin R. Roper

5d. PROJECT NUMBER

5e. TASK NUMBER

5f. WORK UNIT NUMBER

7. PERFORMING ORGANIZATION NAME(S) AND ADDRESS(ES)

Duke University
Durham, NC 27710

8. PERFORMING ORGANIZATION REPORT NUMBER

9. SPONSORING / MONITORING AGENCY NAME(S) AND ADDRESS(ES)
U.S. Army Medical Research and Materiel Command

Fort Detrick, Maryland 21702-5012

10. SPONSOR/MONITOR'S ACRONYM(S)

11. SPONSOR/MONITOR'S REPORT NUMBER(S)

12. DISTRIBUTION / AVAILABILITY STATEMENT
Approved for public release; distribution unlimited

13. SUPPLEMENTARY NOTES

14. ABSTRACT

The overall goal of this work is to assess the potential performance characteristics of using single photon emission computed tomography (SPECT) for imaging inside radiation therapy treatment rooms to localize functional & molecular targets associated with metastatic breast cancer. The first aim is to evaluate localization accuracy and precision as a function of scan time, tumor size, tumor-to-background uptake ratio, and background non-uniformity. This aim was addressed using computer-simulation and hardware studies. The second aim involves the localization of breast metastases in lung. Through computer simulations, we studied localization performance of tumors in the lungs and other sites as a function of spatial resolution modeling, observer normalization, iteration number, and post-reconstruction smoothing. Localization errors were also analyzed for directional dependencies in relation to the detector trajectory.

15. SUBJECT TERMS
SPECT, Radiation Therapy, Onboard Imaging, Target Localization

16. SECURITY CLASSIFICATION OF:			**17. LIMITATION OF ABSTRACT**	**18. NUMBER OF PAGES**	**19a. NAME OF RESPONSIBLE PERSON**
a. REPORT	**b. ABSTRACT**	**c. THIS PAGE**			USAMRMC
U	U	U	UU	75	**19b. TELEPHONE NUMBER** *(include area code)*

Table of Contents

Introduction

The overall goal of this work is to assess the potential performance characteristics of using single photon emission computed tomography (SPECT) for imaging inside radiation therapy treatment rooms to localize functional & molecular targets associated with metastatic breast cancer. The first aim is to evaluate localization accuracy and precision as a function of scan time, tumor size, tumor-to-background uptake ratio, and background non-uniformity. This aim was addressed using computer-simulation and hardware studies. The second aim involves the localization of breast metastases in lung. Through computer simulations, we studied localization performance of tumors in the lungs and other sites as a function of spatial resolution modeling, observer normalization, iteration number, and post-reconstruction smoothing. Localization errors were also analyzed for directional dependencies in relation to the detector trajectory. Proposed studies on respiratory gating and the use of compact detectors are incomplete.

Body

Specific Aim 1: Evaluate localization accuracy and precision as a function of scan time, tumor size, tumor-to-background uptake ratio, and background non-uniformity.

This aim was addressed by assessing localization performance using (1) computer simulations and (2) a hardware study with a whole-body phantom and a clinical SPECT scanner.

(1) Computer-simulation study

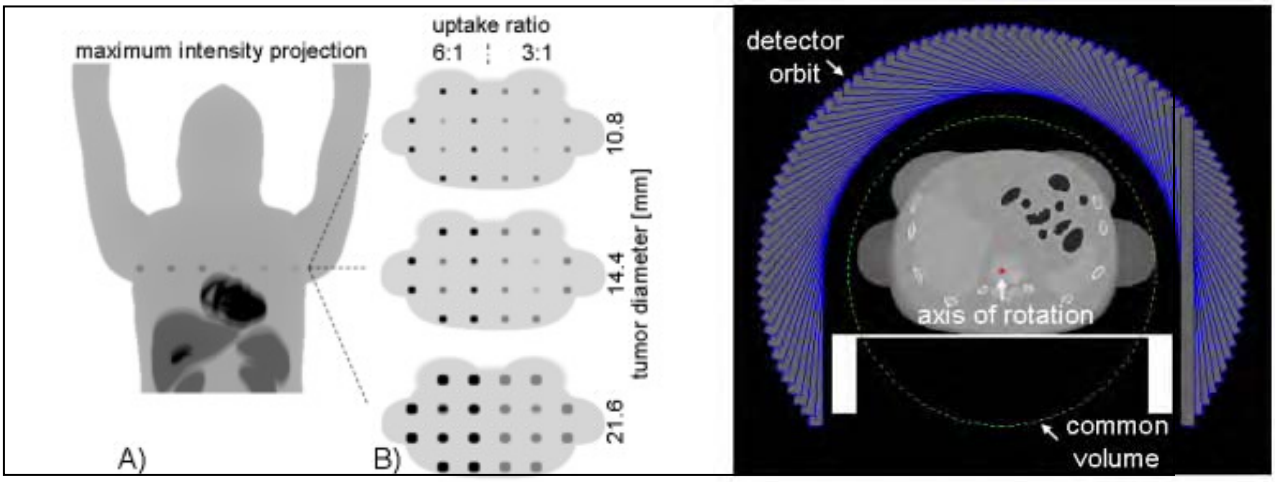

Fig.1. Activity distribution (LEFT) simulating ^{99m}Tc-sestamibi with tumors located in a transaxial slice superior to the heart. Three tumor diameters and two uptake ratios were investigated. (RIGHT) Attenuation map for 140 keV photons from ^{99m}Tc shown with anterior half-circular detector orbit [1].

Tumors were simulated with various diameters – 10.8, 14.4 and 21.6 mm – and with uptake ratios of 3:1 and 6:1 relative to background and were located in bone, lung and soft tissue of a female NCAT phantom (Fig. 1). These tumor sizes have been observed clinically, and the uptake ratios are based on breast cancer imaging with Tc-99m cardiac perfusion radiotracers [2].

The 8 deepest tumors were positioned in lung and were subject to the effects of respiratory motion. The same motion vectors were applied to laterally-symmetric lung tumors in order to minimize differences other than activity uptake ratios. Background activity was non-uniform for tumors near the heart. An anterior, half-circular detector trajectory was used to avoid viewing through the flat-top treatment couch. The simulated projection images included the effects of distance-dependent spatial resolution and non-uniform attenuation. Scatter was not modeled. Projections were degraded with Poisson Noise to form ensembles of 25 independent noisy realizations for scans times of 4, 8 and 20 minutes. Images were reconstructed with attenuation correction using 6-subset, 5-iteration OSEM. Representative reconstructed images are shown in Fig. 2 from the image ensembles.

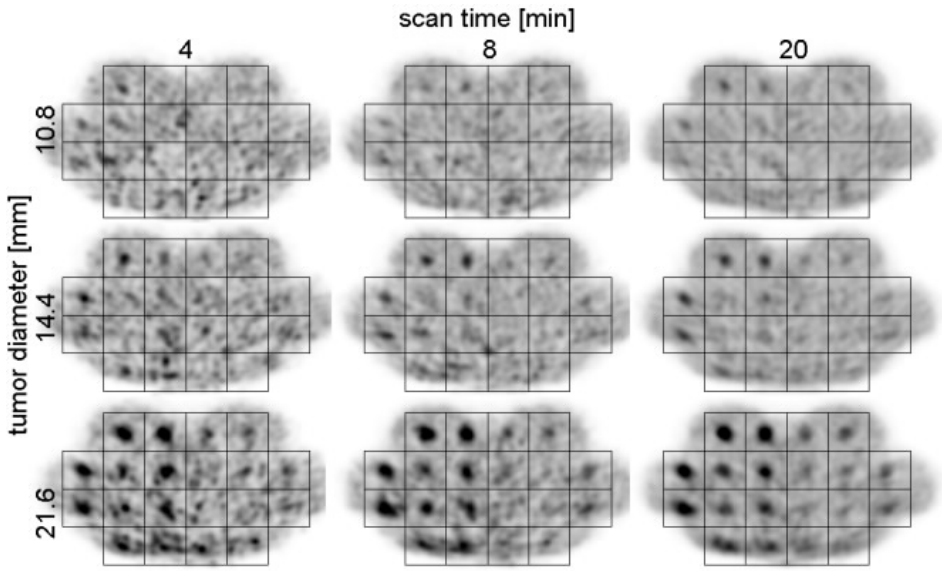

Fig. 2. Sample reconstructed images for each tumor diameter and scan time. Grids are superimposed on images such that true tumor locations are centered within the grid squares [1].

Tumors were localized using numerical observers, which had no knowledge of noise correlations, for a multiple alternative forced choice (MAFC) task where one and only one tumor was located within each 28.8-mm-diameter search volume. Observer templates were generated by blurring true tumor geometries with a 14.4-mm-FWHM Gaussian kernel, which approximates image spatial resolution. An observer was translated throughout each search volume and the location with the highest cross correlation value was selected as the measured tumor centroid. Euclidean distances between the measured and true centroid locations were computed over the image ensembles yielding estimates of mean error -- localization accuracy -- and standard deviation of error – localization precision. Estimates of localization accuracy and precision are reported in Fig. 3 for the investigated tumor diameters, anatomical locations, tumor-to-background activity ratios and scan times.

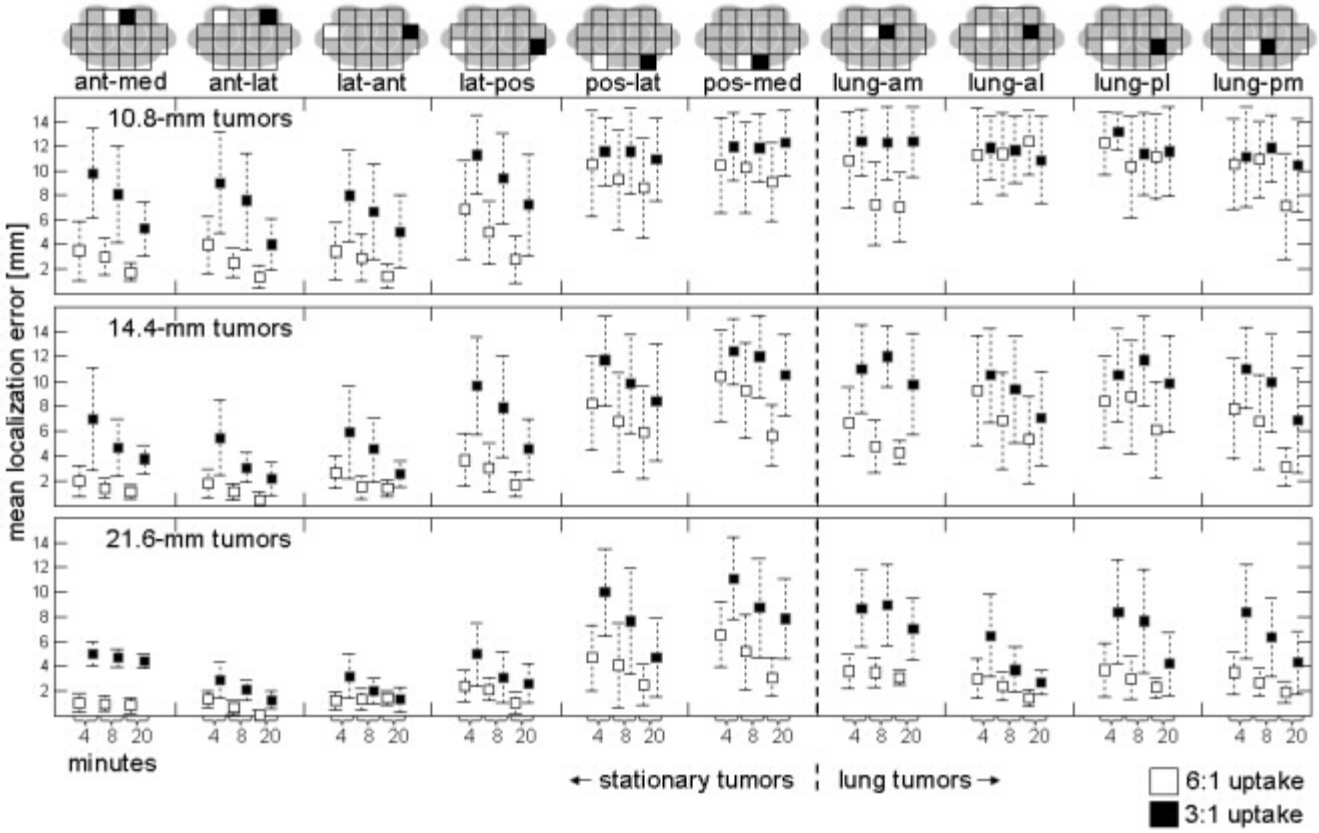

Fig. 3. Localization accuracy – boxes – and localization precision – error bars – displayed as a function of tumor size, anatomical location, tumor-to-background activity uptake ratio and scan time [1].

The results in Fig. 3 have important implications for using on-board SPECT to localize metastatic breast cancer. For stationary tumors of the same diameter and uptake ratio, localization accuracy varied substantially depending on tumor location relative to the detector trajectory. Localization accuracy was vastly better in the chest wall than near spine. These differences are due to the effects of attenuation and distance-dependent spatial resolution. Because of the anterior detector trajectory, relatively fewer counts from tumors near the spine escaped the phantom, and those that did escape were blurred over a larger number of detector bins as compared with counts from tumors near the chest wall. While the investigated half-circular detector trajectory yields highly variable localization values and does not appear to be a one-size-fits-all acquisition strategy, it is important to note that the task of on-board SPECT likely would not be to image a large volume, e.g., the upper torso. Instead the task would be to image a relatively small region near tumor. Since tumor location is known approximately from treatment planning images, detector trajectories could be customized for certain anatomical locations to minimize the effects of attenuation and distance-dependent spatial resolution. Further research is needed to determine impact of custom detector trajectories on target localization, given the constraints of the treatment couch, particularly for posterior tumors where localization was generally poor using an anterior detector trajectory.

Results from Fig. 3 also demonstrate the importance of radiotracer specificity. Tumors in laterally-symmetric anatomical locations differed primarily by tumor-to-background activity ratios. For those tumors where SPECT was useful for localization, tumors of 6:1 uptake were typically localized as well using 4-minute scans as tumors of 3:1 uptake using 20-minute scans. Because short imaging times are necessary to minimize patient motion and for machine throughput, radiotracers with a high differential uptake between tumor and nearby healthy tissue would be most appropriate for on-board SPECT imaging. Additionally, treatment planning SPECT images could be used to estimate tumor-to-background activity ratios to determine which patients might benefit from on-board SPECT guided radiation therapy. Planning images can also be used to estimate tumor geometry, another important criterion for patient selection since localization accuracy is strongly related to tumor diameter, as shown in Fig 3.

Non-uniform background activity from the heart proved challenging for localizing tumors of 3:1 uptake in the medial chest wall. These tumors are denoted by black boxes in the first column of Fig 3. For the 21.6-mm-diameter tumors, error bars are much smaller than the total error, demonstrating a bias that can be visualized in reconstructed images. Apparent tumor activity is suppressed inferiorly near the heart and causes the measured tumor centroid to shift superiorly. Additional research is needed to improve target localization near hot background objects.

Localization was generally poor in the lungs, and further work is needed to investigate the impact of respiratory gating on localization. As expected, localization accuracy and precision usually improved with increasing scan time. For the shortest scan time, certain results from this simulation study were encouraging. Localization accuracy was within 2 mm for anterior tumors of 6:1 uptake that were 14.4 mm or larger in diameter using 4-minute scans. This scan time is compatible with limited-fraction, high-dose-per-fraction therapies like stereotactic body radiation therapy where additional time is allowed for patient positioning.

Further details pertaining to this study may be found in the published manuscript [1], which is located in Appendix B.

(2) Hardware study

In related SPECT studies, scatter has been shown to degrade observer performance in the detection of hot tumors in unknown locations [3]. The above computer-simulation study did not model scatter in the phantom or detector [1]. In this present study, localization performance was assessed in scanner-acquired SPECT images that inherently include scattered photons because of limited energy resolution. This study is important for gauging the degree of localization that can be achieved with a currently available SPECT detector. Also investigated in this study are the effects of the detector trajectory on localization performance.

The hardware phantom consisted of five fillable spheres – targets labeled A-E – that were placed in a single 40-cm section of the Extended Oval PET Phantom [Data Spectrum, Hillsborough, N.C.] as shown in Fig 4. Inner dimensions of the whole-body phantom were 34 cm laterally and 19 cm anterior-posteriorly, with a 1-cm-thick Acrylic wall. Spherical targets were weighed before and after filling, and by assuming a density of 1 g/cm^3, the inner diameters of targets A-E were calculated as 2.8, 2.8, 3.4, 3.4, and 2.2 cm. Target-to-background Tc-99m radioactivity ratio was 6:1 and is based on clinically observed tumor-to-background activity uptake in breast cancer using cardiac perfusion radiotracers [2].

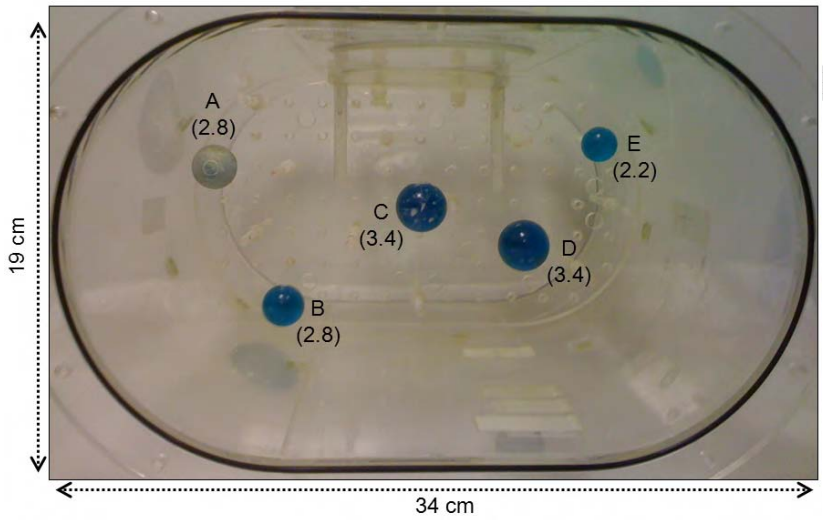

Fig. 4. Shows the whole-body phantom and five fillable spheres labeled A-E. Inner diameters of the spheres are reported in (cm).

As shown in Fig 5, the phantom was imaged using one detector of a Trionix Triad SPECT scanner. The detector was equipped with low energy, ultrahigh resolution (LEUR) parallel-hole collimation. The LEUR collimator holes were 1.4 mm in diameter by 34.9 mm in length. A photopeak window for ^{99m}Tc was centered on 140 keV +/- 10.0%. Projection images were acquired every 2° in step-and-shoot mode and implemented on a 256 x 128 grid of 1.78 x 1.78 mm^2 bins.

Fig. 5. The whole-body phantom was imaged by one detector on a Trionix Triad SPECT scanner using LEUR parallel-hole collimation.

Three noncircular detector trajectories were investigated – left lateral 180°, 360°, and right lateral 180° as illustrated in Fig 6 – that contour to the phantom and couch, thereby achieving better spatial resolution than is possible with a non-conformal circular detector trajectory.

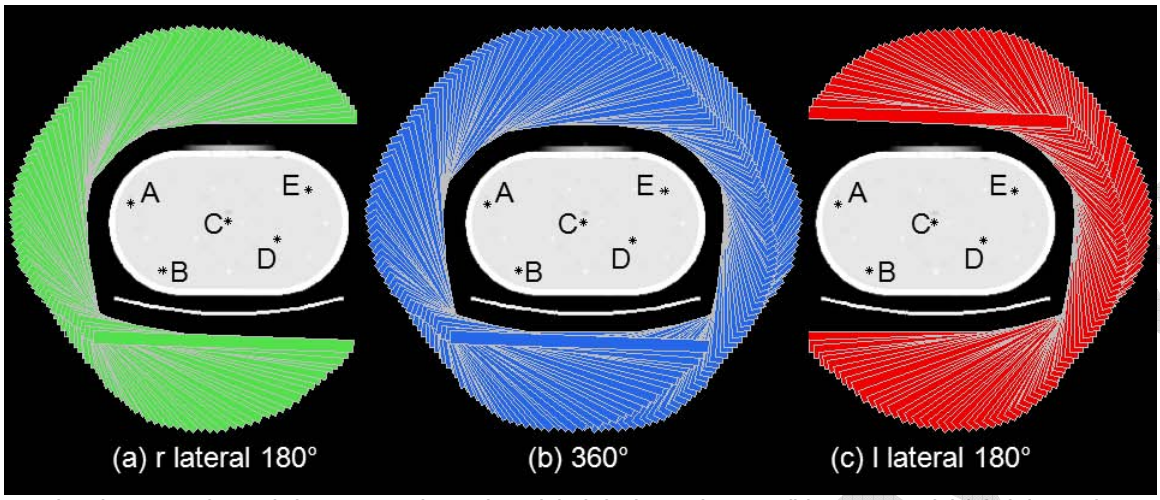

Fig. 6. Shows the three conformal detector trajectories: (a) right lateral 180°, (b) 360°, and (c) left lateral 180°

Scan time was equivalent for these detector trajectories. The scan time was adjusted as the radioactivity decayed to maintain the equivalent of a 4.5-minute clinical scan for a background activity level of 0.25 μCi/ml. In regions of the detector illuminated by background activity, approximately 7 photons were detected in the photopeak window every second per cm^2. The modeled scan time does not include the time spent rotating the detector, and thus models the number of counts expected from list-mode acquisition, which could be implemented for on-board SPECT imaging. Ten independent scans were acquired for these trajectories. SPECT images were reconstructed on a grid of 1.78 x 1.78 x 1.78 mm^3 voxels using MLEM without corrections for attenuation, distance-dependent spatial resolution, or scatter.

To determine localization error, the true position of a target must be known. In this study, the true positions of targets A-E were estimated from CT and 12-hour SPECT images. In the CT image, regions of interest (ROIs) were placed on the spheres. Intensity thresholds were used to segment air, water, and sphere wall. Target was defined as sphere wall and internal water, excluding air pockets. The center of mass was calculated for each target and was used as an estimate of true target position on the CT grid. Fig 7a shows the CT image and the segmented targets averaged over several axial slices. In a 12-hour SPECT image, ROIs were placed on targets A-E. Background activity was estimated from proximate slices and subtracted from each ROI. Target appearance in SPECT images is distorted by distance-dependent spatial resolution, non-uniform attenuation, and scatter. Due to these effects, it was challenging to select an optimal intensity threshold based on visual inspection to differentiate target from background. To address this challenge, target positions in SPECT were estimated using a broad range of intensity thresholds. Fig 7b shows the 12-hour SPECT image and the targets after background subtraction and intensity thresholding.

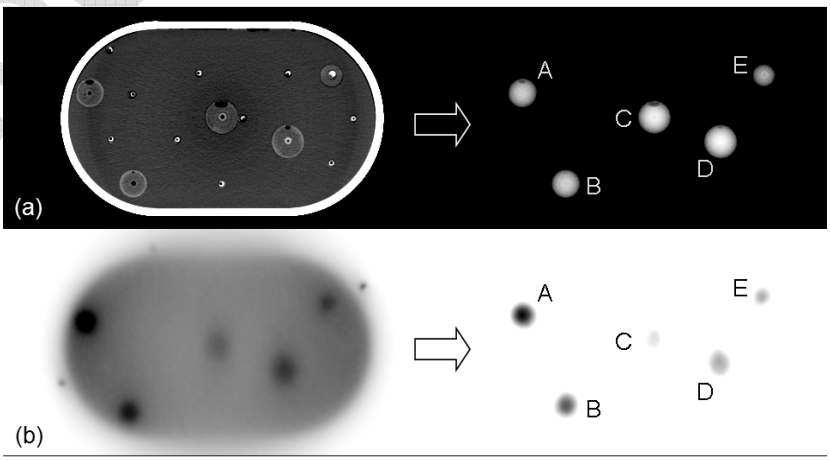

Fig. 7. True target positions were derived from CT and 12-hour SPECT images

The CT- and SPECT-based target positions – 5 pairs of 3D coordinates – were rigidly registered using Horn's closed-form, least-squares method [4]. The SPECT-based position estimates with the lowest residual errors were considered the truth in subsequent assessments of localization performance in the 4.5-minute SPECT images.

Target attenuation and distance to the collimator were calculated for all detector views in each detector trajectory. Attenuation was estimated from the CT image by segmenting air, water, and Acrylic and by assigning 140 keV linear attenuation coefficients of 0.0, 0.155, and 0.176 cm^{-1} respectively to these materials. Attenuation survival probability was defined as the fraction of photons from a target directed towards the detector that were not attenuated by the phantom or couch. Distance was calculated from a target centroid to the patient-side surface of the collimator along a ray perpendicular to the detector surface. These metrics – related to the number of target counts and collimator spatial resolution – were used in subsequent comparisons of localization performance between detector trajectories.

Target localization was assessed in the 4.5-minute-equivalent SPECT images using a numerical observer. Observer templates were binary spheres of the same diameters as the targets. The numerical observer searched 36-mm-diameter volumes, each containing only one target, and selected the location with the highest cross correlation value. Localization error was the distance between the target position estimated by the numerical observer and the target position determined from the 12-hour SPECT and CT images.

Fig. 8 shows SPECT images from the three detector trajectories: right lateral 180°, 360°, and left lateral 180°. A target is most readily visible in an image corresponding to the most proximal detector trajectory, i.e., targets A and B in right lateral 180° and targets D and E in left lateral 180°. Hot focal activity near the phantom surface is attributable to external fiducial markers not used in this analysis.

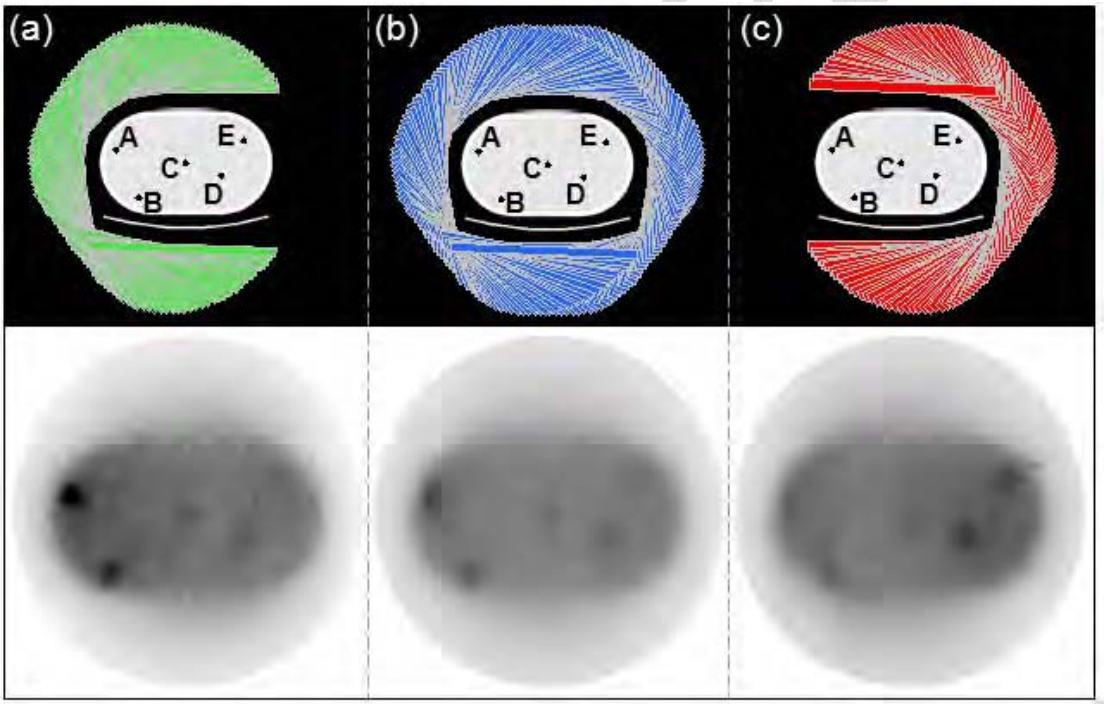

Fig. 8. Detector trajectories and corresponding SPECT images: (a) right lateral 180°, (b) 360°, and (c) left lateral 180°. For display purposes, images were summed over the axial slices containing at least one target.

In Fig 9, attenuation survival probability and distance to the collimator are summarized by two sets of curves, each indexed by the detector angle. Curves on the top row show the distance between the collimator and a target. Smaller values indicate better spatial resolution. A series of filled curves in the bottom row show the fraction of photons originating from the center of a target that are not attenuated by the phantom or SPECT couch. The area under these curves is proportional to number of tumor counts for a particular detector trajectory.

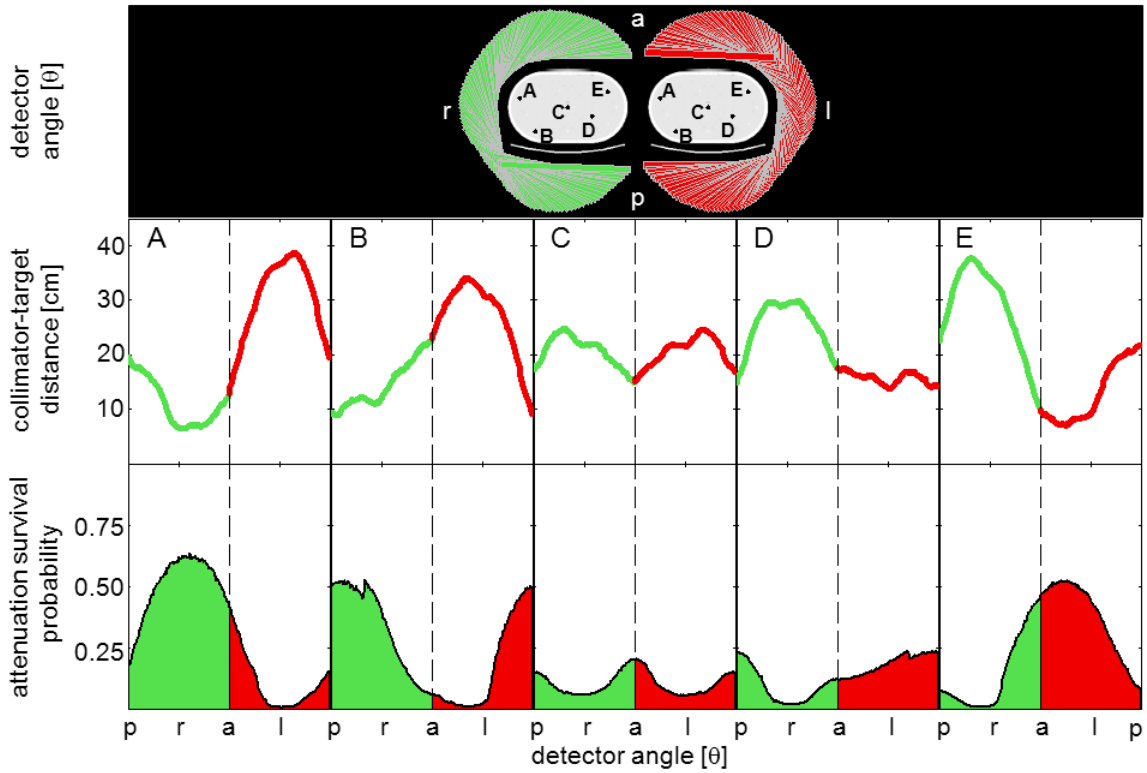

Fig. 9. Collimator-target distance and attenuation survival probability are plotted as function of the detector angle and are color-coded by detector trajectory.

The distance and attenuation results displayed in Fig 9 were averaged over each detector trajectory and are reported in Table 1. Target C was centered in the phantom such that mean attenuation survival probability and distance to the collimator were equivalent for each trajectory. For the other targets, a proximal 180° trajectory yielded the lowest collimator-target distances and the highest photon survival probabilities, followed by 360° and then distal 180° trajectories.

Table 1: Mean target-collimator distance and attenuation survival probability for each detector trajectory.

	Mean Target-Collimator Distance [cm]			Mean Attenuation Survival Probability		
Target	R 180°	360°	L 180°	R 180°	360°	L 180°
A	11	21	30	0.51	0.31	0.11
B	14	21	27	0.34	0.25	0.17
C	21	21	21	0.10	0.10	0.10
D	26	21	16	0.09	0.13	0.18
E	29	21	13	0.14	0.26	0.38

Localization errors were estimated across 10 SPECT images. Results are displayed in Fig 10 using box plots. Filled rectangles include data within the 25th and 75th percentiles. Outliers are marked by filled circles. The Wilcoxon rank-sum test was used to assess for statistical significance in localization differences between proximal 180° and 360° trajectories. The symbol * indicates p-value < 0.05.

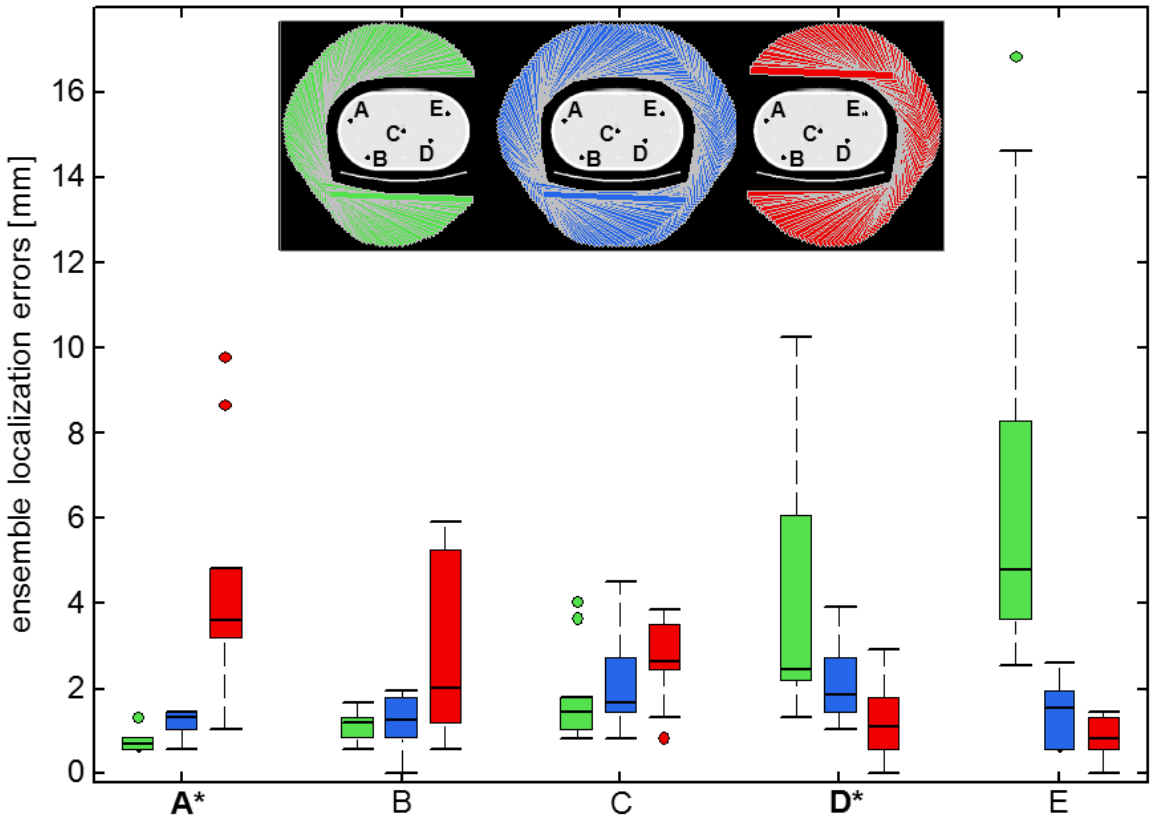

Fig. 10. Ensemble localization errors – estimated from images with optimal smoothing and iteration number – are summarized by box plots and color-coded to the detector trajectory. The symbol * indicates that localization was significantly better using a proximal 180° as compared with a 360° trajectory.

Localization errors were lowest for right-sided targets A and B using the right lateral 180° trajectory, were slightly larger with the 360° trajectory, and were the highest and substantially so with the left lateral 180° trajectory. Similarly for left-sided targets D and E, localization errors were lowest using the left lateral 180° trajectory and were highest for the right lateral 180° trajectory. These results demonstrate that localization was best using proximal 180° trajectories. Localization differences between proximal 180° and 360° trajectories were statistically significant at A and D with p-values of 0.004 and 0.049, respectively. Using a proximal 180° trajectory, mean localization error was within 1.1 mm for A, B, D, and E. The worst localization errors across the 10 images were within 2 mm for targets A, B, and E. These results demonstrate that a commercially available SPECT detector can provide useful information for localizing certain targets given the time constraints of treatment room imaging.

This study also demonstrates that parallel-hole SPECT is better for localizing superficial targets than deep targets. The volumes of deep targets C and D were 1.8 to 3.7 times larger than superficial targets A, B, and E; however, mean localization errors of the deep targets were on average almost twice that of superficial targets when using a proximal 180° trajectories. Though beyond the scope of this study, the challenge of imaging deep targets may be addressed by using converging collimation.

Specific Aim 2: Evaluate the effect of respiratory motion on the accuracy and precision of target localization.

The computer-simulation study, described above in Aim 1, modeled respiratory motion for tumors in the lungs. Localization performance was typically poor for these tumors, as shown in Fig 3. Respiratory motion was one degrading effect but other sources of poor localization performance – attenuation and spatially-varying spatial resolution – are inherent to SPECT imaging. In light of findings from this previous study, we designed another computer-simulation study to analyze localization performance for lung (and other) tumors under ideal gating conditions, i.e., no motion, and for a scan time consistent with the constraints of treatment room imaging.

This present computer-simulation study expanded upon the previous computer-simulation study by assessing for directional and locational dependent localization errors. Also investigated were the effects of observer normalization, detector response function compensation, iteration number and post-reconstruction smoothing on localization performance. This study has been accepted for publication in the peer-reviewed journal *Medical Physics*. For additional details on this study, refer to the corresponding manuscript in Appendix C.

A female XCAT Phantom, an extended version of the NCAT Phantom [5], was implemented on a grid of 0.15 x 0.15 x 0.15 cm^3 voxels. Twelve, 1.5-cm-diameter tumors were simulated – in axilla, breast, chest wall, lung, rib, vertebra, and other soft tissues – for a broad sampling of locations deep, superficial, anterior, and posterior in an axial slice superior to the heart. Relative activity ratios were 20:6:1 for heart, tumor, and other tissues [2]. The simulated activity distribution and the 12 tumor sites labeled A-L are shown in Fig 11a,b. Respiratory and cardiac motions were not modeled. A conformal detector trajectory was defined such that for each detector view, the detector radius was adjusted to achieve 0.5-cm proximity between the patient-side surface of the collimator and the phantom or couch. The detector trajectory is illustrated in Fig 11c.

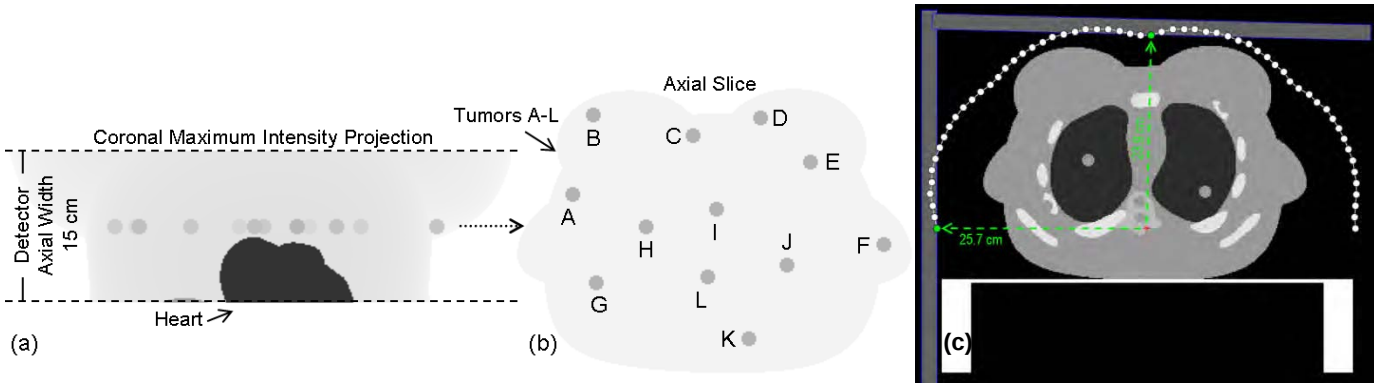

Fig. 11. (a) coronal MIP of the activity phantom, (b) axial slice containing 12 hot, 1.5-cm-diameter tumors, and (c) the detector trajectory overlaid on the attenuation map.

Images were reconstructed using OSEM [6], with and without detector response function compensation (DRC) [7], and were then smoothed with a 3D Gaussian filter. For each tumor location and each combination of DRC versus nDRC and normalized versus un-normalized observer (defined below), localization was evaluated across a broad range of image updates (*i.e.* products of numbers of iterations and subsets) and of smoothing kernel widths, in order to determine an optimal number of updates and degree of smoothing at each location and for each method of reconstruction and each method of localization estimation. These different methods were compared using the iteration numbers and smoothing widths that were optimal for each method. In the comparison results presented below, four subsets were used to accelerate DRC reconstructions, but only one subset was used for nDRC images because the iteration-number optimization indicated that 1 iteration with 4 subsets gave too many image updates for optimal localization at several tumor sites. Post-reconstruction smoothing was performed using 3D Gaussian kernels that ranged in FWHM from 0 to 2.5 cm in increments of 0.5 cm. In total, 80 noisy images were reconstructed using 2 variations of OSEM (DRC and nDRC) and smoothed to different degrees with 6 Gaussian kernels at iterations 1-25.

Localization was assessed in a forced choice task, where each 3.0-cm-diameter spherical search volume Ω contained one and only one tumor. In the phantom, the tumor was centered in Ω at coordinates (x_t, y_t, z_t). A numerical observer sampled Ω every 0.3 cm in Cartesian space. The voxel with the greatest response and its 26 neighbors were then sampled more finely at every 0.1 cm. The observer selected subvoxel location $i(x_m, y_m, z_m)$ within Ω of noisy image g that produced the greatest scalar response from un-normalized cross correlation (XC) with an observer template w:

$$i(x_m, y_m, z_m) = \arg\max_{i\in\Omega} (\mathrm{XC}_i), \quad (1)$$

where

$$\mathrm{XC}_i = w \cdot g_i. \tag{2}$$

Thus, location (x_m, y_m, z_m) was recorded as the measured tumor position. The 3D template w was a sphere – the background-subtracted tumor signal as defined in the XCAT activity phantom. Template dimensions were 1.5 x 1.5 x 1.5 cm^3. The same template w was used for all 12 tumor sites and for both reconstruction methods and variations of cross correlation. Note that the spherical template was not matched exactly to a tumor because tumor appearance in the SPECT images was distorted due to the effects of distance-dependent spatial resolution, iteration number, and post-reconstruction smoothing.

Normalized cross correlation (NXC) was also investigated for estimating tumor positions:

$$\mathrm{NXC}_i = \frac{w \cdot g_i}{\sqrt{(w \cdot w)(g_i \cdot g_i)}}. \tag{3}$$

Localization error dr was calculated as the Euclidean distance between a true tumor position and a measured tumor position:

$$dr = \sqrt{(x_t - x_m)^2 + (y_t - y_m)^2 + (z_t - z_m)^2}. \tag{4}$$

Localization errors were recorded across the noisy image ensembles for each tumor site. Localization errors were compared for DRC-XC, DRC-NXC, nDRC-XC, and nDRC-NXC using site-specific optimal smoothing and iteration number parameters.

For each tumor site, direction-dependent localization errors were computed every 3° over 180°. These errors were indexed by an angle θ. Angle θ was defined in a transaxial plane as follows: θ was equal to 0 for the view from left lateral to center of rotation, $\pi/2$ for the anterior view, and π for the right lateral view. Direction-dependent localization bias ($b^{\perp\theta}$) and precision ($\sigma^{\perp\theta}$), indexed to a specific value of θ, were calculated along the dimension perpendicular to θ. As such, localization precision at the anterior view described the lateral spread of localization errors, and localization bias – the lateral bias. Fig 12 illustrates this convention using data from tumor G.

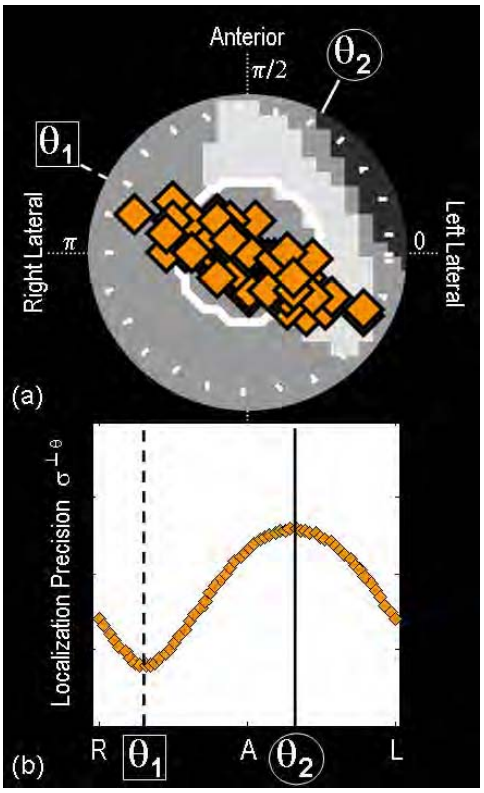

Fig. 12. (a) 80 tumor position estimates are marked by diamonds and overlaid on the attenuation map. The dashed and solid circles respectively mark the search volume and tumor boundaries. (b) direction-dependent localization precision is plotted as a function of angle θ.

The direction-dependent localization errors were defined mathematically as follows: Measured tumor coordinates $(x_{m,k}, y_{m,k})$ from noisy image k and true tumor coordinates (x_t, y_t) were rotated by angle θ using matrix T:

$$T = \begin{bmatrix} \cos\theta & -\sin\theta \\ \sin\theta & \cos\theta \end{bmatrix} \tag{5}$$

to yield

$$\begin{bmatrix} x^{\theta}_{m,k} \\ y^{\theta}_{m,k} \end{bmatrix} = T \begin{bmatrix} x_{m,k} \\ y_{m,k} \end{bmatrix} \tag{6}$$

and

$$\begin{bmatrix} x^{\theta}_{t} \\ y^{\theta}_{t} \end{bmatrix} = T \begin{bmatrix} x_{t} \\ y_{t} \end{bmatrix}. \tag{7}$$

For the direction perpendicular to θ, direction-dependent localization bias $b^{\perp\theta}$ was calculated as

$$b^{\perp\theta} = \frac{1}{N} \sum_{k=1}^{N=80} \left(y^{\theta}_{m,k} - y^{\theta}_{t} \right) \tag{8}$$

and direction-dependent localization precision $\sigma^{\perp\theta}$ as

$$\sigma^{\perp\theta} = \sqrt{\frac{1}{N-1} \sum_{k=1}^{N=80} \left(y^{\theta}_{m,k} - \overline{y^{\theta}_{m}} \right)^2}, \tag{9}$$

where

$$\overline{y^{\theta}_{m}} = \frac{1}{N} \sum_{k=1}^{N=80} y^{\theta}_{m,k}. \tag{10}$$

Localization performance was studied across a broad range of smoothing filters and iteration numbers. Results are reported below in Fig 13. Comparisons in localization performance between nDRC-XC, nDRC-NXC, DRC-XC, and DRC-NXC were made using the combination of smoothing and iteration number that resulted in the lowest mean localization error. Localization errors from the ensembles of 80 images are summarized by box plots in Fig 14.

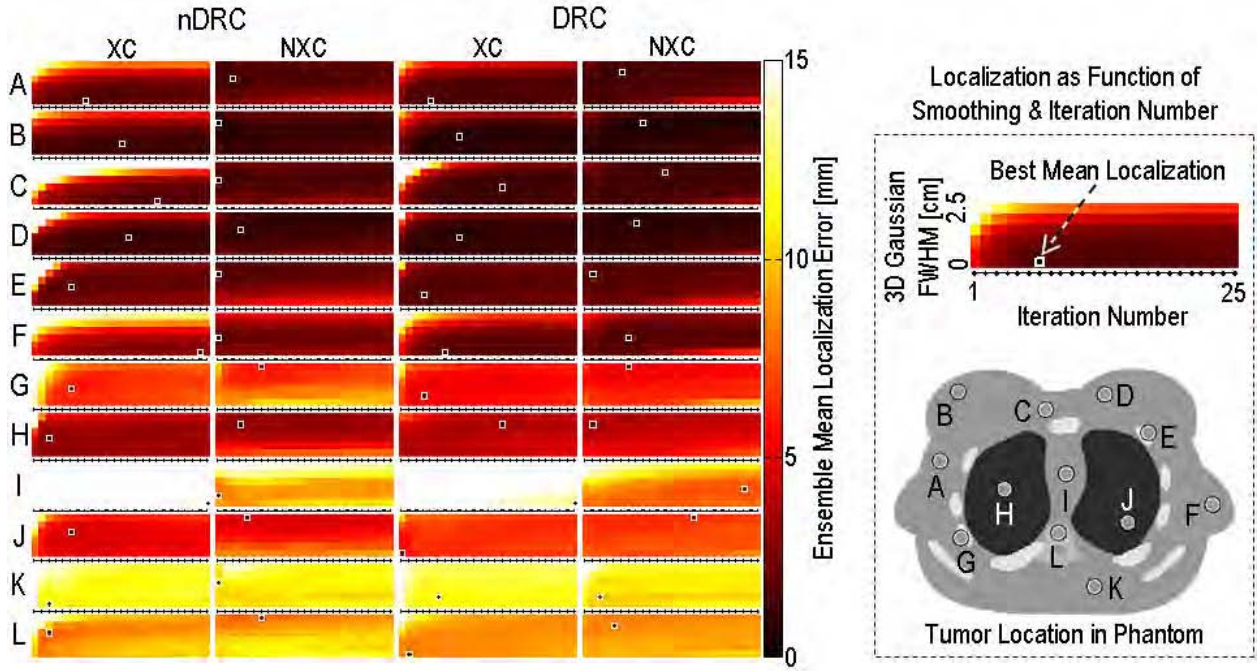

Fig. 13. Shows the effects of smoothing and iteration number on mean localization error for each tumor site (A-L) and also for the variations of image reconstruction (DRC vs. nDRC) and observer cross correlation (XC vs. NXC). The combination of smoothing and iteration number that yielded the lowest mean localization error is marked by a box.

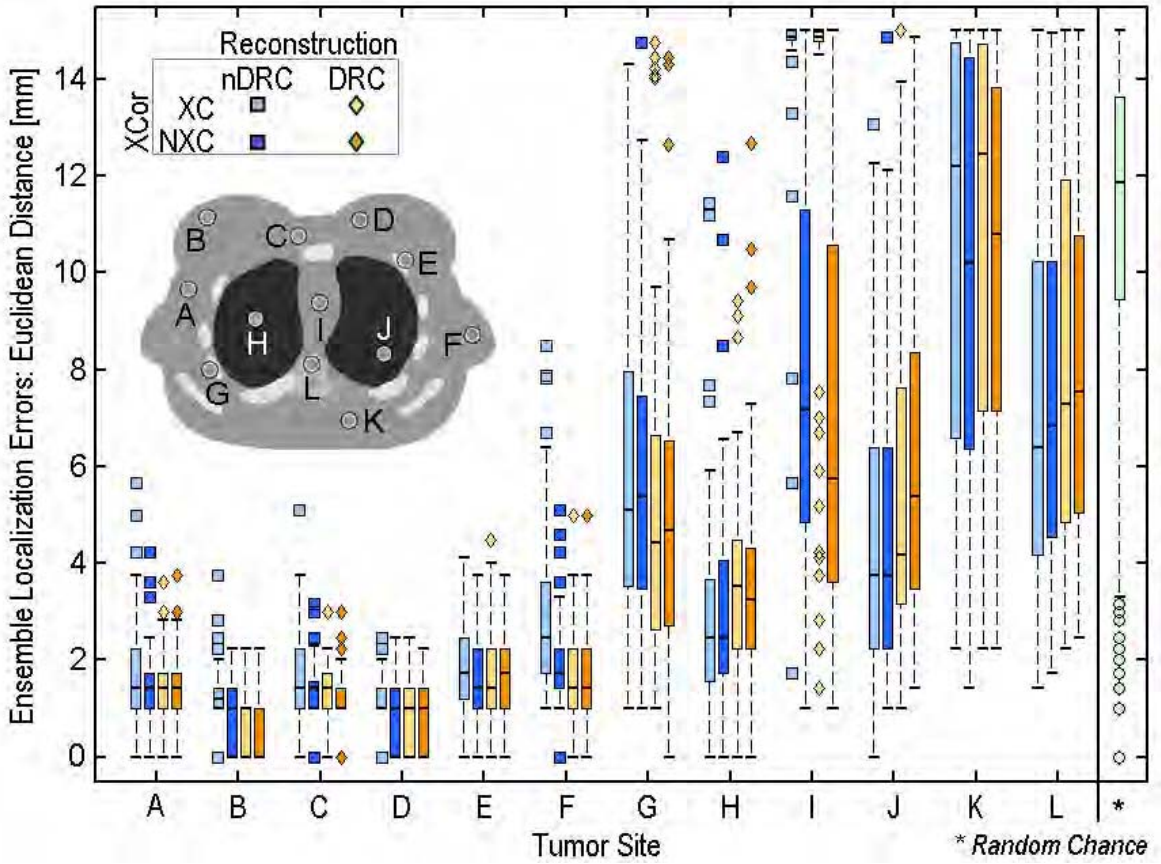

Fig. 14. Localization errors, calculated across ensembles of 80 images, are summarized by box plots. Median errors are marked by horizontal lines, the interquartile range (IQR) by filled rectangles, and outliers by squares or diamonds.

The random chance box plot describes the uniform probability of selecting any location in a search volume and thus provides a benchmark for gauging the amount of information provided by SPECT for target localization.
Tumor position estimates are displayed on the attenuation map in Fig 15. Note that the position estimates are tightly clustered at site B but are more diffuse and noticeably anisotropic at site G. The anisotropic error pattern at site G is related to the detector trajectory in Fig 16.

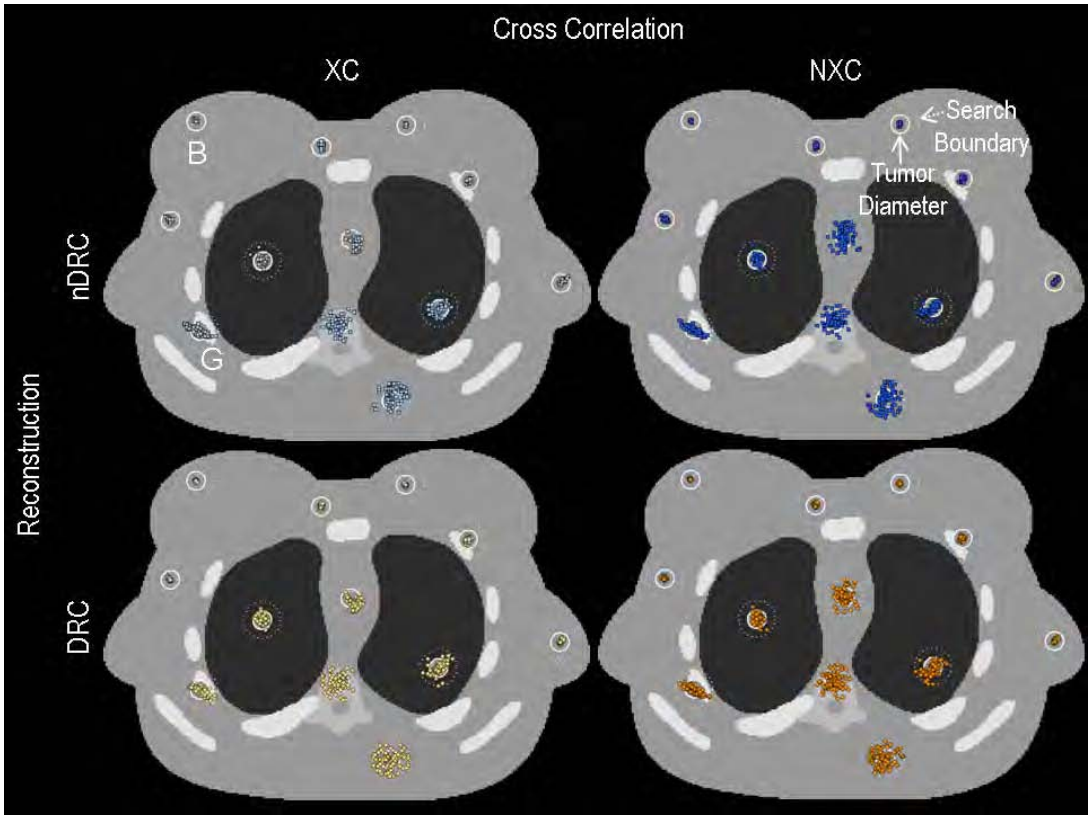

Fig. 15. Tumor position estimates from the 80-image ensembles are overlaid on the attenuation map.

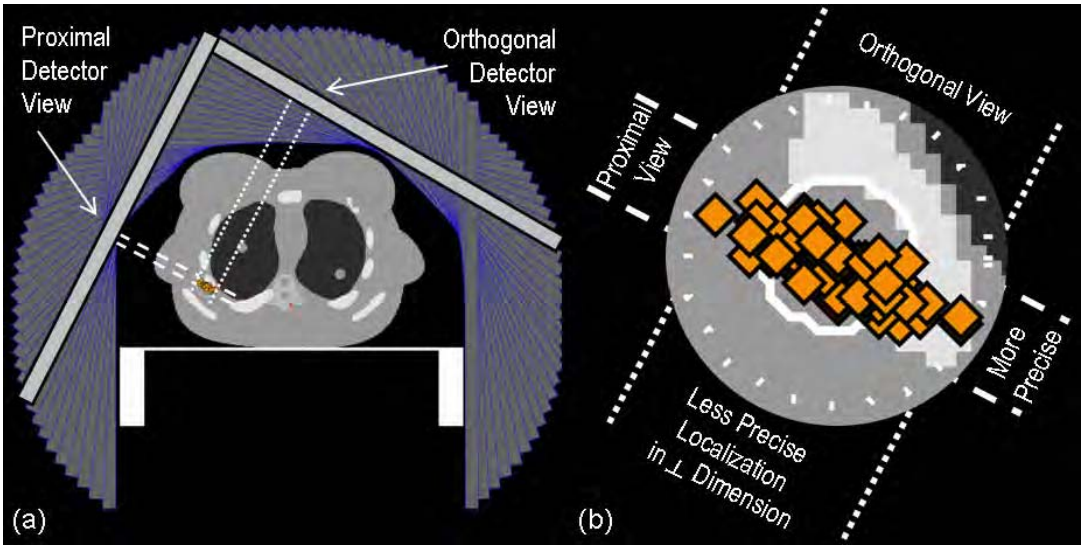

Fig. 16. (a) Shows the detector trajectory in reference to position estimates for tumor G. (b) Magnified view of the position estimates demonstrates that detector views of close approach and minimal attenuation are associated with more precise localization.

Direction-dependent localization bias and precision – calculated using Eqs (8,9) – are plotted in Fig 17 as a function of angle θ. Beneath these two curves are two additional sets of curves: The first set of curves shows collimator-tumor distance, which is proportional to collimator spatial resolution, and the second set shows attenuation survival probability (defined as the fraction of tumor photons directed towards the detector that are not attenuated by the

phantom). Detector angles of close approach and with high survival probabilities are predictive of directions with the best directional bias and precision, particularly for A-F.

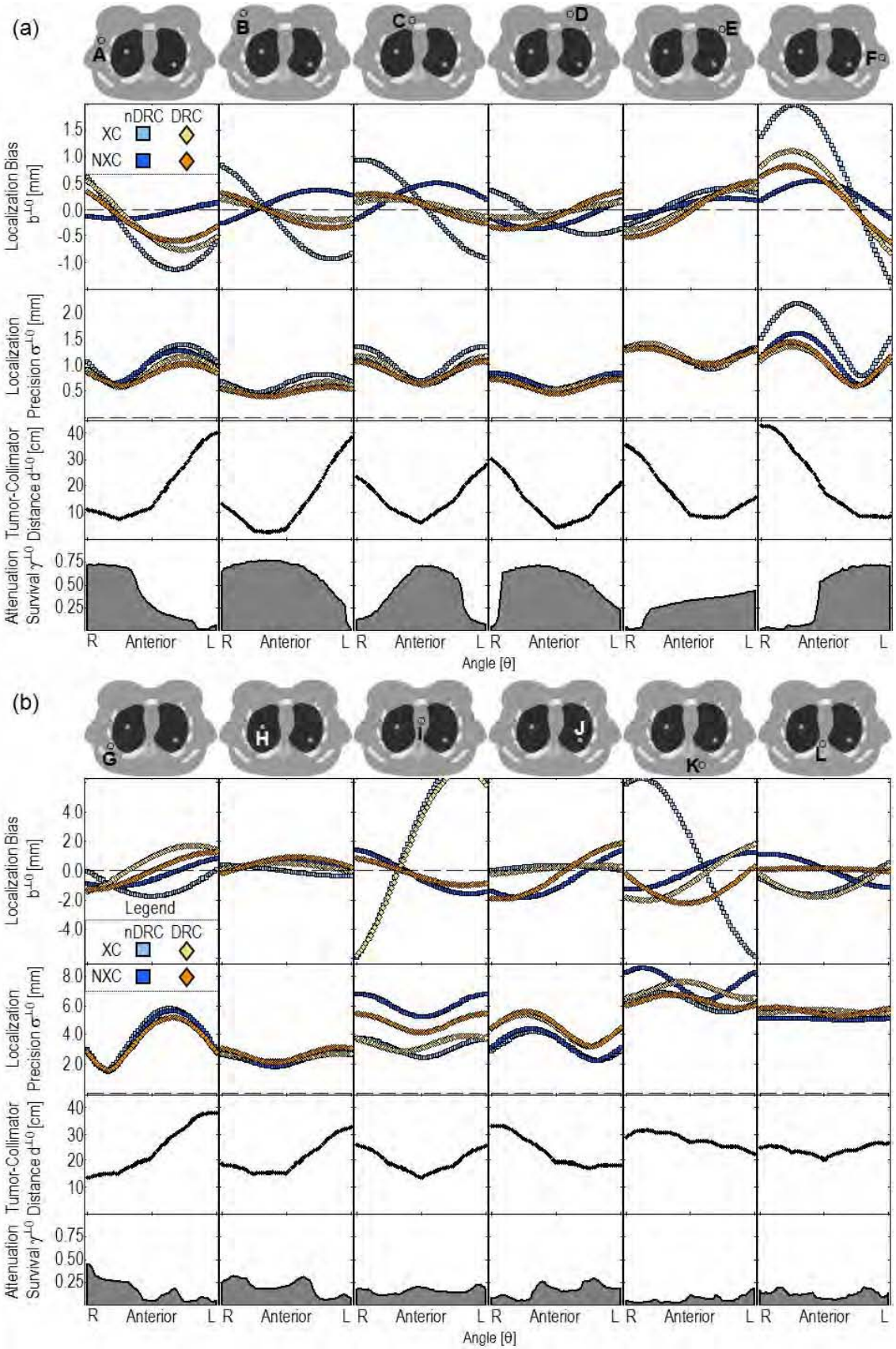

Fig. 17. (a) Direction-dependent localization bias and precision are plotted as a function of θ for tumors A-F. Horizontal dashed lines mark ideal bias and precision. Also plotted are curves showing tumor-collimator proximity and the survival

probability for photons from a tumor to escape the phantom without being attenuated. (b) Shows results for tumors G-L. Note that the direction-dependent localization bias curve is truncated at site I.

This computer-simulation study compared localization performance for normalized and un-normalized numerical observers, which were used to estimate tumor positions in SPECT images, reconstructed with and without DRC. For tumors localized to < 2 mm on average, which are good candidates for SPECT-guided radiation therapy, localization performance typically improved by compensating for the detector response function and by using a normalized observer.

For the two lung tumors, detector response function compensation did not improve localization performance. In certain images, localization errors were 1 cm or greater for the lung tumors. These results show that distance-dependent spatial resolution and attenuation can have a major effect on localization performance. Localization likely would be worse under free-breathing conditions. Respiratory gating would require more imaging time for the same counting statistics. These considerations and the results above demonstrate the challenges to imaging lung tumors with parallel-hole SPECT.

Localization errors were analyzed across the image ensemble and were found to be anisotropic and dependent on tumor position relative to the detector trajectory. Directional dependencies are attributable to the effects of attenuation and distance-dependent spatial resolution. Direction-dependent localization errors have important implications for external beam radiation therapy because radiation is often delivered from multiple gantry angles. These findings on direction-dependent localization errors might be useful to other SPECT-guided procedures, e.g., breast cancer biopsy.

The proposed studies to assess the localization of lung tumors as a function of different respiratory gating strategies are incomplete.

Specific Aim 3: Evaluate the impact of limited detector surface area, and consequent projection-data truncation, on the accuracy and precision of target localization.

Though this aim is largely incomplete, preliminary results in Appendix D, demonstrate that a sizeable region of interest surrounding a tumor can be reconstructed with similar results using either a full-size or compact detector given that the conditions of [8] are met. Localization was not assessed in this preliminary study.

Conclusions

On-board SPECT was investigated for localizing functional & molecular targets associated with metastatic breast cancer. Computer-simulation and hardware studies were performed to characterize localization accuracy and precision as a function of scan time, tumor size, tumor-to-background uptake ratio, and background non-uniformity. Localization performance was studied in images with and without spatial resolution modeling, using un-normalized and normalized observers, and for a broad range of iteration numbers and smoothing parameters. Of the parameters that can be controlled, the detector trajectory typically had the largest effect on localization performance. A proximal 180° trajectory yielded the best localization performance due to the effects of distance-dependent spatial resolution and attenuation. Also because of these effects, parallel-hole SPECT is better for the localization of superficial targets than deep targets. Another parameter that can be controlled is observer normalization. For tumors proximal to hotter background structures, the normalized observer placed more weight on template shape than on image intensities, as compared with the un-normalized observer, and in these cases, localization performance was vastly better using a normalized observer. Mean localization errors were < 2 mm for superficial tumors of > 1.4 cm in diameter and of 6:1 uptake ratio using a proximal detector trajectory and scan time of approximately 5 minutes. These results show the potential of SPECT for localizing certain targets given the time constraints of imaging inside radiation therapy treatment rooms.

References

1. Roper J, Bowsher J, Yin FF. On-board SPECT for localizing functional targets: a simulation study. *Medical Physics* 2009;36:1727-35.

2. Maublant J, deLatour M, Mestas D, Clemenson A, Charrier S, Feillel V, Le Bouedec G, Kaufmann P, Dauplat J, Veyre A. Technetium-99m-sestamibi uptake in breast tumor and associated lymph nodes. *Journal of Nuclear Medicine* 1996;37:922-925.

3. Farncombe TH, Gifford HC, Narayanan MV, Pretorius PH, Frey EC, King MA. Assessment of scatter compensation strategies for (67)Ga SPECT using numerical observers and human LROC studies. *Journal of Nuclear Medicine* 2004;45:802-12.

4. Horn BKP. Closed-Form Solution of Absolute Orientation Using Unit Quaternions. *Journal of the Optical Society of America a-Optics Image Science and Vision* 1987;4:629-642.

5. Segars WP, Tsui BM. Study of the efficacy of respiratory gating in myocardial SPECT using the new 4D NCAT Phantom. *IEEE Transactions on Nuclear Science* 2002;49:675-679.

6. Hudson HM, Larkin RS. Accelerated Image-Reconstruction Using Ordered Subsets of Projection Data. *IEEE Transactions on Medical Imaging* 1994;13:601-609.

7. Frey EC, Tsui, B.M.W. Collimator-Detector Response Compensation in SPECT In: Zaidi H, ed. Quantitative Analysis in Nuclear Medicine Imaging: Springer, 2006:141-166.

8. Defrise M, Noo F, Clackdoyle R, Kudo H. Truncated Hilbert transform and image reconstruction from limited tomographic data. *Inverse Problems* 2006;22:1037-1053.

Key Research Accomplishments

Aim 1 was addressed through computer simulation and hardware studies. In the computer-simulation study, localization accuracy and precision were evaluated as a function of scan time, tumor size, tumor-to-background uptake ratio, and background non-uniformity. This work was published in a peer-reviewed journal *Medical Physics* (please see Appendix B.) A hardware study was performed to study the effects of the detector trajectory on localization performance. This study shows the degree of localization accuracy and precision that can be achieved using a commercially available SPECT detector. Findings from this study have been submitted to *Medical Physics*.

Aim 2 involves the localization of tumors in the lungs. Localization was studied for these and other tumors as a function of spatial resolution modeling, observer normalization, number of iterations, and the degree of post-reconstruction smoothing. This study has been accepted for publication in *Medical Physics* (please see Appendix C.)

My research has been presented at conferences hosted by AAPM and ASTRO. Published abstracts are listed below in Appendices D-G.

Other Tasks Related to BCRP Predoctoral Traineeship:
(Appendix A)

• I have gained a better understanding of clinical care for breast cancer patients through interactions with physicians from radiology and radiation oncology at Duke University. More specifically, I have attended the Joint Breast Conference where patient charts are reviewed by surgeons, oncologists, radiation oncologists, pathologists, nurses, and others involved in patient care to determine the best course of treatment. Further, I have completed the Nuclear Medicine Practicum offered by the Medical Physics Graduate Program where I spent time in a reading room with radiologists who explained the strategies and challenges of interpreting nuclear medicine images.

• I have participated in and presented my research at journal clubs and seminars hosted by the Medical Physics Graduate Program and by the Department of Radiation Oncology. For two semesters, I was responsible for organizing weekly research meetings in the Physics Division of Radiation Oncology where ongoing research was presented by graduate students and postdoctoral researchers.

• I have completed the course work required by the Medical Physics Graduate Program and fulfilled all teaching assistantships. During the spring semester 2009, I participated in an independent study involving IMRT treatment planning under the supervision of a senior medical physicist. Through this course, I gained practical skills for creating treatment plans that deliver prescribed dose to tumor while sparing healthy tissues.

• Results from this report were included in my preliminary exam proposal and presentation, “On-board SPECT Imaging for Localizing Biological Targets”, which was accepted by my committee on April, 20 2009.

• I successfully defended my dissertation “On-board Single Photon Emission Computed Tomography (SPECT) for Biological Target Localization” on June, 21 2010.

Bibliography

Peer-reviewed articles

JR Roper, JE Bowsher, FF Yin. "On-board SPECT for localizing functional targets: A simulation study." *Med. Phys*. Volume 36, Issue 5, pp. 1727-1735 (May 2009)

JR Roper, JE Bowsher, FF Yin. "Direction-dependent localization errors in SPECT images." *(accepted for publication in Med. Phys.)*

JR Roper, JE Bowsher, JM Wilson, TG Turkington, FF Yin. "On-board SPECT: Target localization and the effect of the detector trajectory in scanner-acquired images." *(submitted to Med. Phys.)*

Presentations and published abstracts

JR Roper, JE Bowsher, FF Yin. "Quantitative Analysis of On-board SPECT Imaging Using Compact Gamma Cameras." Poster presentation at the *50th Annual AAPM Meeting*, Houston, TX, 27 – 31 Jul. 2008.

JR Roper, AA Manzoor, JB Bowsher, FF Yin, S-M Zhou, TZ Wong, S Borges-Neto, JL Hubbs, S Demirci, LB Marks. "Are post-RT cardiac perfusion defects due to cardiac toxicity, or are they artifacts from attenuation changes in surrounding soft tissues?" Poster presentation at the *50th Annual ASTRO Meeting*, Boston, MA, 21 – 25 Sept. 2008.

JR Roper, JE Bowsher, FF Yin. "On-board SPECT Imaging: Improved Target Localization via Spatial Resolution Compensation." Poster presentation at the *51th Annual ASTRO Meeting*, Chicago, IL, 1 – 5 Nov. 2009.

JR Roper, JM Wilson, JE Bowsher, TG Turkington, FF Yin. "On-Board SPECT: Localization Study Using Scanner-Acquired Data." Moderated poster presentation at the *52th Annual AAPM Meeting*, Philadelphia, PA, 18 – 22 Jul. 2010.

Invited talks

"Overview of medical physics and my PhD research experience." Tennessee Governor's School for Computational Physics, Clarksville, TN, 3 June 2010.

"Overview of medical physics and my PhD research experience." ACS – DOE Summer School in Nuclear and Radiochemistry, Brookhaven National Laboratory, Upton, NY, 13 June 2010.

Appendix A

Specific Aim 1: Evaluate localization accuracy and precision as a function of scan time, tumor size, tumor-to-background uptake ratio, and background non-uniformity.

A. Hardware Phantom Studies (Months 1- 8)
- a. Fillable hot spheres in a lower-activity cylindrical background, approximately mimicking the geometry of supraclavicular lymph nodes
- b. Sphere diameters ranging from 8mm to 24mm
- c. Lesion-to-background uptake ratios of 2:1, 5:1, and 10:1
- d. Background non-uniformity: 40mm sphere with an offset inner 8mm sphere
- e. Activity ratios of 10:2:1 and 10:5:1 in the outer sphere, inner sphere, and background
- f. Acquire projection images using a Trionix Triad XLT SPECT scanner.
- g. Scan times from 1 minute to 24 minutes
- h. Acquire CT image of the same phantom (See 1B below).
- i. From ensemble of images, evaluate the following as a function of scan time, tumor size, tumor-to-background uptake ratio, and background non-uniformity:
  - i. Evaluate contrast-to-noise ratios (CNRs)
  - ii. Evaluate MAFC
- j. Prepare and submit paper on this work. (Months 7- 8)

B. Use Above Hardware Data to Validate Computer-Simulation Studies (Months 9-12)
- a. Generate software phantom by digitizing the CT image of the 1A hardware phantom.
- b. Repeat 1A studies using the digital, software phantom.
- c. Compare hardware and software studies, in order to validate the software approach (which is employed below in 2A-3A).

Specific Aim 2: Evaluate the effect of respiratory motion on the accuracy and precision of target localization.

A. Software Studies using Digital Anthropomorphic Phantom (Months 13-19)
- a. Hot spherical lesions surrounded by warm background activity in torso of NCAT anthropomorphic phantom, simulating breast cancer metastasis in bone, lung, and lymph nodes.
- b. Lesion sizes ranging from 8mm to 24mm
- c. Radiotracer uptake ratios of 2:1, 5:1, and 10:1 in lesions and background
- d. Scan times ranging from 1 minute up to 24 minutes
- e. Generate ensembles of breath-hold images
- f. Evaluate CNR and MAFC as function of lesion size, lesion-to-background uptake ratio, and scan time.

B. Digital Anthropomorphic Phantom with Respiratory Motion (Months 20- 28)
- a. Enable respiratory motion features within NCAT software.
  - i. Model ungated onboard SPECT imaging during free breathing
  - ii. Model gated onboard SPECT imaging during free breathing
- b. Repeat 2A studies with the addition of respiratory motion
- c. Calculate CNR and MAFC as a function of lesion size, lesion-to-background uptake ratio, scan time, and scan mode (as described in 2Bai-ii)
- d. Prepare and submit paper for work in 2A-B. (Months 27- 28)

Specific Aim 3: Evaluate the impact of limited detector surface area, and consequent projection-data truncation, on the accuracy and precision of target localization.

A. Software Studies using Truncated Detector Field of View (FOV) (Months 29-36)
- a. Truncate projection images from 2A to simulate detectors with smaller surface areas.
- b. Detector FOV ranging from 15x15cm2 to 20x40cm2
- c. Investigate the dependence of CNR and MAFC on detector FOV.
- d. Evaluate the relationship between detector FOV and truncation artifacts.
- e. Write and submit paper (Months 35-36)

Other Tasks Related to BCRP Predoctoral Traineeship.

A. Shadow radiologist(s) to better understand breast cancer diagnoses and staging. (Months 1-12)
B. Shadow radiation oncologist(s) to learn about breast cancer therapies. (Months 1-12)
C. Participate in weekly journal clubs and seminars. (Months 1-36)
D. Audit courses relevant to my breast cancer research project (Months 1-36)
E. Present research at conferences such as AAPM, ASTRO, and the Era of Hope Meeting. (Months 1-36)
F. Gain experience with RT medical physics (e.g. treatment planning & quality assurance). (Months 12-36)
G. Prepare and defend PhD dissertation (Months 30-36)

Appendix B

JR Roper, JE Bowsher, FF Yin. “On-board SPECT for localizing functional targets: A simulation study.” *Med. Phys*. Volume 36, Issue 5, pp. 1727-1735 (May 2009)

On-board SPECT for localizing functional targets: A simulation study

Justin Roper,[a] James Bowsher, and Fang-Fang Yin
Department of Radiation Oncology, Medical Physics Graduate Program, Duke University Medical Center, Durham, North Carolina 27710

(Received 29 September 2008; revised 23 February 2009; accepted for publication 16 March 2009; published 16 April 2009)

Single photon emission computed tomography (SPECT) was investigated for imaging on-board radiation therapy machines in order to localize functional and molecular targets. A computer-simulated female NCAT phantom was positioned supine on a flat-top treatment couch. Twenty tumor locations were defined in the upper torso. The eight lung tumors were subject to the effects of respiratory motion. Tumor diameters of 10.8, 14.4, and 21.6 mm were simulated for tumor-to-background ratios of 3:1 and 6:1 that are characteristic of the radiotracer ^{99m}Tc-sestamibi. Projection images representing scan times of 4, 8, and 20 min were simulated for an anterior, half-circular trajectory. Images were reconstructed with attenuation correction by ordered-subsets expectation maximization (OSEM) using six subsets and five iterations. Contrast-to-noise ratios (CNRs) were calculated from ensembles of 25 images. Cross correlation with a noise-free tumor template was used to select the most suspicious tumor location within a 14.4-mm-radius search volume surrounding each tumor, with only that one tumor in each search volume. Localization accuracy was assessed by calculating average distances between measured and true tumor locations. Localization accuracy and CNRs were strongly affected by tumor location relative to the detector trajectory. For example, CNR values near the chest wall were greater by a factor of 3.5 than for tumors near the spine and posterior ribs, a much greater effect than the factor of 1.6 difference in CNR between 6:1 and 3:1 tumor uptakes. Typically, tumors of 6:1 uptake were localized as accurately with 4 min of scan time as tumors of 3:1 uptake that had been imaged for 20 min. Using 4 min scans, 14.4 and 21.6 mm anterior tumors of 6:1 uptake were localized within 2 mm. These results suggest that SPECT, on-board radiation therapy machines, may be a viable modality for localizing certain functional and molecular targets using relatively short scan times. [DOI: 10.1118/1.3113902]

Key words: SPECT, on-board imaging, target localization

I. INTRODUCTION

Functional imaging modalities such as positron emission tomography (PET) and single photon emission computed tomography (SPECT) rely on radiotracers to identify physiological processes—such as angiogenesis, apoptosis, hormone receptor status, hypoxia, and proliferation—that have important implications in cancer management.[1] In the context of radiation therapy, such functional information can be used to define biological target volumes and, when combined with the dose sculpting capabilities of intensity modulated radiation therapy (IMRT), may provide enhanced therapeutic success.[2] To date, SPECT and PET have been utilized for diagnosis, staging, and treatment planning. We propose that functional imaging may also have an important role in the treatment room for the delivery of radiation therapy. Currently, treatment-room imaging is composed mainly of x-ray transmission imaging and ultrasound imaging, which are predominantly anatomical imaging modalities.[3] Imaging with these modalities immediately prior to delivery has improved patient alignment and reduced normal tissue damage for some sites,[3] but there are limitations. Notably, anatomical differences between tumor and surrounding tissue may not be substantial enough to directly visualize tumor. Consequently, localization is often performed instead with indirect markers such as bony anatomy, that may not necessarily indicate tumor position.[4–6] This limitation may be particularly important when high gradients are used to sculpt dose around biological targets that cannot be visualized using current treatment-room imaging modalities. Further, ultimately radiation therapy may be directed to temporally varying functional targets, such as hypoxia, which at treatment time may be in a location different from their location during planning CT or planning functional imaging.[7]

One possible method for directly localizing biological targets is to image with SPECT inside radiation therapy treatment rooms. SPECT has been used for a wide array of tumor imaging applications,[8,9] and ongoing research is expanding the already broad array of radiotracers.[10–15] While spatial resolution is somewhat limited compared with many anatomical imaging modalities, contrast between tumor and background can be substantially greater, and this stronger tumor signal may improve treatment-room tumor localization.

Though SPECT has been studied extensively for diagnostic tasks, SPECT has not been developed for the treatment-room environment where new challenges await. Notably, SPECT scans typically last 20 min or more, and this amount of time is too long in terms of patient motion and machine throughput. Shorter imaging times are needed, which implies

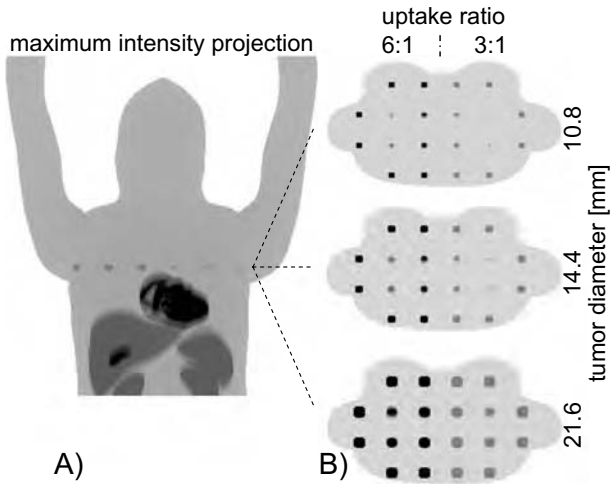

FIG. 1. (A) Coronal view of radiotracer distribution in phantom; (B) uptake pattern for different tumor sizes in transaxial slice.

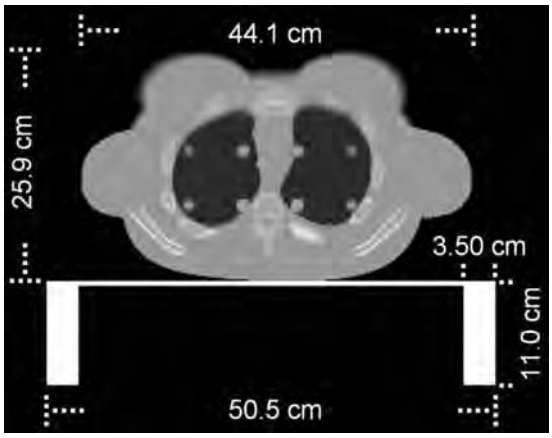

FIG. 2. Attenuation map of phantom and treatment couch with dimensions.

greater image noise. Additionally, treatment-room couches are wider and supporting rails are typically deeper than diagnostic SPECT couches. As such, treatment couches may challenge detector-to-patient proximity and increase attenuation, which in turn degrade image quality with poorer spatial resolution and increased noise. While these constraints will negatively impact image quality, it is important to consider that the task for on-board SPECT would be different than with most diagnostic SPECT scans. Because target size and approximate location are known, it may be possible to accurately localize functional targets. Furthermore, SPECT detector trajectories can be optimized for imaging the treatment region, a factor which may enhance SPECT images in the region of interest (ROI) as compared to diagnostic scans which typically have to survey a larger volume.

II. METHODS AND MATERIALS

II.A. Phantom

A female anthropomorphic phantom was generated with NCAT software.[16,17] The phantom was placed supine on a flat-surface treatment couch. Twenty tumor locations were arranged periodically on a square grid with centroid-to-centroid spacing of approximately 6 cm. Tumors were centered on voxels in an axial slice superior to the heart. For each tumor location, three tumor diameters—10.8, 14.4, and 21.6 mm with true volumes of 0.980, 2.10, and 6.49 cm^3—were simulated in separate phantoms as shown in Fig. 1. The 8 deepest tumors were located in the lungs where they were subject to respiratory motion, while the remaining 12 tumors were stationary in soft tissues or bone. Activity distribution was modeled for the radiotracer ^{99m}Tc-sestamibi that has been used to image a number of tumors, including breast cancer and its metastases.[18–20] Activity concentrations were 5.0 μCi/ml in the gall bladder and myocardium, 2.5 μCi/ml in the liver, kidneys, and spleen, and 0.25 μCi/ml in other healthy tissues. Left- and right-sided tumor activity concentrations were 1.75 and 1.5 μCi/ml, respectively, as these uptake values relative to normal tissues—3:1 and 6:1—have been noted clinically.[19]

We used NCAT software to generate a CT-like image of linear attenuation coefficients for 140 keV photons in the following tissues: 0.149–0.157 cm^{-1} in soft tissues and 0.163–0.220 cm^{-1} in bone. The attenuation phantom had the exact geometry of the activity phantom. The couch was assigned a linear coefficient of 0.250 cm^{-1}, which corresponds to a predominately carbon-based material with physical density of 1.8 g/cm^3.[21] A map of attenuation coefficients and dimensions for a slice containing tumor are shown in Fig. 2.

The effects of respiration were considered by averaging 16 phases of a respiratory cycle where the diaphragm moved 20.0 mm and the chest expanded by 12.0 mm. Normal structures experienced varying degrees of 2D motion in the anteroposterior (AP) and superoinferior (SI) dimensions. Identical motion vectors were applied to laterally symmetric left- and right-sided lung tumors to minimize differences other than activity concentration. Lung tumor motion was characterized by one of four maximum centroid-to-centroid displacements according to tumor location: anteromedial (7.20 mm SI, 7.20 mm AP), anterolateral (10.8 mm SI, 10.8 mm AP), posteromedial (7.20 mm SI, 3.60 mm AP), posterolateral (10.8 mm SI, 3.60 mm AP). Tumors outside the lungs were stationary. Activity and attenuation phantoms were implemented on a $384\times384\times384$ grid of 0.18-cm-wide voxels. Attenuation phantoms, one for each tumor size, were also placed on a coarser grid with 0.36-cm-wide voxels and were used to correct for nonuniform attenuation during reconstruction.

II.B. Projection data simulation and image reconstruction

SPECT imaging was simulated with an analytical, ray-driven software using the code SPECT-MAP which has been utilized and tested in this and many previous studies, e.g., Refs. 22–26. Projection images were modeled for a gamma camera with 46×23 cm^2 active surface area and parallel-hole, low-energy, high-resolution collimation. Simulated collimator holes were 2.7 cm long by 0.14 cm in diameter.

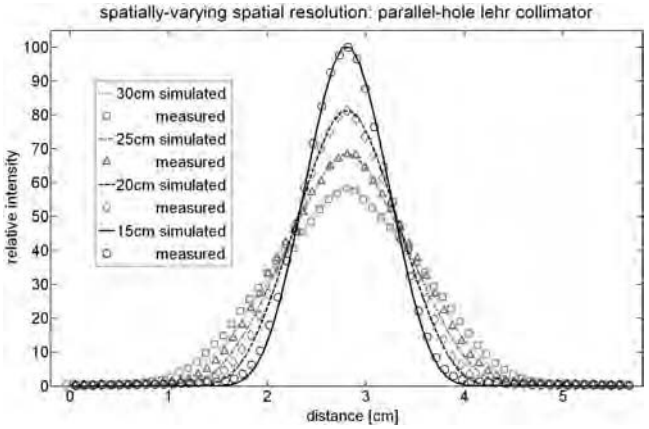

FIG. 3. Line source profiles for measured and simulated data that show the effects of distance-dependent collimator resolution. Measurements were made with a Trionix Triad SPECT scanner.

Distance-dependent spatial resolution was determined by fitting an analytical form to measured projection data. This spatial resolution modeling was implemented by tracing a cone of 121 rays from multiple subdivisions of each detector bin. The resolution modeling was validated by comparing measured line spread functions to those calculated using 121-ray cones, as shown in Fig. 3. Intrinsic resolution was modeled with a 2D, 0.34-cm-FWHM Gaussian kernel. Also modeled were the efficiencies of the collimator, scintillator, and branching ratio of ^{99m}Tc. SPECT-MAP calculations of efficiency and attenuation were checked against hand calculations. Scatter was not considered.

Projection images were simulated for step-and-shoot mode every 3° over a half-circular trajectory by rotating the detector from right lateral over the chest to left lateral as shown in Fig. 4. Bins in projection images were 0.36 cm wide. Finite bin width was modeled by tracing four cones from each bin, i.e., one cone from the center of the four quadrants; thus in total $4\times121=484$ rays were traced from each detector bin. The detector-to-image-plane radius of rotation was 26.5 cm with the axis of rotation centered near the phantom spine. Using this detector and trajectory, there was no truncation of the transaxial slices containing tumors, as demonstrated in Fig. 4 by the dashed line that encloses the common volume, i.e., the region that is projected onto the detector surface at every angle. These simulated noise-free 2D projection images were degraded with varying levels of Poisson noise corresponding to scan times of 4, 8, and 20 min. Ensembles of 25 independent noisy projection images were generated for each combination of scan time and tumor size.

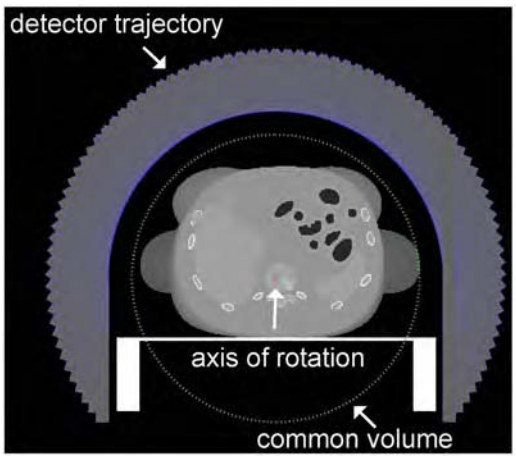

FIG. 4. Detector trajectory spanning 180° anteriorly is displayed with overlapping gray bars. Axis of rotation is marked with an asterisk. Common volume—voxels projected onto the detector at every view—is inside the dashed line.

Image ensembles were reconstructed via ordered-subsets expectation maximization (OSEM) (Ref. 27) using six subsets and five iterations, which are in the range of typically used values.[28] Attenuation correction was achieved by modeling photon detection probabilities within OSEM. In the reconstructed images, the intensities of deep background regions were similar to those in the phantom, thus validating attenuation correction. Our reconstructions did not model distance-dependent spatial resolution, as is typical of most clinical SPECT imaging. Image voxels were 0.36 cm wide, a factor of 2 coarser than voxels of grids on which phantoms were placed for simulating projections. During reconstruction, four rays were traced from every projection bin through the reconstruction grid in order to average over the finite detector bin width. Rays were oriented perpendicular to the image plane and spaced equally from one another in the transaxial dimension of a bin. Additional rays were not traced along the axial (superior-inferior) dimension because of the exact axial alignment between projection bins and image voxels at every detector view. Noisy reconstructed images were smoothed with 3D Gaussian kernels of 8, 14, and 20 mm FWHMs.

II.C. Image analysis

Contrast-to-noise ratios (CNRs) and localization metrics were calculated from noisy image ensembles. For CNR calculations, 3D ROIs were drawn around the tumor. Approximately 7.2 mm away from these ROI boundaries, shell-like ROIs were defined in the background. ROIs were approximately spherical for stationary tumors. For lung tumors, ROIs were irregularly shaped so as to account for the asymmetric blurring effects of respiratory motion. Both tumor and background ROIs were the size of tumor volumes and encompassed 21, 45, and 139 voxels for respective tumor diameters of 10.8, 14.4, and 21.6 mm.

Contrast was defined as

$$C_i = \frac{\overline{T_i} - \overline{B_i}}{\overline{B_i}}, \tag{1}$$

where $\overline{T_i}$ and $\overline{B_i}$ are mean tumor and background ROI intensities in image i. Mean contrast,

$$\hat{C} = \frac{\sum_{i=1}^{N} C_i}{N}, \tag{2}$$

was calculated from the $N=25$ noisy reconstructed images. This definition of contrast allows for negative values when the background is hotter than the tumor in order to avoid upward bias of mean contrast values when background noise dominates the tumor signal. Noise was calculated as the standard deviation of contrast:

$$\sigma_{\hat{C}} = \sqrt{\frac{\sum_{i=1}^{N}(C_i - \hat{C})^2}{N-1}}. \tag{3}$$

Ensemble average contrast-to-noise ratio was

$$\mathrm{CNR} = \frac{\hat{C}}{\sigma_{\hat{C}}}. \tag{4}$$

Localization accuracy and precision were assessed by calculating the mean and standard deviation of distances between true and measured tumor centroids over ensembles of noisy reconstructed images. Tumor locations in noisy images were selected via a forced choice task using nonprewhitening filters.[29–31] This approach is relevant to radiation therapy delivery because disease is known to exist; yet the exact position varies with each time the patient is positioned on the treatment table.

Since the approximate tumor location is known from treatment-planning images, the search can be limited to a relatively small volume. In this study, 3D search volumes—14.4-mm-radius spherical ROIs—were defined around each tumor. The size of each search volume was intended to encompass the uncertainties in tumor location that are typical for radiation therapy. Each search volume contained 257 voxels that were subdivided three times in each dimension. The location in the ROI that had the highest cross correlation (XC) with a noise-free tumor template was selected as the measured tumor centroid:

$$\mathrm{XC}_i = \frac{\mathrm{template}_j \cdot \mathrm{image}_i}{\sqrt{(\mathrm{template}_j \cdot \mathrm{template}_j)(\mathrm{image}_i \cdot \mathrm{image}_i)}}, \tag{5}$$

$$r_{m,i} = \arg\max_{j \in \Omega}(\mathrm{XC}_{i,j}), \tag{6}$$

where $\mathrm{template}_j$ represents the template centered at voxel j within ROI Ω of ensemble image i. The denominator in the above cross-correlation equation normalizes the response such that it does not depend on voxel intensities. As such cross-correlation values were suppressed for hot background structures (e.g., heart) that would have otherwise elicited greater responses than the nearby tumor. Tumor templates were generated by convolving true tumor geometries with a 14.4-mm-Gaussian kernel that approximates typical spatial resolutions in these images. For lung tumors, the true tumor geometry included asymmetric blurring from respiratory motion. Tumor templates were constructed on cubic grids of 0.12-cm-wide voxels with grid widths of 27, 33, and 39 voxels for tumor diameters of 10.8, 14.4, and 21.6 mm, respectively.

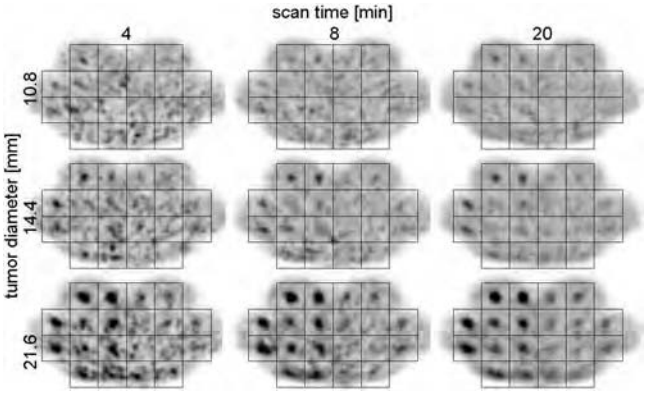

FIG. 5. Sample reconstructed images, smoothed with 14-mm-FWHM Gaussian, for each combination of tumor size and scan time.

Mean localization error $\overline{dr}$ was defined as the offset distance dr between true $r_t=(x_t,y_t,z_t)$ and measured tumor centroids $r_{m,i}=(x_{m,i},y_{m,i},z_{m,i})$ averaged over the ensemble of $N=25$ noisy reconstructed images:

$$dr = \sqrt{(x_m - x_t)^2 + (y_m - y_t)^2 + (z_m - z_t)^2}, \tag{7}$$

$$\overline{dr} = \frac{1}{N}\sum_{i=1}^{N} dr_i. \tag{8}$$

Standard deviation in localization error was computed as

$$\sigma_{dr} = \sqrt{\frac{\sum_{i=1}^{N}(dr_i - \overline{dr})^2}{N-1}}. \tag{9}$$

III. RESULTS

III.A. Reconstructed images

Reconstructed images for each combination of tumor diameter and scan time are presented in Fig. 5. These images are noisy realizations, not ensemble averages, and have been smoothed with a 3D, 14-mm-FWHM Gaussian kernel. Grids are superimposed on images such that each square element is centered on a tumor.

Qualitative trends are apparent in these images. As scan time increases, noise decreases, thereby improving the tumor visibility. For instance, with the 4 min scans, image noise resembles the expected signal for 10.8 and 14.4 mm diameter tumors in some locations, especially in the lungs and near posterior of the phantom. When scan time is increased to 8 and then 20 min, there are fewer and fewer hot spots off center of the grid, which suggests that the apparent activity is the true tumor signal. Tumor-to-background uptake ratios have a substantial effect on tumor visibility, as those on the patient right side with 6:1 uptake ratios are more noticeable than left-sided tumors with 3:1 uptake ratios. Also note the impact of tumor location relative to the detector trajectory: Tumors near the chest wall, which are on average closer to the detector, are strikingly more apparent than lung tumors and stationary tumors near the spine. The detector trajectory also affects apparent tumor shape. Anterior tumors are ap-

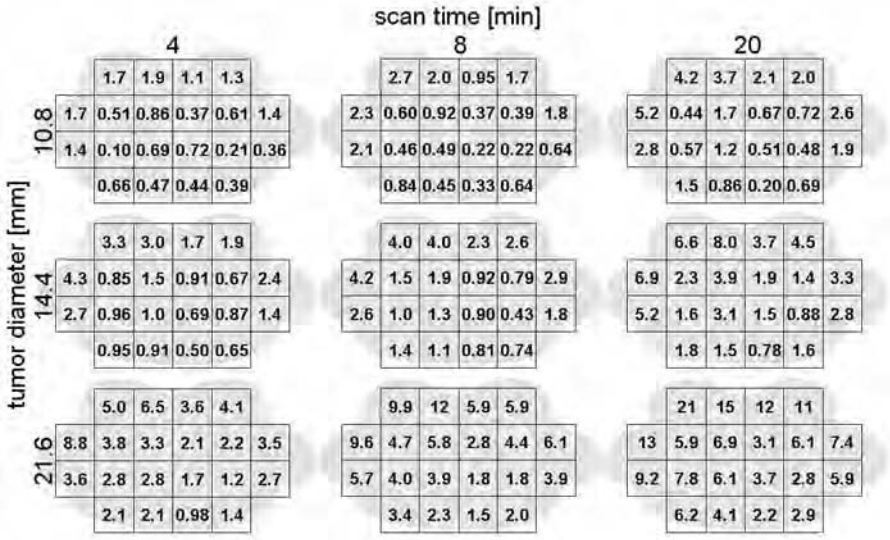

FIG. 6. CNRs calculated from ensembles of noisy reconstructed images and presented as a function of location for each combination of scan time and tumor diameter.

proximately circular, while other visible tumors are elliptical with varying degrees of eccentricity. Greater eccentricity occurs when the detector-to-tumor distance is substantially different over the detector trajectory.

III.B. Contrast-to-noise ratio

CNRs were calculated from ensembles of noisy reconstructed images using Eqs. (1)–(4). CNR values are displayed in Fig. 6 as a function of anatomy for the investigated scan times and tumor diameters. Many of the visual trends noted in the reconstructed images from Fig. 5 are expressed quantitatively in Fig. 6 as ensemble CNRs. CNRs increase approximately by the square root of imaging time. Right-sided tumors with 6:1 radiotracer uptake ratios have higher CNRs than their laterally symmetric counterparts of 3:1 uptake by an average factor of 1.6. CNRs of anterior tumors are typically 3.5 times greater than their posterior counterparts. These trends are shown in Fig. 7, thus demonstrating the relative impact of radiotracer uptake versus the detector trajectory on CNR.

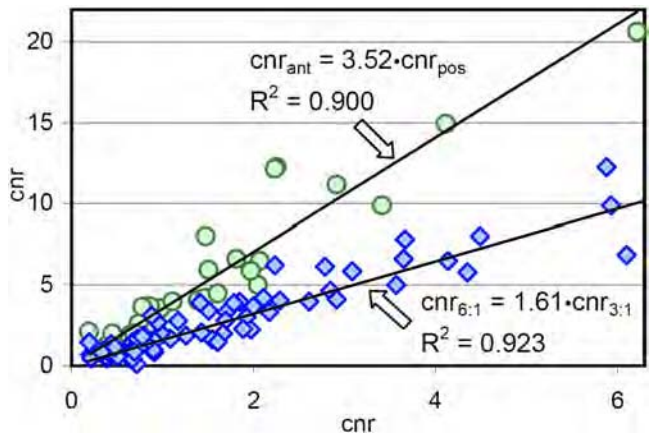

FIG. 7. Differences in CNR due to radiotracer uptake and anatomical location. Circles represent differences in CNR between anterior tumors and their posterior counterparts. Diamonds indicate the CNRs of laterally symmetric tumors that differ by radiotracer uptake.

III.C. Localization

Localization metrics—the mean localization error $\overline{dr}$ and ensemble standard deviation σ_{dr}—were calculated using Eqs. (5)–(9) and are reported in Fig. 8. Mean errors are represented by white and black boxes that respectively correspond to tumors of 6:1 and 3:1 radiotracer uptakes. Error bars indicate standard deviations. The different tumor sizes are separated by rows. Columns differentiate tumor locations. Note the diagram above each column in Fig. 8 that specifies anatomical locations. Within each column there are six data points—three white and three black boxes—that correspond to scan times of 4, 8, and 20 min for each uptake ratio. When viewing Fig. 8 from left to right, tumor locations vary from anterior to lateral to posterior. A bold dashed line separates stationary and lung tumors. The relative order of lung tumors is the same as that of stationary tumors.

In all but the regions of poorest SPECT image quality, tumors of 6:1 uptake are typically localized as accurately with 4 min of scan time as tumors of 3:1 uptake that are imaged for 20 min. This trend is demonstrated in Fig. 8 by observing the relative height of boxes, specifically the first white and the third black boxes within a column. For locations at which noise and blur are severe, localization is determined primarily by random chance for both 3:1 and 6:1 uptake ratios. In these cases, localization accuracy is similar and poor for the two uptake ratios. This effect is illustrated by the 10.8 mm tumors in the lungs.

Tumor location has a major impact on localization accuracy. In Fig. 8, there is a general trend where localization errors worsen when tumor location changes from anterior to lateral to posterior. As with CNRs, tumor location relative to the detector trajectory can have a larger effect on localization error than radiotracer uptake ratio. These effects are shown in Fig. 8 when making comparisons among stationary tumors near the chest wall of different uptake ratios, and then with

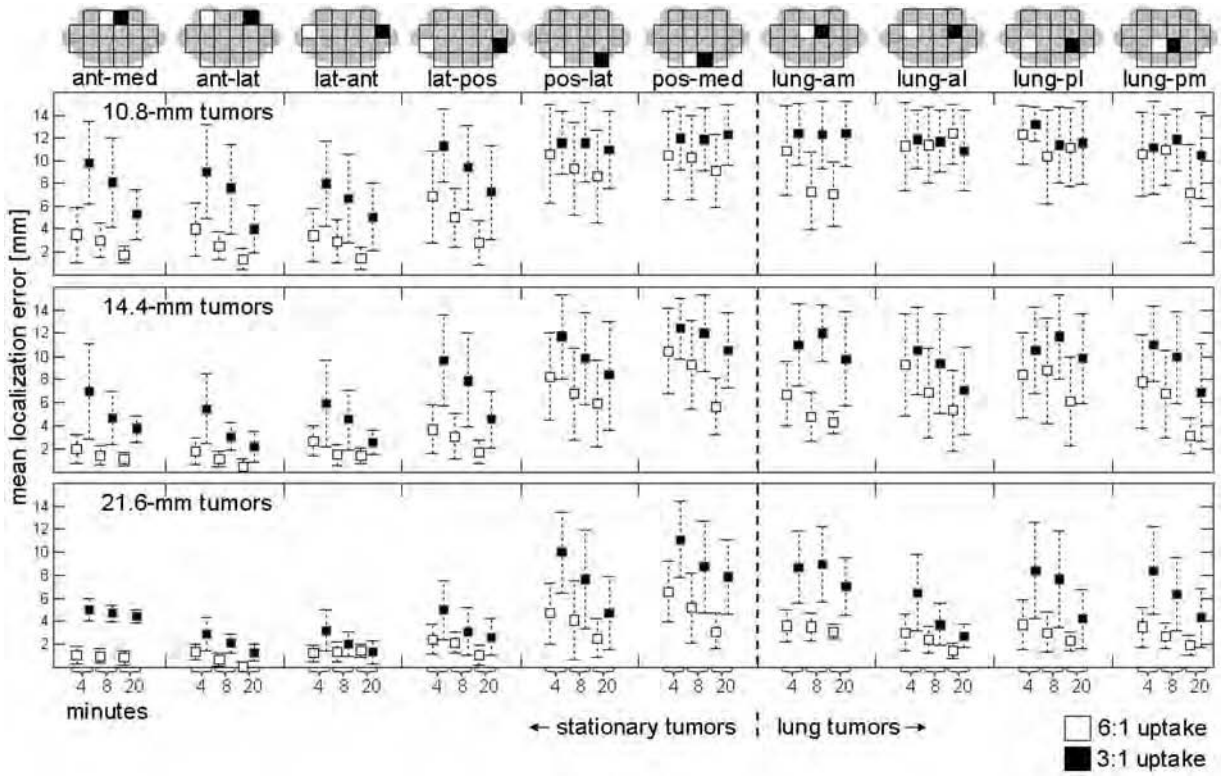

FIG. 8. Ensemble localization errors for different combinations of tumor size, location, radiotracer uptake, and imaging time. Mean errors are displayed as black and white boxes for respective uptake ratios of 3:1 and 6:1. Error bars indicate standard deviations. Tumor sizes are separated by rows and tumor locations by columns. Within each column, there are six data points that correspond with scan times of 4, 8, and 20 min for laterally symmetric tumors of different uptake ratios.

counterparts near the spine and posterior ribs. Though localization is generally poor for posterior tumors, certain results are encouraging. When using relatively short 4 min scans, anterior tumors with diameters of 14.4 and 21.6 mm and 6:1 uptake ratios had mean localization errors less than 2 mm.

III.D. Localization accuracy as a function of contrast-to-noise ratio

Mean localization errors are plotted as a function of CNRs in Fig. 9. There is a noticeable trend. When CNRs are close to zero, localization errors are around 11 mm, which is the expected error when randomly selecting radial locations from a 14.4-mm-radius search volume. In this regime, noise dominates and SPECT provides very little information. As CNRs increase to around 5, localization errors improve rapidly because SPECT is providing more information. Improvements in localization are more modest as CNRs continue to increase. In this region, there is comparatively less to gain from enhancing the already pronounced tumor signal.

There are other more subtle effects in Fig. 9. In the CNR range of 3–5, localization is typically better for tumors of 6:1 than 3:1 uptake. Localization error is generally better for stationary tumor of the same uptake ratio than lung tumors with similar CNRs. Two stationary tumors of 3:1 uptake with relatively high CNRs are noticeably skewed above the other data points. The unexpected degradation in localization error is attributable to proximity to the heart where radiotracer concentrations are much higher and suppress tumor signal inferiorly. These results show potential challenges for localizing targets near a hot background.

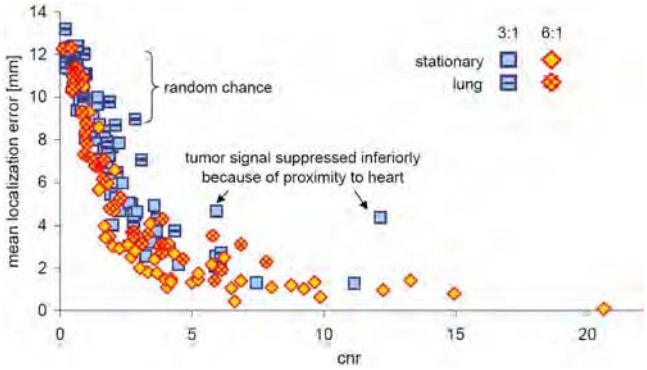

FIG. 9. Mean localization errors plotted as a function of CNRs. Tumors of 3:1 and 6:1 uptakes are differentiated by square and diamond markers. Markers that are crossed signify lung tumors, while solid markers represent stationary tumors.

IV. DISCUSSION

In this simulation study, on-board SPECT was investigated for localizing functional and molecular targets. Several parameters were considered: Scan time and tumor location, diameter, and uptake ratio. Among these, one of the most influential factors was radiotracer uptake in tumor relative to

background: As indicated by CNRs, localization metrics, and visual inspection. Tumors of 6:1 uptake were strikingly more noticeable than their laterally symmetric counterparts of 3:1 uptake. These visual observations were supported by quantitative values—CNRs and localization accuracy. CNRs were on average 1.6 times greater for the tumors of 6:1 radiotracer specificity. The observed ratio of 1.6 is less than the true phantom contrast ratio of 2.5. In the absence of spatial resolution modeling, blurring from limited spatial resolution has a relatively greater impact on contrast recovery of 6:1 tumors compared with those of 3:1 uptake. This result is consistent with the findings of Ref. 32 where scatter, a type of blurring, more substantially reduced the recovered contrast of hotter lesions.

Typically, tumors of 6:1 uptake were localized as accurately using 4 min scans as 3:1 tumors that had been imaged for 20 min. This difference in time has important implications, especially in the context of radiation therapy delivery where short scans are important in minimizing patient motion and ensuring machine throughput. Thus, radiotracer specificity will be an important criterion when selecting or developing potential radiotracers for on-board SPECT imaging. Conversely, diagnostic or treatment-planning SPECT images could be used to estimate tumor characteristics—radiotracer uptake and size—that affect localization in a predictable way in order to gauge whether individual patients would benefit from on-board SPECT. Further, diagnostic or treatment-planning SPECT images could provide radiotracer-concentration templates for estimating localization. Such templates may be particularly useful for localizing tumors with inhomogeneous radiotracer uptake that is comparable in width to, or wider than, the on-board SPECT spatial resolution.

This study utilized a 180° orbit in order to avoid viewing the patient through the couch. Radiation therapy couches are thicker and wider than typical diagnostic imaging couches, such that SPECT data acquired through the couch would be substantially attenuated, and the SPECT detector would be displaced away from the patient, thereby degrading spatial resolution. Averaging over all angles of the 180° orbit, tumors near the chest wall are on average closer to the detector, which implies better spatial resolution, and they are less attenuated by tissue. Because of attenuation, image noise was greater near the spine than the chest wall. Quantum noise is not reversible even with attenuation correction. As is typical for most clinical SPECT imaging, the reconstructions did not model spatial resolution. Consequently, poorer spatial resolution and poorer contrast are expected for the posterior tumors. Modeling spatial resolution would increase image reconstruction time—an important consideration for on-board SPECT. That noted, spatial resolution modeling is worth evaluating in a future study, since it has potential to improve localization.[33] Because localization is better in regions proximal to the detector trajectory and since tumor location is known approximately, on-board SPECT trajectories could be optimized for imaging specific tumor sites.

CNR and localization error are related, but one metric may not necessarily be a good predictor of the other. In this study, noisy reconstructed images were smoothed using Gaussian kernels with FWHMs of 8, 14, and 20 mm. CNRs and localization errors were calculated for noisy images and for images with each degree of smoothing. CNRs improved with smoothing. In contrast, localization errors improved at certain anatomical locations but worsened for others. On average localization errors were comparable across different degrees of smoothing. These results demonstrate that localization errors cannot be estimated directly from CNRs. Encouragingly, these results also suggest that localization accuracy is somewhat robust to smoothing. It follows that they may be robust to iteration number when using iterative reconstruction since smoothness is highly correlated with iteration number. Smoothing did, however, impact localization for certain tumors, and these effects need to be studied further.

CT provides anatomical information that would be valuable for correcting nonuniform attenuation in on-board SPECT images. Attenuation coefficients could be estimated from on-board cone beam CT or from registered CT images.

We do not anticipate that on-board SPECT imaging would be used for every fraction in a highly fractionated treatment because of associated imaging time and patient dose. On-board SPECT is better suited for treatments with a limited number of fractions such as stereotactic body radiation therapy (SBRT). SBRT is used to treat a variety of tumors, including breast oligometastasis.[34,35] For SBRT, imaging time is less of an issue because additional time is allotted for patient positioning as compared with most highly fractioned treatments. Concerning patient dose, a typical 25 mCi injection of ^{99m}Tc-sestamibi[36] results in an effective dose of 7.9 mSv,[37] which is about 1/3 the effective dose of an on-board CBCT chest scan.[38] Cost is also an issue that would have to be evaluated along with any improvements in morbidity and/or mortality through clinical studies.

Localization values may change depending on the coarseness of image voxels or the size of the search volume. In this study, centroids were estimated on a voxelized grid, limited by the half width of a subvoxel. Localization would likely worsen by using a larger search volume with more locations where random noise fluctuations could mimic tumor, particularly for barely visible tumors.

Our simulation study makes absolute estimates regarding localization. Localization values will change—likely for the worse as additional factors such as scatter (estimated to account for 20%–40% of the detected counts in scanner data[39]), tumor diffuseness, and tumor inhomogeneities are considered. Localization accuracy, however, will likely change for the better as trajectories are focused on the target region, as scatter correction is implemented, and as estimation methods are developed specifically for tumor inhomogeneities. This current study contributes as a significant first step, by incorporating a significant degree of realism (e.g., spatial resolution and attenuation), clearly defining that level of realism, and then returning absolute numbers for localization accuracy and precision. Such absolute estimates are necessary in order to access whether on-board SPECT is even

possibly feasible, and these estimates form a baseline which will help in quantifying and understanding the effects of future developments.

V. CONCLUSION

SPECT imaging was investigated for localizing functional and molecular targets immediately prior to radiation therapy. CNRs and localization errors were analyzed as a function of scan time and tumor size, location, and radiotracer uptake using computer simulations. Localization errors were less than 2 mm for certain tumors using relatively short 4 min scans. These encouraging results warrant further investigation of on-board SPECT for localizing functional and molecular targets.

ACKNOWLEDGMENTS

This project was supported in part by NIH Grant No. T32EB007185 from the National Institute of Biomedical Imaging and Bioengineering and by the Department of Defense Breast Cancer Research Program Predoctoral Fellowship (Grant No. BC073559). The content is solely the responsibility of the authors and does not necessarily represent the official views of the National Institute of Biomedical Imaging and Bioengineering, the National Institutes of Health, or the Department of Defense. The authors would like to thank the reviewers for helpful comments which have improved the paper.

[a]Author to whom correspondence should addressed. Electronic mail: justin.roper@duke.edu; Tel.: (919)-688-0489; Fax: (919)-681-7183.

[1]J. D. Chapman, J. D. Bradley, J. F. Eary, R. Haubner, S. M. Larson, J. M. Michalski, P. G. Okunieff, H. W. Strauss, Y. C. Ung, and M. J. Welch, "Molecular (functional) imaging for radiotherapy applications: An RTOG symposium," Int. J. Radiat. Oncol., Biol., Phys. **55**, 294–301 (2003).

[2]C. C. Ling, J. Humm, S. Larson, H. Amols, Z. Fuks, S. Leibel, and J. A. Koutcher, "Towards multidimensional radiotherapy (MD-CRT): Biological imaging and biological conformality," Int. J. Radiat. Oncol., Biol., Phys. **47**, 551–560 (2000).

[3]L. A. Dawson and D. A. Jaffray, "Advances in image-guided radiation therapy," J. Clin. Oncol. **25**, 938–946 (2007).

[4]L. A. Dawson, K. K. Brock, S. Kazanjian, D. Fitch, C. J. McGinn, T. S. Lawrence, R. K. Ten Haken, and J. Balter, "The reproducibility of organ position using active breathing control (ABC) during liver radiotherapy," Int. J. Radiat. Oncol., Biol., Phys. **51**, 1410–1420 (2001).

[5]M. Guckenberger, J. Meyer, J. Wilbert, K. Baier, G. Mueller, J. Wulf, and M. Flentje, "Cone-beam CT based image-guidance for extracranial stereotactic radiotherapy of intrapulmonary tumors," Acta Oncol. **45**, 897–906 (2006).

[6]J. M. Schallenkamp, M. G. Herman, J. J. Kruse, and T. M. Pisansky, "Prostate position relative to pelvic bony anatomy based on intraprostatic gold markers and electronic portal imaging," Int. J. Radiat. Oncol., Biol., Phys. **63**, 800–811 (2005).

[7]S. A. Nehmeh, N. Y. Lee, H. Schroder, O. Squire, P. B. Zanzonico, Y. E. Erdi, C. Greco, G. Mageras, H. S. Pham, S. M. Larson, C. C. Ling, and J. L. Humm, "Reproducibility of intratumor distribution of (18)F-fluoromisonidazole in head and neck cancer," Int. J. Radiat. Oncol, Biol., Phys. **70**, 235–242 (2008).

[8]Z. Keidar, O. Israel, and Y. Krausz, "SPECT/CT in tumor imaging: Technical aspects and clinical applications," Semin. Nucl. Med. **33**, 205–218 (2003).

[9]C. Zhu, "Eighth Asia and Oceania Congress of Nuclear Medicine and Biology," October 9–13, 2004, Beijing, China. J. Nucl. Med. **45**, 13N–16N (2004).

[10]D. J. Yang, E. E. Kim, and T. Inoue, "Targeted molecular imaging in oncology," Ann. Nucl. Med. **20**, 1–11 (2006).

[11]K. T. Cheng, A. Menkens, S. Bryant, and D. C. Sullivan, "NIH MICAD initiative and guest author program opportunities," J. Nucl. Med. **48**, 19N (2007).

[12]M. Hamoudeh, M. A. Kamleh, R. Diab, and H. Fessi, "Radionuclides delivery systems for nuclear imaging and radiotherapy of cancer," Adv. Drug Delivery Rev. **60**, 1329–1346 (2008).

[13]S. K. Imam, "Molecular nuclear imaging: The radiopharmaceuticals," Cancer Biother. Radiopharm. **20**, 163–672 (2005).

[14]R. Schibli and P. A. Schubiger, "Current use and future potential of organometallic radiopharmaceuticals," Eur. J. Nucl. Med. Mol. Imaging **29**, 1529–1542 (2002).

[15]Q. F. Xiong and Y. Chen, "Review: Deoxyglucose compounds labeled with isotopes different from 18-fuoride: Is there a future in clinical practice?," Cancer Biother. Radiopharm. **23**, 376–381 (2008).

[16]W. P. Segars and B. M. Tsui, "Study of the efficacy of respiratory gating in myocardial SPECT using the new 4D NCAT Phantom," IEEE Trans. Nucl. Sci. **49**, 675–679 (2002).

[17]B. M. W. Tsui, W. P. Segars, and D. S. Lalush, "Effects of upward creep and respiratory motion in myocardial SPECT," IEEE Transactions on Nuclear Science **47**(3), 1192–1195 (2000).

[18]A. Spanu, O. Schillaci, and G. Madeddu, "Tc-99m labelled cationic lipophilic complexes in malignant and benign tumors: The role of SPET and pinhole-SPET in breast cancer, differentiated thyroid carcinoma and hyperparathyroidism," Q. J. Nucl. Med. Mol. Imaging **49**, 145–169 (2005).

[19]J. Maublant, M. deLatour, D. Mestas, A. Clemenson, S. Charrier, V. Feillel, G. Le Bouedec, P. Kaufmann, J. Dauplat, and A. Veyre, "Technetium-99m-sestamibi uptake in breast tumor and associated lymph nodes," J. Nucl. Med. **37**, 922–925 (1996).

[20]A. Chiti, L. S. Maffioli, M. Infante, G. Grasselli, M. Incarbone, M. D. Gasparini, G. Savelli, and E. Bombardieri, "Assessment of mediastinal involvement in lung cancer with technetium-99m-sestamibi SPECT," J. Nucl. Med. **37**, 938–942 (1996).

[21]B. Poppe, N. Chofor, A. Ruhmann, W. Kunth, A. Djouguela, R. Kollhoff, and K. C. Willborn, "The effect of a carbon-fiber couch on the depth-dose curves and transmission properties for megavoltage photon beams," Strahlenther. Onkol. **183**, 43–48 (2007).

[22]J. E. Bowsher, D. M. DeLong, T. G. Turkington, and R. J. Jaszczak, "Aligning emission-tomography and MRI images by optimizing the emission-tomography image reconstruction objective function," IEEE Trans. Nucl. Sci. **53**, 1248–1258 (2006).

[23]J. E. Bowsher, M. P. Tornai, J. Peter, D. E. Gonzalez Trotter, A. Krol, D. R. Gilland, and R. J. Jaszczak, "Modeling the axial extension of a transmission line source within iterative reconstruction via multiple transmission sources," IEEE Trans. Med. Imaging **21**, 200–215 (2002).

[24]D. E. G. Trotter, J. Bowsher, and R. Jaszczak, "Absolute quantitation of a spherical I-131 activity distributions using a high-resolution rotating collimator: A phantom study," IEEE Trans. Nucl. Sci. **48**, 65–73 (2001).

[25]C. N. Archer, M. P. Tornai, J. E. Bowsher, S. D. Metzler, B. C. Pieper, and R. J. Jaszczak, "Implementation and initial characterization of acquisition orbits with a dedicated emission mammotomograph," IEEE Trans. Nucl. Sci. **50**, 413–420 (2003).

[26]R. Ter-Antonyan, R. J. Jaszczak, J. E. Bowsher, K. L. Greer, and S. D. Metzler, "Brain SPECT simulation using half-cone-beam collimation and single-revolution helical-path acquisition," IEEE Transactions on Nuclear Science **54**, 475–479 (2007).

[27]H. M. Hudson, B. F. Hutton, and P. Larkin, "Accelerated EM reconstruction using ordered subsets," J. Nucl. Med. **33**, 960 (1992).

[28]A. Seret, "The number of subsets required for OSEM reconstruction in nuclear cardiology," Eur. J. Nucl. Med. Mol. Imaging **33**, 231 (2006).

[29]H. C. Gifford, P. E. Kinahan, C. Lartizien, and M. A. King, "Evaluation of multiclass model observers in PET LROC studies," IEEE Trans. Nucl. Sci. **54**, 116–123 (2007).

[30]H. C. Gifford, M. A. King, P. H. Pretorius, and R. G. Wells, "A comparison of human and model observers in multislice LROC studies," IEEE Trans. Med. Imaging **24**, 160–169 (2005).

[31]C. Lartizien, P. E. Kinahan, and C. Comtat, "Volumetric model and human observer comparisons of tumor detection for whole-body positron emission tomography," Acad. Radiol. **11**, 637–648 (2004).

[32]J. E. Bowsher and C. E. J. Floyd, "Treatment of Compton scattering in maximum-likelihood, expectation-maximization reconstructions of SPECT images," J. Nucl. Med. **32**, 1285–1291 (1991).

[33]H. C. Gifford, M. A. King, R. G. Wells, W. G. Hawkins, M. V. Narayanan, and P. H. Pretorius, "LROC analysis of detector-response compen-

sation in SPECT," IEEE Trans. Med. Imaging **19**, 463–473 (2000).
[34]H. Blomgren, I. Lax, I. Naslund, and R. Svanstrom, "Stereotactic high dose fraction radiation therapy of extracranial tumors using an accelerator. Clinical experience of the first thirty-one patients," Acta Oncol. **34**, 861–870 (1995).
[35]M. T. Milano, A. W. Katz, M. C. Schell, A. Philip, and P. Okunieff, "Descriptive analysis of oligometastatic lesions treated with curative-intent stereotactic body radiotherapy," Int. J. Radiat. Oncol., Biol., Phys. **72**, 1516–1522 (2008).
[36]I. Khalkhali, J. Villanueva-Meyer, S. L. Edell, J. L. Connolly, S. J. Schnitt, J. K. Baum, M. J. Houlihan, R. M. Jenkins, and S. B. Haber, "Diagnostic accuracy of 99mTc-sestamibi breast imaging: multicenter trial results," J. Nucl. Med. **41**, 1973–1979 (2000).
[37]Radiological Protection in Biomedical Research, "A report of Committee 3 adopted by the International Commission on Radiological Protection," Ann. ICRP **22**, 1–28 (1991).
[38]M. W. Kan, L. H. Leung, W. Wong, and N. Lam, "Radiation dose from cone beam computed tomography for image-guided radiation therapy," Int. J. Radiat. Oncol., Biol., Phys. **70**, 272–279 (2008).
[39]Y. S. Gur, T. H. Farncombe, P. H. Pretorius, H. C. Gifford, M. V. Narayanan, E. C. Frey, D. Gagnon, and M. A. King, *Comparison of Scatter Compensation Strategies for Cardiac Perfusion Imaging using Tc-99m labeled sestamibi Nuclear Science Symposium Conference Record*, 2001 (IEEE, 2001), pp. 2188–2192.

Appendix C

JR Roper, JE Bowsher, FF Yin. “Direction-dependent localization errors in SPECT images.” *(accepted for publication in Med. Phys.)*

Accepted for publication in *Medical Physics*

Direction-dependent localization errors in SPECT images

Justin Roper
James Bowsher
Fang-Fang Yin

Medical Physics Graduate Program
Department of Radiation Oncology
Duke University Medical Center
Durham, NC 27710, USA

Corresponding address:

Justin Roper
Medical Physics Graduate Program
Department of Radiation Oncology
Duke University Medical Center
Box 3295 Medical Center
Durham, NC 27710, USA
Email: justin.roper@duke.edu
Tel: (919) 688-0489
Fax: (919) 681-7183

ABSTRACT

Purpose: Single photon emission computed tomography (SPECT) is being investigated for imaging inside radiation therapy treatment rooms to localize biological targets. Here computer simulations were used to analyze locational and directional dependencies in localization errors and to assess the effects of spatial resolution modeling and observer normalization on localization performance.

Methods: SPECT images of the XCAT phantom, containing 12 hot tumors, were reconstructed with detector response function compensation (DRC) and without DRC (nDRC). Numerical observers were forced to select the most suspicious tumor location – using normalized (NXC) or un-normalized (XC) cross correlation – from 3-cm-diameter search volumes that each contained only one tumor. For each tumor site, localization was optimized as a function of iteration number and post-reconstruction smoothing. Localization error – the distance between true and estimated tumor positions – was calculated across the ensembles of 80 images. Direction-dependent localization bias and precision were estimated from the image ensemble.

Results: For the 6 superficial tumors in close proximity to the detector trajectory, mean localization errors were < 2 mm and were lowest or comparable using DRC-NXC, though differences from DRC-XC and nDRC-NXC were not statistically significant. DRC-NXC did provide statistically significantly better localization than nDRC-XC for 5 of these 6 tumors. At the other 6 sites where attenuation was more severe and the distance generally greater between tumor and detector, DRC typically did not show better localization than nDRC. Observer normalization improved localization substantially for

a tumor near the hotter heart. Localization errors were anisotropic and dependent on tumor location relative to the detector trajectory.

Conclusions: This computer-simulation study compared localization performance for normalized and un-normalized numerical observers, which were used to estimate tumor positions in SPECT images, reconstructed with and without DRC. For tumors localized to < 2 mm on average, which are good candidates for SPECT-guided radiation therapy, localization performance typically improved by compensating for the detector response function and by using a normalized observer. The observed direction-dependent localization errors have important implications for radiation therapy and are relevant to SPECT imaging in general.

Keywords: SPECT, localization, direction-dependent localization errors, detector response function compensation, numerical observer

I. INTRODUCTION

Biologically-conformal radiation therapy has been proposed for sculpting dose in regions of high tumor burden, increased growth, and hypoxia.[1] Currently, however, there are no imaging modalities inside radiation therapy treatment rooms that provide functional information for localizing biological targets. In a previous study, we investigated certain aspects of the technical feasibility of using single photon emission computed tomography (SPECT) for the task of localizing biological targets while a patient is on the treatment couch, immediately prior to radiation delivery.[2] In this previous study, SPECT images were reconstructed without compensation for the detector response function, and normalized numerical observers were used to assess localization errors as a function of the location, size, and uptake ratio of hot tumors.

In the present study, the evaluation of localization errors was extended to directional dependencies, which were analyzed relative to the detector trajectory and the attenuating medium. Also evaluated for localization performance were the use of spatial resolution modeling within image reconstruction and the use of normalization in the numerical observer. Assessments of direction-dependent localization errors are important to external beam radiation therapy because radiation is typically delivered from multiple gantry angles.

Related work on spatial resolution modeling includes localization receiver operating characteristic (LROC) studies.[3] These LROC studies involved human observers and computer simulations of ^{67}Ga SPECT tumor imaging using a 360° detector trajectory. Observers considered a broad region of the mediastinum where lymphoma commonly occurs, and LROC performance was averaged over many tumor sites. These studies found improved LROC performance when utilizing SPECT images reconstructed with detector response compensation (DRC), as compared to utilizing images with no DRC (nDRC).

II. METHODS AND MATERIALS

A. Phantom

A female XCAT Phantom, an extended version of the NCAT Phantom[4], was implemented on a grid of 0.15 x 0.15 x 0.15 cm^3 voxels. Twelve, 1.5-cm-diameter tumors were simulated – in axilla, breast, chest wall, lung, rib, vertebra, and other soft tissues – for a broad sampling of locations deep, superficial, anterior, and posterior in an axial slice superior to the heart. Tumor activity concentration was 1.5 μCi/cm^3, based on breast tumor imaging with ^{99m}Tc cardiac perfusion radiotracers.[5] Relative activity ratios

were 20:6:1 for heart, tumor, and other tissues.[5, 6] The simulated activity distribution and the 12 tumor sites labeled A-L are shown in Figure 1. Beneath the supine phantom with raised arms, a flat-top couch was simulated that had a lateral width of 50.5 cm. Attenuation was modeled for 140 keV photons, the emission energy of ^{99m}Tc. Linear attenuation coefficients were as follows for the different structures: lung, 0.043 cm^{-1}; soft tissue, 0.15 cm^{-1}; rib, 0.22 cm^{-1}; vertebra, 0.18 cm^{-1}, and couch 0.25 cm^{-1}. Respiratory and cardiac motions were not modeled.

B. Image Simulation

In SPECT, a collimator is used to select photons emitted in certain directions. The low-energy, high-resolution (LEHR) collimator simulated in this study had circular parallel holes, 0.14 cm in diameter and 2.635 cm in effective length. Hole length l and diameter d determine angles – ϕ (-tan^{-1}(d/l), tan^{-1} (d/l)) – through which rays may pass directly to the detector. Rays perpendicular to the detector surface, where ϕ is zero, have the highest probability of being accepted. Angular ray weights $a(\phi)$ for circular parallel holes are described by

$$a(\phi) = c\left(2\cos^{-1}\left|\frac{l\cdot\tan\phi}{d}\right| - \left|\frac{l\cdot\tan\phi}{d}\right|\sqrt{1-\left|\frac{l\cdot\tan\phi}{d}\right|^2}\right), \qquad (1)$$

where c is a normalization factor.[7]

Figure 2 shows schematics of (a) the collimator hole geometry and (b) the cone of rays used to simulate distance-dependent spatial resolution. The cone of rays was divided into 49 segments of equal area. Rays were weighted by the mean $a(\phi)$ of each segment. Intrinsic blur was modeled with a 2D, 0.32-cm-FWHM Gaussian kernel. Figure 2c shows the agreement between measured and simulated line source profiles at distances of

15 to 30 cm. Profiles – 1.8-cm thick – were drawn perpendicular to the long axis of simulated and physical line sources that were 4 cm in length and 0.1 cm in diameter. The physical source, a capillary tube, was filled with ^{99m}Tc. Measurements were made on a Trionix Triad scanner, equipped with parallel-hole LEHR collimation. Projection images were generated, with detector resolution modeled as just described, using the software SPECT-MAP, which analytically models collimator efficiency, detector efficiency, radioactive decay, isotope branching, non-uniform attenuation, and distance-dependent spatial resolution. Scatter was not modeled in the phantom or detector. Septal penetration was not simulated. SPECT-MAP has been widely utilized and tested.[2, 8-12]

A conformal detector trajectory was defined such that for each detector view, the detector radius was adjusted to achieve 0.5-cm proximity between the patient-side surface of the collimator and the phantom or couch. Detector axial width was considered when varying the detector radius, thereby avoiding collisions with breast, raised arms, and couch. As measured from the detector axis of rotation near the spine, the distance to the collimator surface ranged from a minimum of 23.9 cm in the anterior above the breasts to a maximum of 27.4 cm near the arms. There were 60 detector views over the anterior 180° trajectory, as shown in Figure 3. The simulated 54-cm detector width was sufficiently broad as to avoid image truncation transaxially. In the axial dimension, the simulated detector was more compact at 15 cm than a full-size gamma camera of 40 cm width.[13] Projection bins were 0.15 x 0.15 cm^2. Noise-free projection images were degraded with Poisson noise to simulate 5 seconds of imaging time per detector view. In regions of the detector illuminated by background, i.e., not by heart or tumor,

approximately 8 counts per second were recorded per cm^2. An ensemble of 80 noisy realizations was generated using this detector trajectory.

C. Image Reconstruction

Images were reconstructed using OSEM [14] and then smoothed with a 3D Gaussian filter. For each tumor location and each combination of DRC versus nDRC and normalized versus un-normalized observer, localization was evaluated across a broad range of image updates (*i.e.* products of numbers of iterations and subsets) and of smoothing kernel widths, in order to determine an optimal number of updates and degree of smoothing at each location and for each method of reconstruction and each method of localization estimation. These different methods were compared using the iteration numbers and smoothing widths that were optimal for each method. In the comparison results presented below, four subsets were used to accelerate DRC reconstructions, but only one subset was used for nDRC images because the iteration-number optimization indicated that 1 iteration with 4 subsets gave too many image updates for optimal localization at several tumor sites. Note that one-subset OSEM is MLEM. [14-16] Post-reconstruction smoothing was performed using 3D Gaussian kernels that ranged in FWHM from 0 to 2.5 cm in increments of 0.5 cm. In total, 80 noisy images were reconstructed using 2 variations of OSEM (DRC and nDRC) and smoothed to different degrees with 6 Gaussian kernels at iterations 1-25.

Both reconstruction methods used the same ensemble of noisy projection images. As such, reconstructed images were paired with the only difference being the reconstruction method (DRC or nDRC). For nDRC, central rays were traced perpendicular to the image plane and from each detector bin through the phantom. The

DRC model accounted for distance-dependent collimator spatial resolution and crystal blurring and was matched exactly to that used for simulating projection images. For both reconstruction methods, non-uniform attenuation was calculated along each ray. The attenuation map was ideal. Reconstructed images were implemented on a grid of 0.30 x 0.30 x 0.30 cm^3 voxels.

Tumor positions were estimated in background-subtracted noise-free images, as a method for verifying that tumor positions in reconstructed images were consistent with those in the phantom. Noise-free nDRC and DRC images were reconstructed using the methods described above. Noise-free images without tumor present were used to estimate background activity. In background-subtracted noise-free images, 1.8-cm-diameter ROIs were placed on the 1.5-cm-diameter tumors. The center of mass was calculated for each tumor site and across the 25 iterations. Distances were recorded between the center of a tumor in these images and in the phantom.

D. Localization

Localization was assessed in a forced choice task, where each 3.0-cm-diameter spherical search volume Ω contained one and only one tumor. In the phantom, the tumor was centered in Ω at coordinates (x_t, y_t, z_t). A numerical observer sampled Ω every 0.3 cm in Cartesian space. The voxel with the greatest response and its 26 neighbors were then sampled more finely at every 0.1 cm. The observer selected subvoxel location $i(x_m, y_m, z_m)$ within Ω of noisy image g that produced the greatest scalar response from un-normalized cross correlation (XC) with an observer template w:

$$i(x_m, y_m, z_m) = \arg\max_{i \in \Omega} (\mathrm{XC}_i), \tag{2}$$

where

$$\mathrm{XC}_i = w \cdot g_i. \tag{3}$$

Thus, location (x_m, y_m, z_m) was recorded as the measured tumor position. The 3D template w was a sphere – the background-subtracted tumor signal as defined in the XCAT activity phantom. Template dimensions were 1.5 x 1.5 x 1.5 cm^3. The same template w was used for all 12 tumor sites and for both reconstruction methods and variations of cross correlation. Note that the spherical template was not matched exactly to a tumor because tumor appearance in the SPECT images was distorted due to the effects of distance-dependent spatial resolution, iteration number, and post-reconstruction smoothing.

Normalized cross correlation (NXC) was also investigated for estimating tumor positions:

$$\mathrm{NXC}_i = \frac{w \cdot g_i}{\sqrt{(w \cdot w)(g_i \cdot g_i)}}. \tag{4}$$

Localization error dr was calculated as the Euclidean distance between a true tumor position and a measured tumor position:

$$dr = \sqrt{(x_t - x_m)^2 + (y_t - y_m)^2 + (z_t - z_m)^2}. \tag{5}$$

Localization error dr is always positive and also discrete due to the 0.1-cm sampling on a Cartesian grid. Localization errors were recorded across the noisy image ensembles for each tumor site. Localization errors were compared for DRC-XC, DRC-NXC, nDRC-XC, and nDRC-NXC using site-specific optimal smoothing and iteration number parameters. Differences in ensemble localization errors were assessed for statistical significance using the Wilcoxon signed-rank test.

For each tumor site, direction-dependent localization errors were computed every 3° over 180°. These errors were indexed by an angle θ. Angle θ was defined in a transaxial plane as follows: θ was equal to 0 for the view from left lateral to center of rotation, $\pi/2$ for the anterior view, and π for the right lateral view. Direction-dependent localization bias ($b^{\perp\theta}$) and precision ($\sigma^{\perp\theta}$), indexed to a specific value of θ, were calculated along the dimension perpendicular to θ. As such, localization precision at the anterior view described the lateral spread of localization errors, and localization bias – the lateral bias. Figure 4 illustrates this convention using data from tumor G. The direction-dependent localization errors were defined mathematically as follows: Measured tumor coordinates $\left(x_{m,k},\ y_{m,k}\right)$ from noisy image k and true tumor coordinates $\left(x_t,\ y_t\right)$ were rotated by angle θ using matrix T:

$$T = \begin{bmatrix} \cos\theta & -\sin\theta \\ \sin\theta & \cos\theta \end{bmatrix} \tag{6}$$

to yield

$$\begin{bmatrix} x_{m,k}^{\theta} \\ y_{m,k}^{\theta} \end{bmatrix} = T \begin{bmatrix} x_{m,k} \\ y_{m,k} \end{bmatrix} \tag{7}$$

and

$$\begin{bmatrix} x_t^{\theta} \\ y_t^{\theta} \end{bmatrix} = T \begin{bmatrix} x_t \\ y_t \end{bmatrix}. \tag{8}$$

For the direction perpendicular to θ, direction-dependent localization bias $b^{\perp\theta}$ was calculated as

$$b^{\perp\theta} = \frac{1}{N}\sum_{k=1}^{N=80}\left(y_{m,k}^{\theta} - y_t^{\theta}\right) \tag{9}$$

and direction-dependent localization precision $\sigma^{\perp\theta}$ as

$$\sigma^{\perp\theta} = \sqrt{\frac{1}{N-1}\sum_{k=1}^{N=80}\left(y_{m,k}^{\theta} - \overline{y_m^{\theta}}\right)^2}, \tag{10}$$

where

$$\overline{y_m^{\theta}} = \frac{1}{N}\sum_{k=1}^{N=80} y_{m,k}^{\theta}. \tag{11}$$

For each angle θ, direction-dependent localization precision and bias were analyzed with respect to the tumor-collimator distance $d^{\perp\theta}$ and also with reference to $\gamma^{\perp\theta}$ – the fraction of photons from a tumor emitted towards the detector not attenuated by the phantom. These metrics are related to distance-dependent spatial resolution and attenuation of tumor signal.

III. RESULTS

A. Reconstructed Images

Noisy OSEM images were smoothed with 3D Gaussian kernels, ranging from 0 to 2.5 cm in FWHM, at iterations 1-25. Representative nDRC and DRC images, reconstructed from the same projection set, are displayed on the same gray scale in Figure 5. Anterior, superficial tumors appear hotter in DRC images than in nDRC images. With greater smoothing, the heart begins to appear near tumor site I. Noise texture differed between nDRC and DRC images. Figure 6 shows ensemble-average images.

Distances were recorded between tumor positions in the XCAT phantom and in noise-free background-subtracted reconstructed images. For DRC images, the mean distance and standard deviation were 0.106 +/- 0.068 mm, as calculated across the 12 tumor sites and 25 iterations. The mean distance was 0.128 +/- 0.060 mm in nDRC images. These shifts in tumor positions are relatively small compared with the localization errors reported in this study below.

B. Localization

The mean localization error was calculated from the 80-image ensemble for each tumor site, reconstruction method, variation of cross correlation, iteration number, and degree of smoothing. Mean localization errors are mapped out as a function of these parameters in Figure 7 where darker color signifies better localization. A white crossed box marks the combination of iteration number and smoothing that resulted in the lowest mean localization. Subsequent comparisons were performed using these optimal parameter values. In Table I, optimal combinations of smoothing and iteration number are listed with corresponding mean localization errors.

Localization errors – calculated across the 80-image ensemble using Eq. (5) – are summarized in Figure 8. The four combinations of reconstruction method and cross correlation – nDRC-XC, nDRC-NXC, DRC-XC, DRC-NXC – are represented by four boxplots at each tumor site. Each box plot includes 80 localization estimates. Also shown is a box plot representing random chance – the uniform probability of selecting any discrete 0.1-cm-spaced location within a 3-cm-diameter search volume centered on tumor. The random chance boxplot shows that more than 75% of potential tumor locations are 9 mm or farther from a true tumor position and thereby serves as a useful

benchmark for gauging the amount of information provided by SPECT for target localization. Note that localization appears worse than expected due to random chance at tumor site I using un-normalized cross correlation because the numerical observer selects the much hotter heart.

Ensemble localization errors are described more completely by plotting the fraction of correct localizations within a radial distance from a true tumor position, as illustrated in Figure 9. Two tumor sites – one each of relatively good and relatively poor localization – are plotted together. For reference, and as described above, the random chance curve is plotted in black. In these plots, localization is better for a curve that is above and to the left of another.

The Wilcoxon signed-rank test was used to assess for significant differences in ensemble localization errors at each tumor site between nDRC-XC, nDRC-NXC, DRC-XC, and DRC-NXC. P-values are reported in Table II, with values less than 0.05 in bold. Localization was the worst, and significantly so, using nDRC-XC at tumor sites A, B, C, D, and F. At these sites, mean localization was best using DRC-NXC (Table I); however, localization differences were not statistically significantly different than DRC-XC and nDRC-NXC at each site. Near the heart at site I, NXC was significantly better than XC. Localization performance was best using nDRC for sites H, J, and L.

In Figure 10, tumor position estimates are overlaid on the attenuation map. There are 80 markers at each tumor site encompassing estimates from the image ensemble. Localization error patterns depend largely on the tumor site. For instance at site B in the right breast, position estimates are tightly clustered near the true tumor position. In contrast, position estimates are distributed more diffusely at site G in the right posterior

rib where there was a noticeable anisotropy. Note the similarity between localization patterns in Figure 10 and the appearance of reconstructed tumors in Figure 6.

Localization was performed in 3D images reconstructed from all detector views. The quality of information from specific detector views was predictive of direction-dependent localization error. This effect is illustrated in Figure 11 where position estimates at site G are plotted with reference to the detector trajectory. Target localization was more precise when the detector was in close proximity to tumor as compared with a more distal, orthogonal view.

Anisotropies in localization patterns were quantitatively analyzed by calculating direction-dependent localization bias $b^{\perp\theta}$ and precision $\sigma^{\perp\theta}$ as a function of angle θ, using Eqs. (9,10). Directional dependencies of $b^{\perp\theta}$ and $\sigma^{\perp\theta}$ are summarized for each tumor site in Figure 12. Beneath localization bias and precision plots are two additional curves: One curve marks the distance $d^{\perp\theta}$ between tumor position and patient-side surface of the collimator at θ. The other, filled curve shows attenuation survival probability $\gamma^{\perp\theta}$ along θ. Attenuation survival probability is the fraction of photons emitted from the tumor towards the detector not attenuated by the phantom. Direction-dependent localization bias and precision tend to be best along directions θ with low values of $d^{\perp\theta}$ and high values of $\gamma^{\perp\theta}$, particularly at sites A-F. Values of $d^{\perp\theta}$ and $\gamma^{\perp\theta}$ were averaged over the detector trajectory and are reported in Table III.

IV. DISCUSSION

In a previous computer-simulation study, we investigated localization performance in SPECT images as a function of scan time, tumor size, tumor-to-background uptake ratio, and tumor position.[2] In the present study, localization

performance was compared for two reconstruction methods – nDRC and DRC – and two variations of cross correlation – XC and NXC – between the observer template and SPECT images. In addition, localization error patterns were analyzed for directional dependencies. Metrics were developed to describe direction-dependent localization bias and precision. These directional errors were related to the detector trajectory.

In this study, localization performance was assessed using numerical observers that had no knowledge of noise correlations. As such, the observers were suboptimal. Prewhitening of noise correlations may improve localization performance. Though prewhitening presents practical challenges, methods for rapidly computing the noise covariance matrix and for using channels to reduce covariance dimensions are areas of active research.[17-19] That noted, for the detection of hot spheres in unknown locations, non-channelized, non-prewhitening matched filters have been shown to outperform human, channelized non-prewhitening, and channelized Hotelling observers.[20] Though channelized observers can better match human performance by using only information in certain frequency channels [20], it was not our objective here to match human performance.

The non-prewhitening matched filter can be defined as $w_{NPW} = g_i - g_o$, where g_i and g_o are expected values for tumor-present and tumor-absent images and w_{NPW} – the expected difference – is an image of the tumor.[21] Thus, the non-prewhitening matched filter accounts for location-dependent distortions of the tumor appearance in a SPECT image. In practice clinically, the matched filter may not be obtainable. In recognition of this limitation, the template used in this study approximated the matched filter with a sphere. Localization performance might be different using the non-prewhitening matched filter or another observer template instead of a spherical template. In some

clinical scenarios, it may be that a tumor template which better approximates the matched filter could be estimated from a treatment planning SPECT image.

Comparisons in localization performance were made between nDRC-XC, nDRC-NXC, DRC-XC, and DRC-NXC for the iteration number and degree of smoothing that yielded the lowest mean localization error. Post-reconstruction smoothing of SPECT images with Gaussian kernels has been shown to improve LROC performance.[22] In this study, smoothing improved localization in 38 of the 48 cases, as evaluated across the 12 tumor sites and the 4 combinations of reconstruction method and variation of cross correlation. At each tumor site, smoothing was always helpful for NXC. The degree of smoothing optimal for localization was largely determined by the type of cross correlation – NXC versus XC. NXC localization was optimized by Gaussian kernels of approximately three times greater width than those optimal for XC. This can be understood as follows: Smoothing causes activity outside of the search volume, or lack thereof for tumors near body contours, to be blurred into the search volume thus creating activity gradients. XC – the (un-normalized) inner product – is biased by such gradients, much more so than NXC. For example, NXC localization is much better than XC localization at tumor site I, which is near the heart. By allowing for greater smoothing than XC, NXC may also minimize the effects of high frequency noise. Iteration number was optimized in conjunction with smoothing. A greater number of image updates (product of the number iterations and number of subsets) were needed for optimal localization in DRC than in nDRC images. These results are consistent with the findings of other SPECT studies.[3, 23] In two cases, localization performance was best at iteration 25. In the absence of normalization, the XC observer selected the much hotter heart

instead of tumor I. It is possible that at higher iteration numbers, cardiac activity would be pulled out of the search volume, thereby resulting in better localization performance.

At superficial tumor sites A-F, which were proximal to the detector trajectory, localization performance was either comparable or best using DRC-NXC. However, differences in localization results were not statistically significantly different from DRC-XC and nDRC-NXC at each tumor site. At all of these 6 sites except for E, localization was worst, and significantly so, using nDRC-XC. At the other 6 sites where attenuation was 2.9 times more severe and the collimator 1.4 times farther from tumor on average, DRC typically did not result in better localization than nDRC. Though DRC improved localization at G, localization was worse using DRC for lung tumors H and J, and for L near the spine. These differences were statistically significant. Study results support using DRC and/or NXC for localization of proximal, superficial tumors. This study did not compare DRC and nDRC images for the task of determining the size or extent of tumor, though such a comparison is relevant since certain biological targets, e.g., hypoxia, can vary with time.[24]

Tumor proximity to the detector trajectory had a major effect on localization errors, generally more so than the reconstruction method or type of cross correlation. Close detector proximity improves spatial resolution, and though attenuation only depends on the material between the detector and tumor, it too is typically best at views of close detector approach. At site K, mean localization error was very poor; however, K was at a comparable depth in the phantom as other tumors, e.g., E and G, that had vastly better localization because of closer proximity to the detector trajectory. Although the

375 couch will limit detector approach and attenuate photons, localization of K may be improved by using a posterior detector trajectory.

Localization error patterns were anisotropic. Close detector proximity to a tumor and minimal attenuation were good predictors of a direction with the best localization bias and precision. The direction-dependent localization pattern at site G is interesting in
380 that localization is relatively good in one dimension but very poor orthogonally. This information is not conveyed when only using distances to describe localization errors. Strong directional dependencies have important implications for external beam radiation therapy since radiation is often delivered from multiple gantry angles.

The optimal iteration numbers and smoothing parameters used in the above
385 comparisons may not be known in clinical applications. Figure 7 shows that there are often broad regions across the 2D iteration-number / smoothing-parameter space over which localization accuracy is near to its optimal value. This may facilitate successful application of practical clinical techniques such as identifying an iteration number and degree of smoothing that work well across a broad range of patients and anatomical
390 locations, perhaps with some parameterization based on factors such as patient diameter, tumor depth, and tumor-to-background uptake ratio. That noted, clinical localization may not generally be able to achieve the optimal performance used in the above comparison studies. We note that other applications of SPECT, such as quantification and detection, are also often performed clinically using suboptimal smoothing and numbers of iterations.

395 This study used an ideal attenuation map. If implemented clinically, attenuation maps could be derived from an offline CT, registered with SPECT or CBCT, or from on-board MV or kV CBCT. Because these x-ray beams are polychromatic and ^{99m}Tc is

monochromatic, the SPECT attenuation map cannot be measured directly, but it can be calculated.[25] CBCT images are, however, subject to artifacts caused by insufficient sampling, beam hardening, and scatter. Inaccuracies in attenuation maps can cause errors in SPECT images.[26] Further investigation is needed to determine the effect of an imperfect attenuation map on localization performance. The simulated detector had ideal scatter rejection. Scatter has been shown to degrade LROC performance, though this effect can be lessened by compensating for scatter during image reconstruction.[27]

V. CONCLUSIONS

This computer-simulation study compared localization performance for normalized and un-normalized numerical observers, which were used to estimate tumor positions in SPECT images, reconstructed with and without DRC. For tumors localized to < 2 mm on average, which are good candidates for SPECT-guided radiation therapy, localization performance typically improved by compensating for the detector response function and by using a normalized observer. Localization errors were analyzed across the image ensemble and were found to be anisotropic and dependent on tumor position relative to the detector trajectory. Directional dependencies are attributable to the effects of attenuation and distance-dependent spatial resolution. Direction-dependent localization error patterns have important implications for radiation therapy and are relevant to SPECT imaging in general.

VI. ACKNOWLEDGMENTS

This project was supported in part by a predoctoral traineeship W81XWH-08-1-0365 from the Department of Defense Breast Cancer Research Program. The content is solely the responsibility of the authors and does not necessarily represent the official

views of the Department of Defense. The authors would also like to acknowledge insightful comments from Drs. Shiva Das, Janet Horton and Timothy Turkington.

FIGURE CAPTIONS

FIG. 1. (a) Simulated activity ratios were 20:6:1 in heart, tumor, and other tissues. (b) Twelve tumor sites, labeled A-L, were in axial slice superior to heart.

FIG. 2. (a) LEHR collimator hole geometry – length l of 2.635 cm and diameter d of 0.140 cm – determines angles ϕ through which rays may pass directly to the detector. (b) Cones of 49 rays were used to simulate distance-dependent collimator spatial resolution. (c) Shows agreement between simulated and measured line-source profiles at distances of 15 to 30 cm. Measurements were made with a Trionix Triad scanner using LEHR collimation.

FIG. 3. The conformal 180° detector trajectory is overlaid on the attenuation map. At the 60 detector views, a circle marks the collimator position. The detector width is indicated by gray bars at the right lateral and anterior views where distances to the axis of rotation are 25.7 cm and 23.9 cm respectively.

FIG. 4. (a) An anisotropic localization error pattern is marked by filled diamonds. (b) Direction-dependent localization precision $\sigma^{\perp\theta}$ is indexed by θ. Note that θ is also shown above.

FIG. 5. Representative images (nDRC, DRC) reconstructed using the same projection data are displayed as function of iteration number and degree of post-reconstruction smoothing.

FIG. 6. (a) nDRC and (b) DRC images were averaged over the 80-image ensemble at iteration number 10. Spherical tumors appear elliptical and vary in orientation and degree of eccentricity. Distortions are related to tumor position relative to the detector trajectory.

FIG. 7. Mean localization error *dr* for tumor sites A-L is plotted as a function of smoothing, iteration number, reconstruction method, and cross correlation. Within each broad column and row, mean localization error is displayed as a function of iteration number (1-25) on the horizontal axis and smoothing (0 to 2.5-cm-FWHM) on the vertical axis. Labeled axes are shown above the phantom, using tumor F, DRC-XC as an example. The combination of iteration number and smoothing with the best mean localization error is marked by a white crossed box.

FIG. 8. Box plots summarize the ensemble localization errors of tumors A-L. Black horizontal bars denote medians, filled rectangles the interquartile range (IQR), whiskers the last data point within 1.5 x IQR from the 25^{th} and 75^{th} percentiles, and filled markers the outliers. Marked by * is a boxplot representing random chance.

FIG. 9. The fraction of correct localizations is plotted as a function of radius from the true tumor location. Dashed lines represent normalized cross correlation, solid lines un-

normalized cross correlation. DRC lines are lighter than nDRC counterparts. Localization by random chance is shown by a black curve.

FIG. 10. Estimates of tumor positions from the image ensembles are plotted on the attenuation map. For reference, tumor diameters are marked by solid white lines and search region boundaries by dotted white lines. Correct localizations are centered exactly in these circles.

FIG. 11. (a) The detector is highlighted at two views – one proximal to tumor and the other more distal and orthogonal. (b) Position estimates at site G show that more precise localization is associated with a more proximal detector view where spatial resolution was relatively good and attenuation less severe.

FIG. 12. (a) Direction-dependent localization bias and precision are plotted as a function of θ for tumors A-F. Horizontal dashed lines mark ideal bias and precision. Also plotted are curves showing tumor-collimator proximity and the survival probability for photons from a tumor to escape the phantom without being attenuated. (b) Shows results for tumors G-L. Direction-dependent localization bias curve is truncated at site I.

TABLE CAPTIONS

TABLE I. Mean localization errors are reported with optimal combinations of smoothing and iteration number.

TABLE II. Differences in ensemble localization errors were assessed using Wilcoxon signed-rank test. Bold indicates $p < 0.05$.

TABLE III. Average tumor-collimator distance $d^{\perp\theta}$ and attenuation survival probability $\gamma^{\perp\theta}$ are reported for tumors A-L.

REFERENCES

1. C. C. Ling, J. Humm, S. Larson, H. Amols, Z. Fuks, S. Leibel and J. A. Koutcher, "Towards multidimensional radiotherapy (MD-CRT): biological imaging and biological conformality," International Journal of Radiation Oncology Biology Physics **47**, 551-560 (2000).
2. J. Roper, J. Bowsher and F. F. Yin, "On-board SPECT for localizing functional targets: a simulation study," Medical Physics **36**, 1727-1735 (2009).
3. H. C. Gifford, M. A. King, R. G. Wells, W. G. Hawkins, M. V. Narayanan and P. H. Pretorius, "LROC analysis of detector-response compensation in SPECT," IEEE Transactions on Medical Imaging **19**, 463-473 (2000).
4. W. P. Segars and B. M. Tsui, "Study of the efficacy of respiratory gating in myocardial SPECT using the new 4D NCAT Phantom," IEEE Transactions on Nuclear Science **49**, 675-679 (2002).
5. C. N. Brzymialkiewicz, M. P. Tornai, R. L. McKinley and J. E. Bowsher, "Evaluation of fully 3-D emission mammotomography with a compact cadmium zinc telluride detector," IEEE Transactions on Medical Imaging **24**, 868-877 (2005).
6. J. Maublant, M. deLatour, D. Mestas, A. Clemenson, S. Charrier, V. Feillel, G. Le Bouedec, P. Kaufmann, J. Dauplat and A. Veyre, "Technetium-99m-sestamibi uptake in breast tumor and associated lymph nodes," Journal of Nuclear Medicine **37**, 922-925 (1996).
7. G. L. Zeng, G. T. Gullberg, B. M. W. Tsui and J. A. Terry, "Three-dimensional iterative reconstruction algorithms with attenuation and geometric point response correction," IEEE Transactions on Nuclear Science **38**, 693-702 (1991).
8. C. N. Archer, M. P. Tornai, J. E. Bowsher, S. D. Metzler, B. C. Pieper and R. J. Jaszczak, "Implementation and initial characterization of acquisition orbits with a dedicated emission mammotomograph," IEEE Transactions on Nuclear Science **50**, 413-420 (2003).
9. J. E. Bowsher, D. M. DeLong, T. G. Turkington and R. J. Jaszczak, "Aligning emission tomography and MRI images by optimizing the emission-tomography image reconstruction objective function," IEEE Transactions on Nuclear Science **53**, 1248-1258 (2006).
10. J. E. Bowsher, M. P. Tornai, J. Peter, D. E. Gonzalez Trotter, A. Krol, D. R. Gilland and R. Jaszczak, "Modeling the axial extension of a transmission line source within iterative reconstruction via multiple transmission sources," IEEE Transactions on Medical Imaging **21**, 200-215 (2002).
11. R. Ter-Antonyan, R. J. Jaszczak, J. E. Bowsher, K. L. Greer and S. D. Metzler, "Brain SPECT Simulation Using Half-Cone-Beam Collimation and Single-Revolution Helical-Path Acquisition," IEEE Transactions on Nuclear Science **54**, 475-479 (2007).
12. D. E. G. Trotter, J. E. Bowsher and R. J. Jaszczak, "Absolute quantitation of a spherical I-131 activity distribution using a high-resolution rotating collimator: a phantom study," IEEE Transactions on Nuclear Science **48**, 65-73 (2001).
13. M. T. Madsen, "Recent advances in SPECT imaging," Journal of Nuclear Medicine **48**, 661-673 (2007).

14. H. M. Hudson and R. S. Larkin, "Accelerated Image-Reconstruction Using Ordered Subsets of Projection Data," IEEE Transactions on Medical Imaging **13**, 601-609 (1994).
15. K. Lange and R. Carson, "EM reconstruction algorithms for emission and transmission tomography," Journal of Computer Assisted Tomography **8**, 306-316 (1984).
16. Y. Vardi, L. A. Shepp and L. Kaufman, "A Statistical-Model for Positron Emission Tomography," Journal of the American Statistical Association **80**, 8-20 (1985).
17. P. Khurd and G. Gindi, "LROC model observers for emission tomographic reconstruction," Medical Imaging 2004: Image Perception, Observer Performance, and Technology Assessment **5372**, 509-520 (2004).
18. P. Bonetto, J. Y. Qi and R. M. Leahy, "Covariance approximation for fast and accurate computation of channelized Hotelling observer statistics," IEEE Transactions on Nuclear Science **47**, 1567-1572 (2000).
19. B. D. Gallas and H. H. Barrett, "Validating the use of channels to estimate the ideal linear observer," Journal of the Optical Society of America a-Optics Image Science and Vision **20**, 1725-1738 (2003).
20. H. C. Gifford, M. A. King, P. H. Pretorius and R. G. Wells, "A comparison of human and model observers in multislice LROC studies," IEEE Transactions on Medical Imaging **24**, 160-169 (2005).
21. H. H. Barrett, T. Gooley, K. Girodias, J. Rolland, T. White and J. Yao, "Linear Discriminants and Image Quality," Image and Vision Computing **10**, 451-460 (1992).
22. R. G. Wells, P. H. Simkin, P. F. Judy, M. A. King, H. Pretorius and H. C. Gifford, "Effect of filtering on the detection and localization of small Ga-67 lesions in thoracic single photon emission computed tomography images," Medical Physics **26**, 1382-1388 (1999).
23. D. S. Lalush and B. M. W. Tsui, "Mean-variance analysis of block-iterative reconstruction algorithms modeling 3D detector response in SPECT," IEEE Transactions on Nuclear Science **45**, 1280-1287 (1998).
24. S. A. Nehmeh, N. Y. Lee, H. Schroder, O. Squire, P. B. Zanzonico, Y. E. Erdi, C. Greco, G. Mageras, H. S. Pham, S. M. Larson, C. C. Ling and J. L. Humm, "Reproducibility of intratumor distribution of F-18-fluoromisonidazole in head and neck cancer," International Journal of Radiation Oncology Biology Physics **70**, 235-242 (2008).
25. H. Zaidi and B. Hasegawa, "Determination of the attenuation map in emission tomography," Journal of Nuclear Medicine **44**, 291-315 (2003).
26. S. Goetze and R. L. Wahl, "Prevalence of misregistration between SPECT and CT for attenuation-corrected myocardial perfusion SPECT," Journal of Nuclear Cardiology **14**, 200-206 (2007).
27. T. H. Farncombe, H. C. Gifford, M. V. Narayanan, P. H. Pretorius, E. C. Frey and M. A. King, "Assessment of scatter compensation strategies for (67)Ga SPECT using numerical observers and human LROC studies," Journal of Nuclear Medicine **45**, 802-812 (2004).

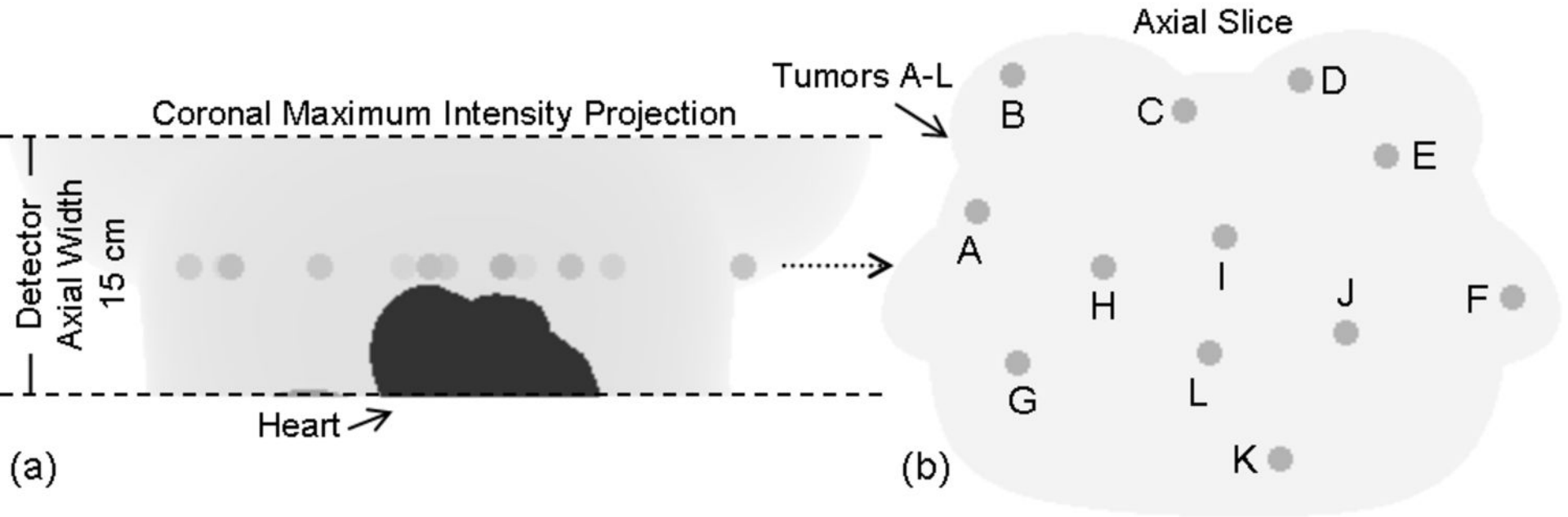
Coronal Maximum Intensity Projection
Detector Axial Width 15 cm
Heart
(a)
Tumors A-L
Axial Slice
A
B
C
D
E
F
G
H
I
J
K
L
(b)

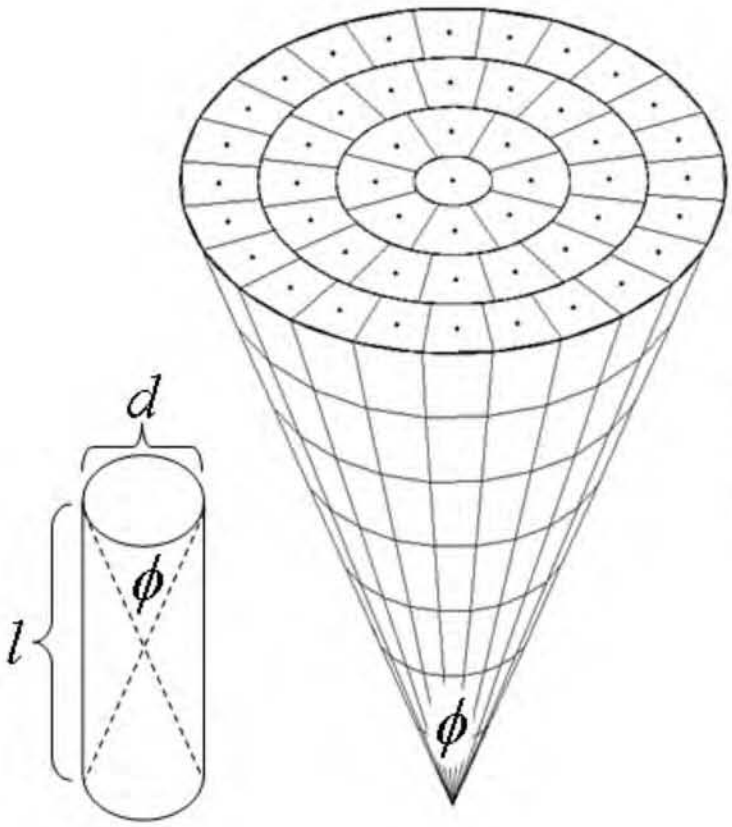
d
l
ϕ
ϕ

(a) (b)

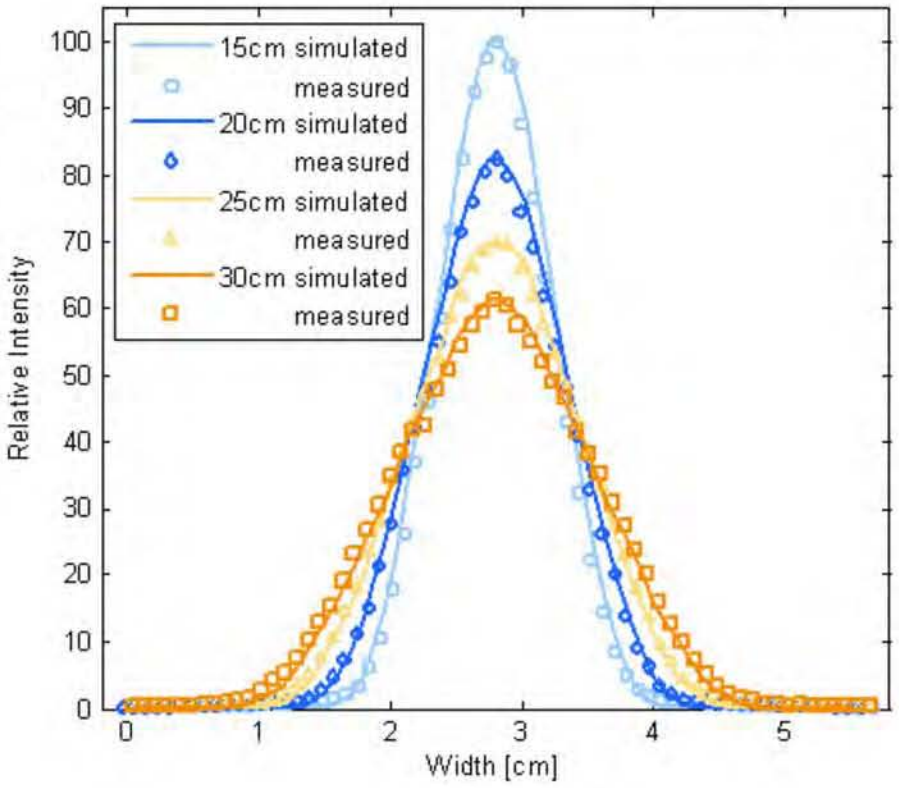
15cm simulated
measured
20cm simulated
measured
25cm simulated
measured
30cm simulated
measured
Relative Intensity
Width [cm]
0
10
20
30
40
50
60
70
80
90
100
0
1
2
3
4
5

(c)

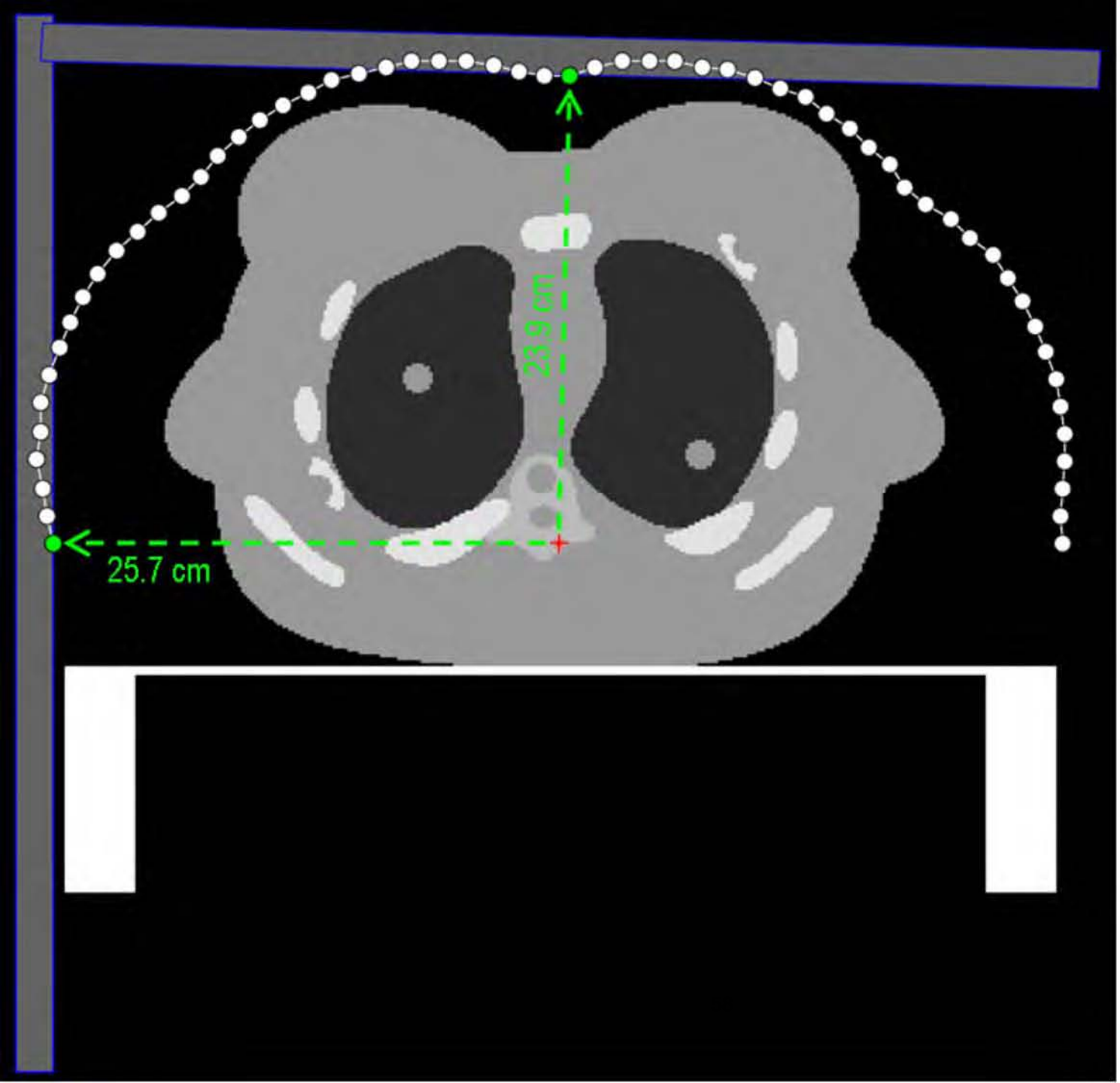
23.9 cm
25.7 cm

Anterior
π/2
θ2
θ1
Right Lateral
π
0
Left Lateral
(a)
Localization Precision σ⊥θ
R
θ1
A
θ2
L
(b)

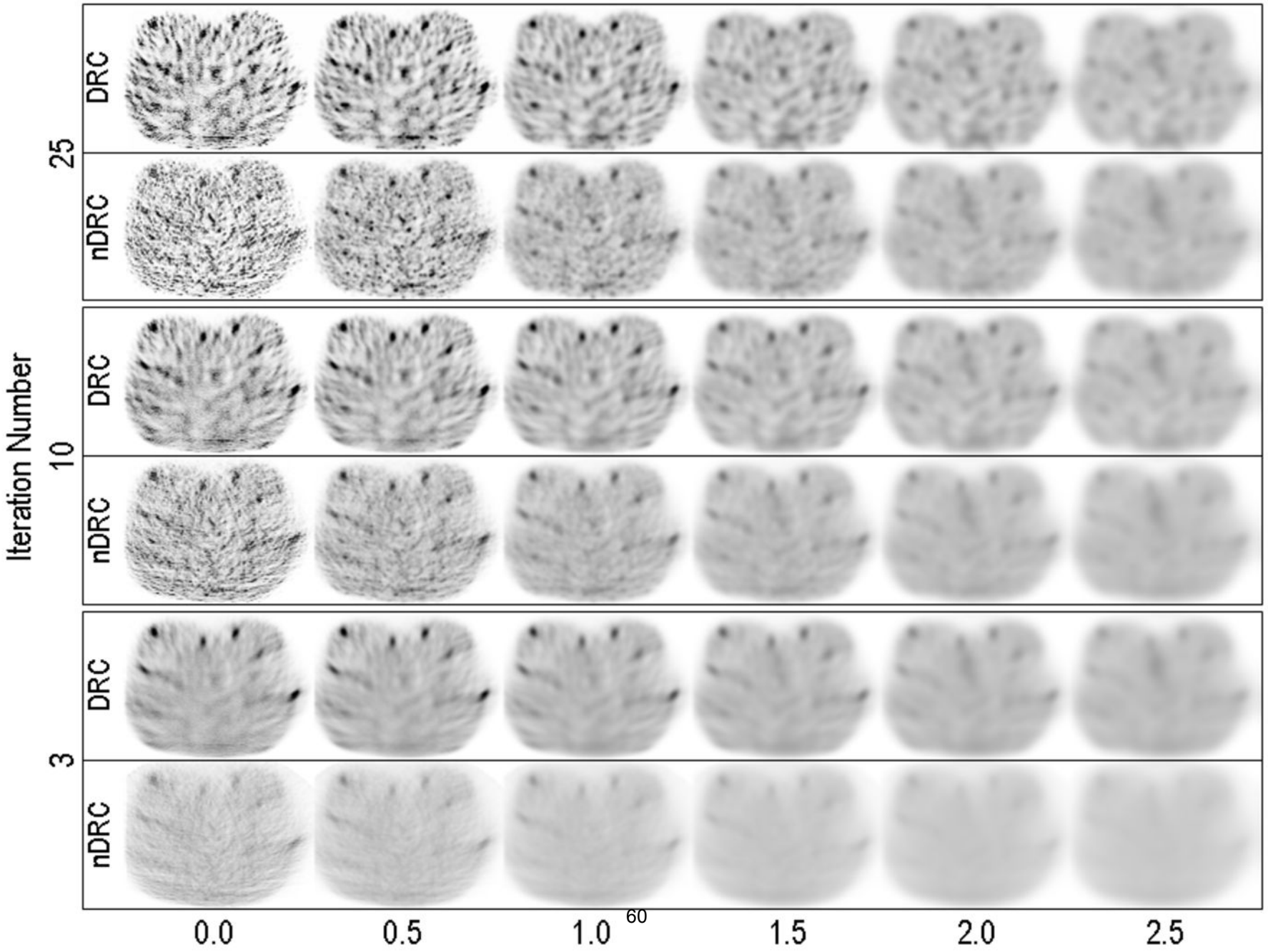
Iteration Number
25
10
3
DRC
nDRC
0.0
0.5
1.0
1.5
2.0
2.5
Post-Reconstruction Smoothing: 3D Gaussian FWHM [cm]

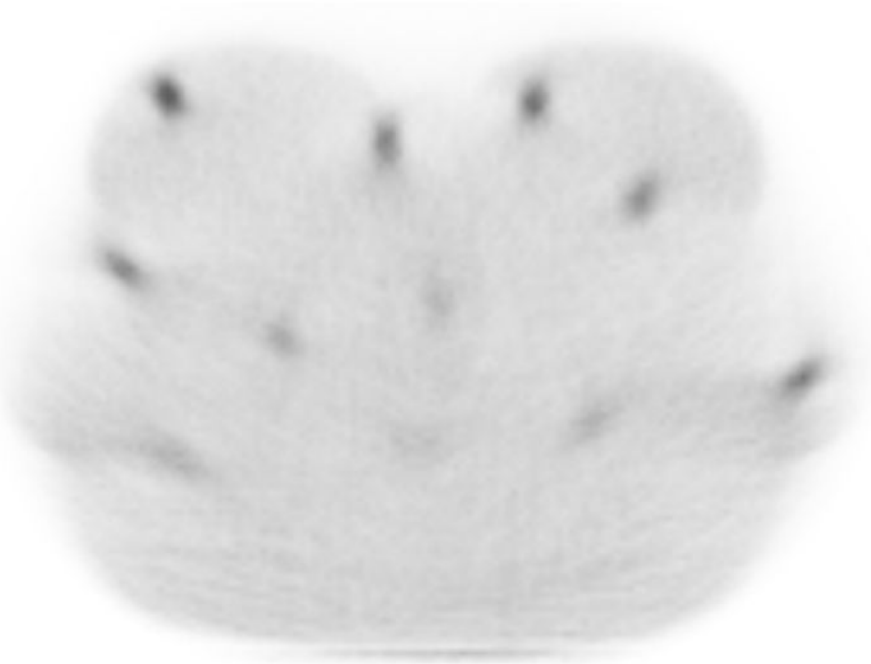

(a) nDRC

(b) DRC

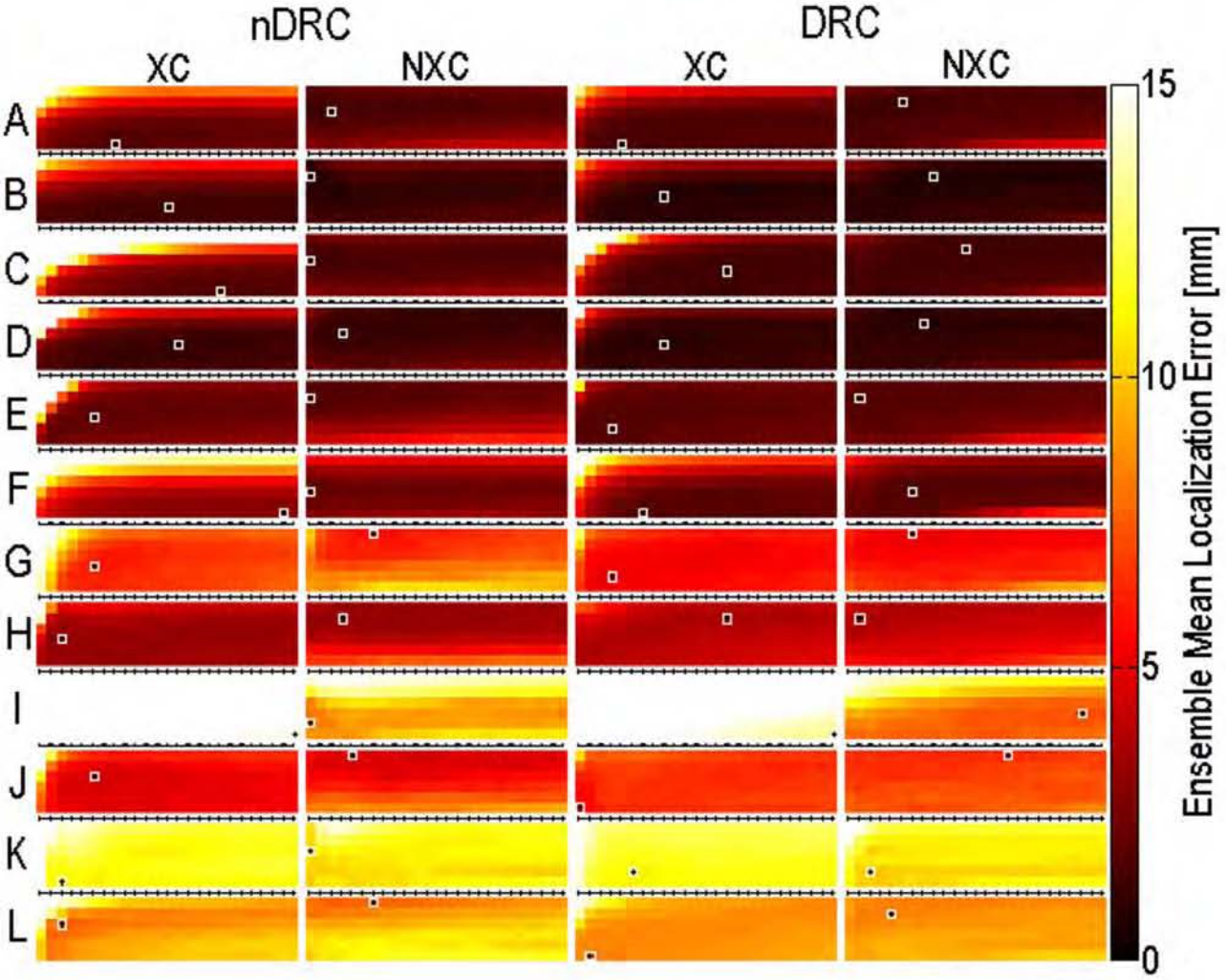
nDRC
DRC
XC
NXC
XC
NXC
A
B
C
D
E
F
G
H
I
J
K
L
15
10
5
0
Ensemble Mean Localization Error [mm]

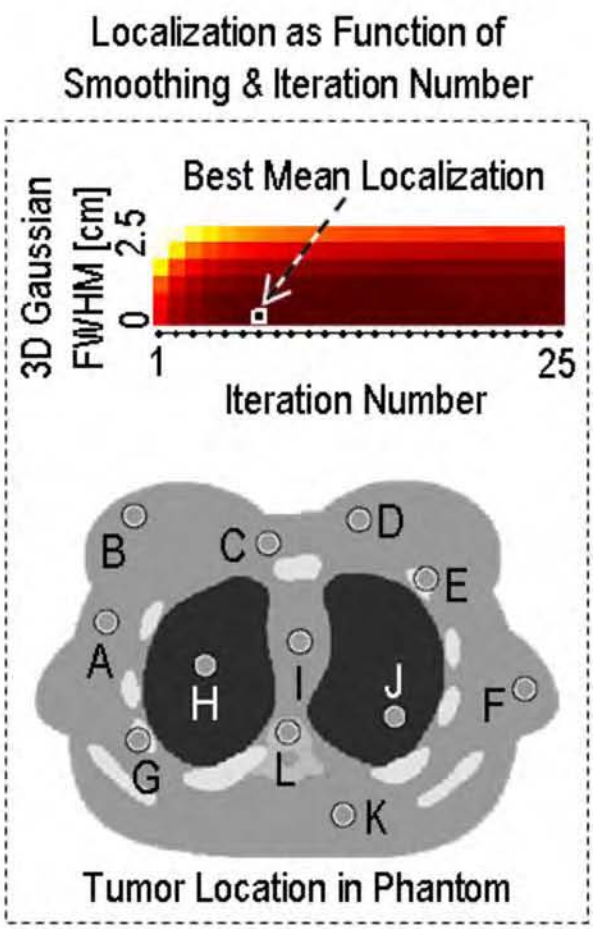
Localization as Function of
Smoothing & Iteration Number
3D Gaussian
FWHM [cm]
2.5
0
Best Mean Localization
1
25
Iteration Number
A
B
C
D
E
F
G
H
I
J
K
L
Tumor Location in Phantom

	Mean Localization Error [mm]				Optimal Smoothing: FWHM [cm]				Optimal Number of Iterations			
	nDRC		DRC		nDRC		DRC		nDRC		DRC	
Tumor	XC	NXC	XC	NXC	XC	NXC	XC	NXC	XC	NXC	XC	NXC
A	1.79	1.38	1.45	1.25	0.0	1.5	0.0	2.0	8	3	5	6
B	1.22	0.689	0.653	0.558	0.5	2.0	1.0	2.0	13	1	9	9
C	1.67	1.32	1.23	1.18	0.0	1.5	1.0	2.0	18	1	15	12
D	1.13	0.962	0.882	0.842	1.0	1.5	1.0	2.0	14	4	9	8
E	1.86	1.68	1.71	1.70	1.0	2.0	0.5	2.0	6	1	4	2
F	2.84	1.84	1.73	1.66	0.0	1.0	0.0	1.0	24	1	7	7
G	5.95	5.77	5.11	5.11	1.0	2.5	0.5	2.5	6	7	4	7
H	2.98	3.05	3.62	3.62	1.0	2.0	2.0	2.0	3	4	15	2
I	14.5	7.96	13.2	7.12	0.0	0.5	0.0	1.0	25	1	25	23
J	4.57	4.65	5.57	6.31	1.5	2.5	0.0	2.5	6	5	1	16
K	10.8	9.94	11.0	9.98	0.0	1.5	0.5	0.5	3	1	6	3
L	7.49	7.63	8.33	8.14	1.5	2.5	0.0	2.0	3	7	2	5
avg	4.73	3.91	4.54	3.96	0.63	1.8	0.54	1.8	11	3.0	8.5	8.3

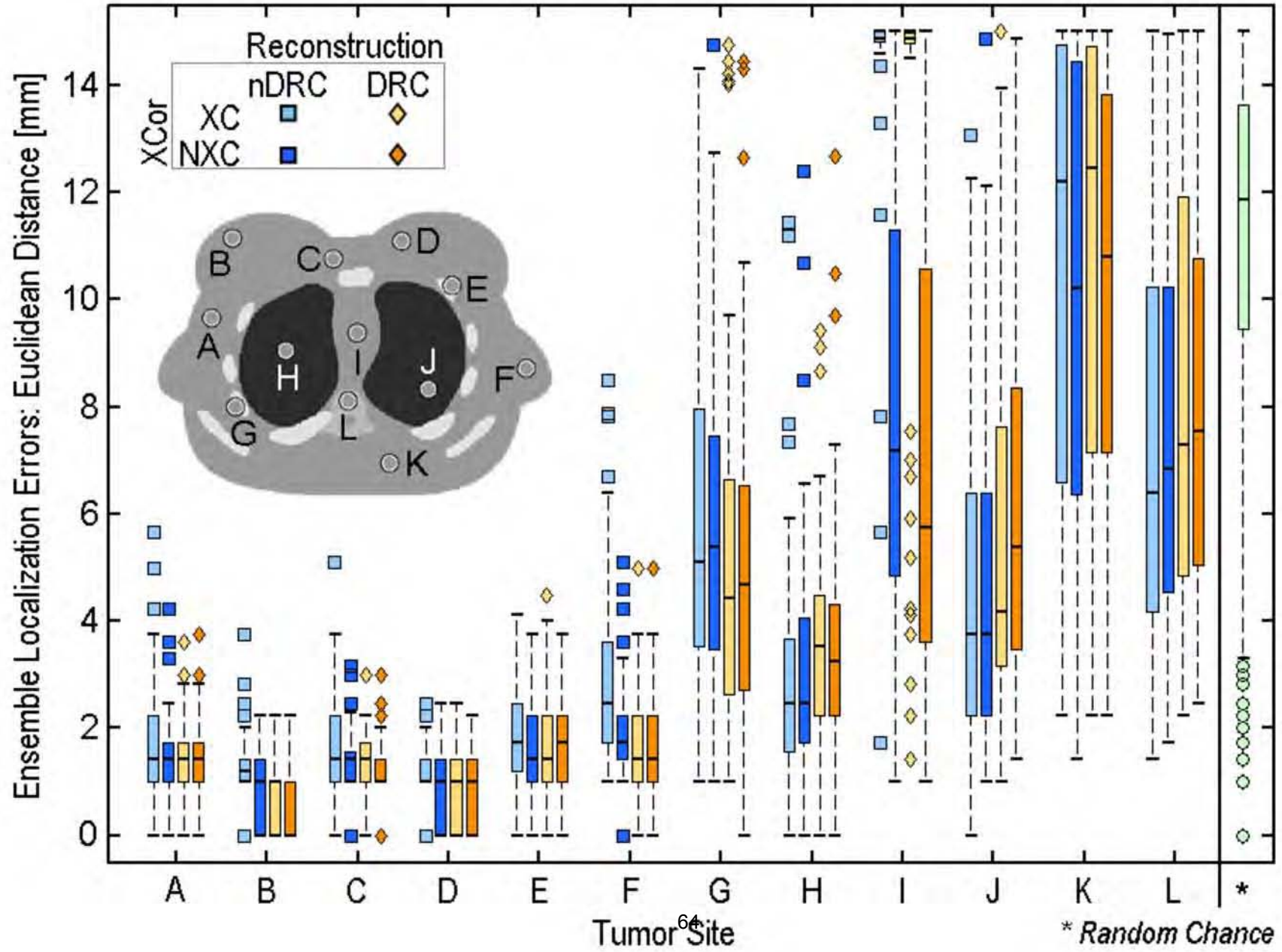
Reconstruction
nDRC
DRC
XCor
XC
NXC
Ensemble Localization Errors: Euclidean Distance [mm]
0
2
4
6
8
10
12
14
A
B
C
D
E
F
G
H
I
J
K
L
*
Tumor Site
* Random Chance

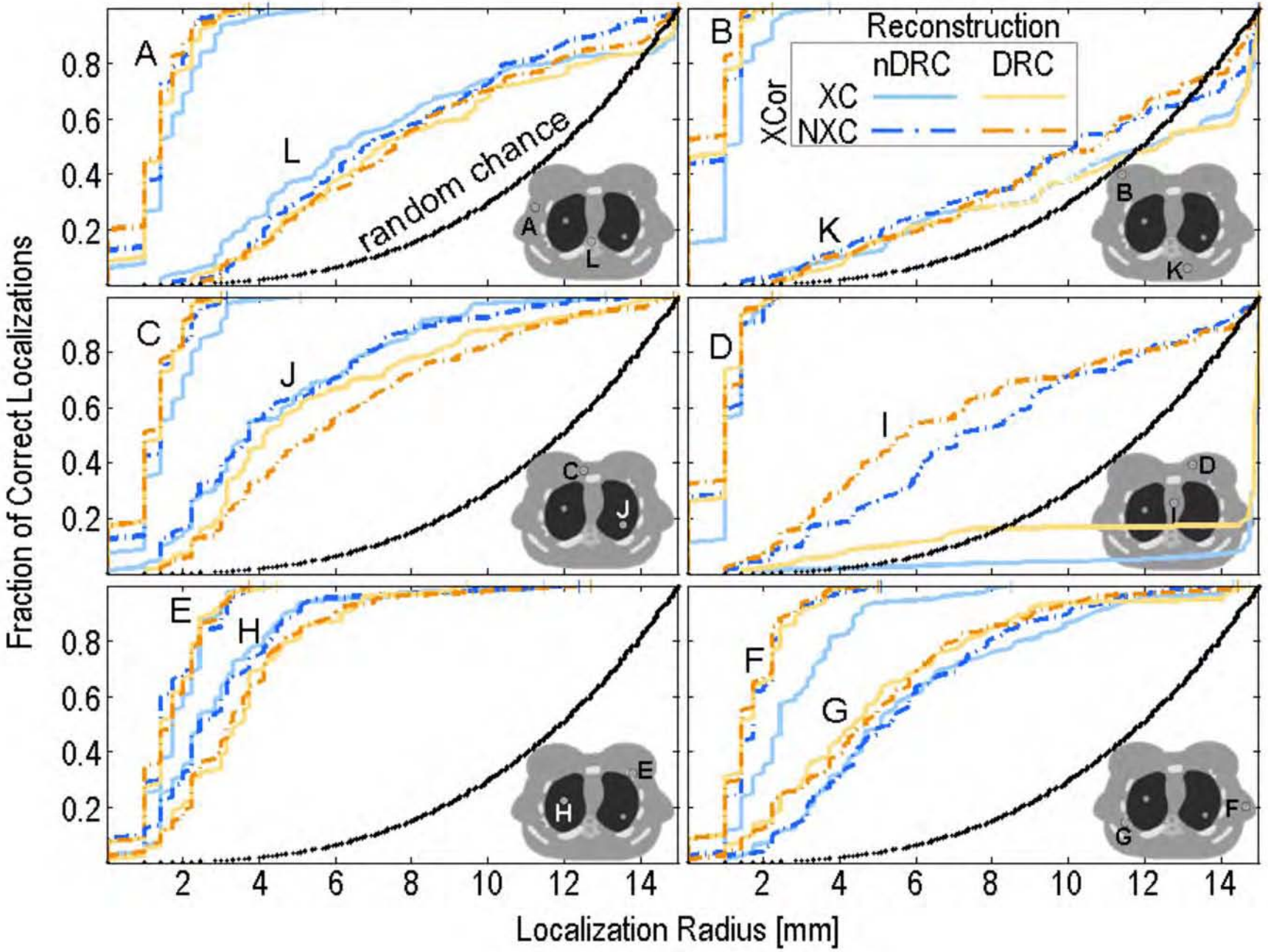
A
B
C
D
E
F
G
H
I
J
K
L
random chance
Reconstruction
nDRC
DRC
XCor
XC
NXC
Fraction of Correct Localizations
Localization Radius [mm]
0.2
0.4
0.6
0.8
2
4
6
8
10
12
14

			nDRC		DRC				nDRC		DRC	
			XC	NXC	XC	NXC			XC	NXC	XC	NXC
A	nDRC	XC	--				G	nDRC	XC	--			
		NXC	**1.3E-03**	--					NXC	8.2E-01	--		
	DRC	XC	**5.0E-04**	3.5E-01	--			DRC	XC	**4.4E-02**	**1.5E-02**	--	
		NXC	**3.2E-06**	1.5E-01	**8.9E-03**	--			NXC	**8.1E-03**	**1.2E-04**	7.6E-01	--
B	nDRC	XC	--				H	nDRC	XC	--			
		NXC	**5.7E-05**	--					NXC	3.8E-01	--		
	DRC	XC	**2.2E-07**	7.3E-01	--			DRC	XC	**2.4E-04**	**2.3E-04**	--	
		NXC	**2.7E-10**	2.0E-01	1.4E-01	--			NXC	**2.7E-05**	**1.8E-06**	7.8E-01	--
C	nDRC	XC	--				I	nDRC	XC	--			
		NXC	**7.4E-03**	--					NXC	**2.2E-14**	--		
	DRC	XC	**7.3E-05**	1.9E-01	--			DRC	XC	9.7E-02	**1.3E-10**	--	
		NXC	**3.8E-05**	7.6E-02	1.9E-01	--			NXC	**1.9E-14**	**2.3E-02**	**3.4E-12**	--
D	nDRC	XC	--				J	nDRC	XC	--			
		NXC	**2.4E-02**	--					NXC	8.6E-01	--		
	DRC	XC	**3.1E-03**	3.8E-01	--			DRC	XC	**7.8E-07**	**2.4E-03**	--	
		NXC	**5.9E-03**	2.1E-01	5.5E-01	--			NXC	**2.1E-08**	**1.7E-09**	**8.9E-03**	--
E	nDRC	XC	--				K	nDRC	XC	--			
		NXC	9.2E-02	--					NXC	**2.6E-03**	--		
	DRC	XC	**2.9E-02**	8.4E-01	--			DRC	XC	3.7E-01	1.0E-01	--	
		NXC	5.6E-02	7.7E-01	9.7E-01	--			NXC	**4.0E-02**	7.5E-01	**1.2E-02**	--
F	nDRC	XC	--				L	nDRC	XC	--			
		NXC	**6.2E-08**	--					NXC	1.2E-01	--		
	DRC	XC	**2.9E-09**	2.9E-01	--			DRC	XC	**2.9E-05**	**4.1E-03**	--	
		NXC	**3.6E-09**	**4.6E-02**	5.4E-01	--			NXC	**5.2E-03**	**2.0E-02**	6.1E-01	--

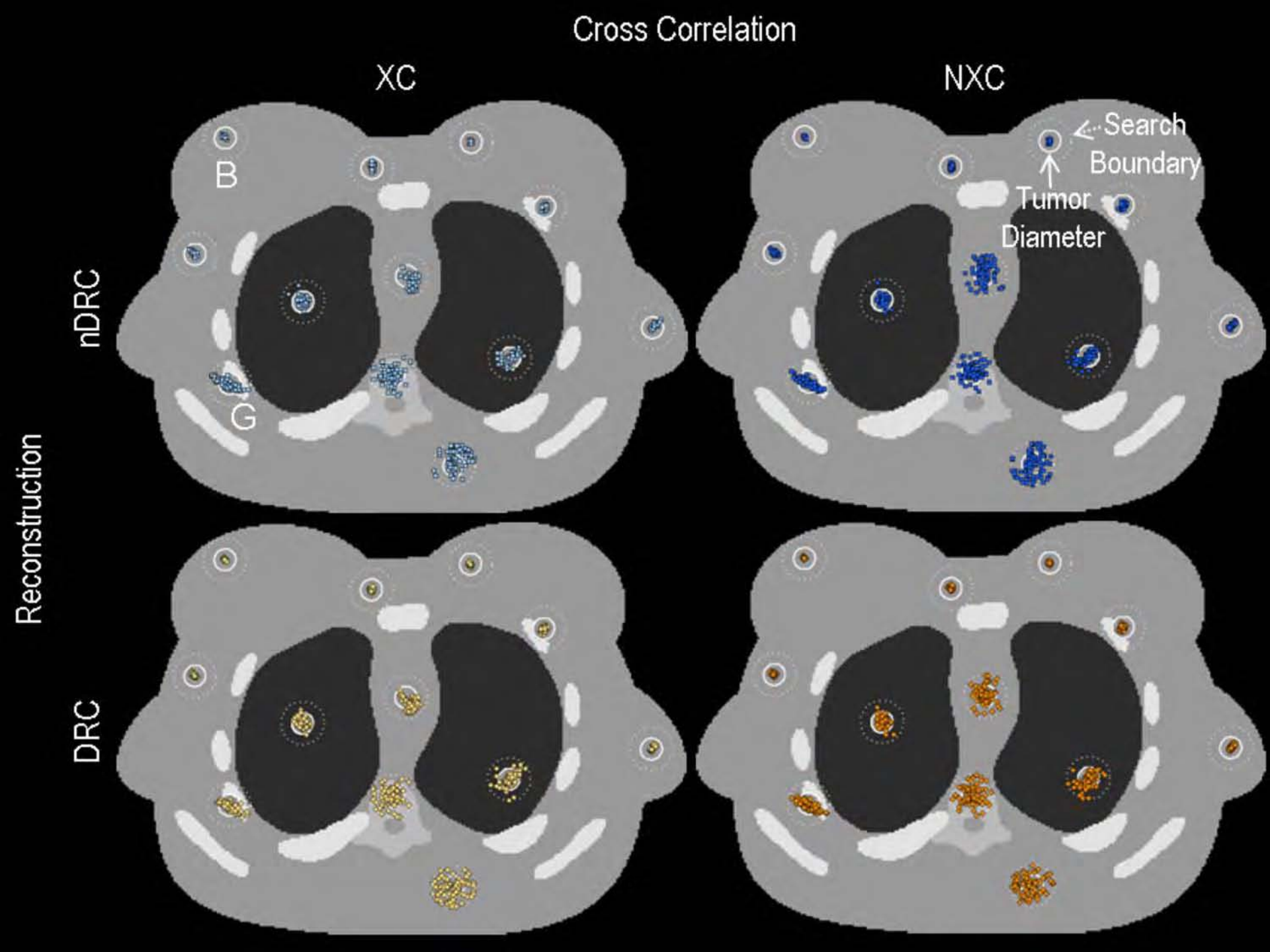
Cross Correlation
XC
NXC
Search
Boundary
Tumor
Diameter
B
G
nDRC
DRC
Reconstruction

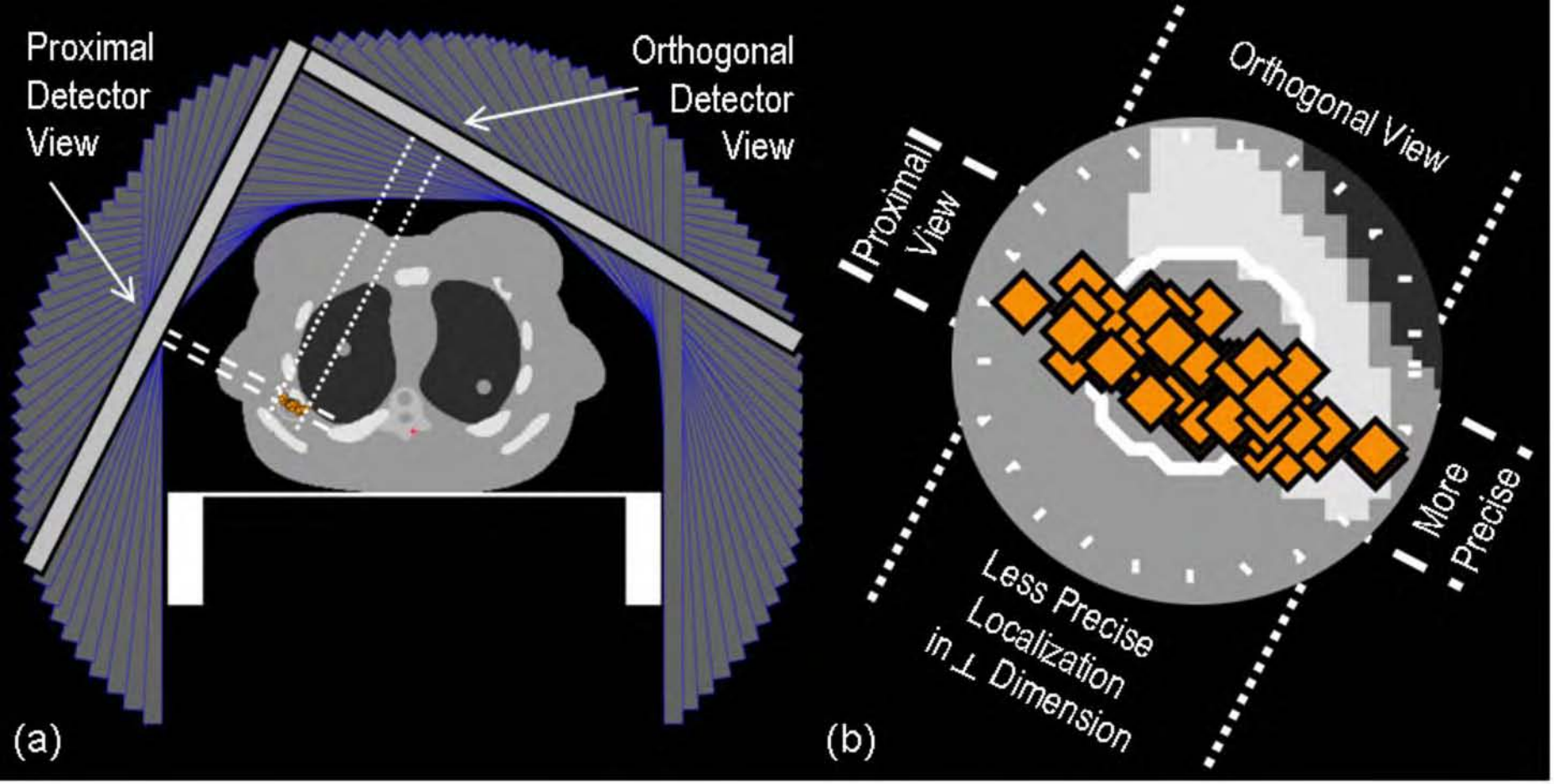
Proximal
Detector
View
Orthogonal
Detector
View
(a)
Orthogonal View
Proximal
View
More
Precise
Less Precise
Localization
in ⊥ Dimension
(b)

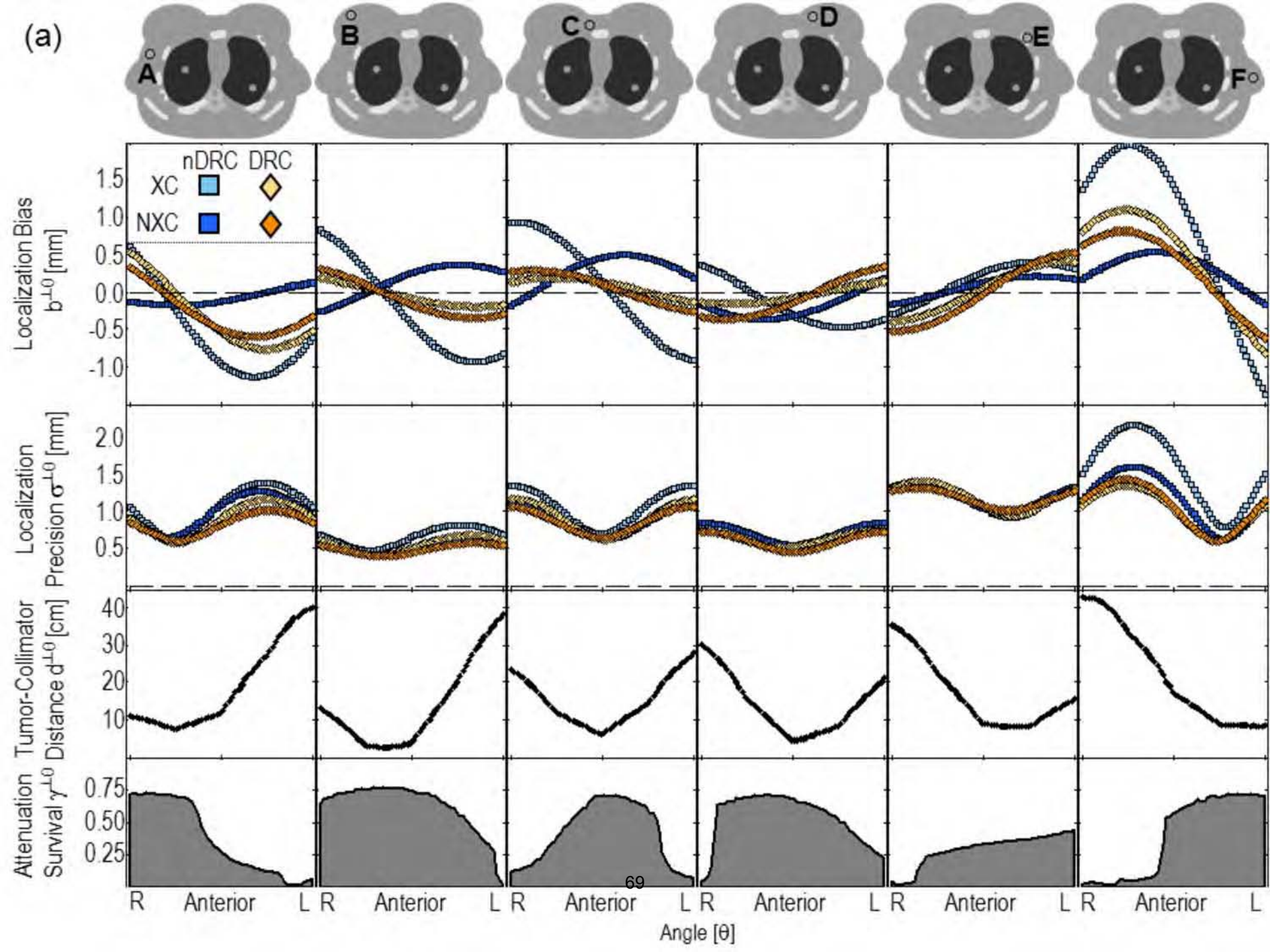
(a)
A
B
C
D
E
F
nDRC DRC
XC
NXC
Localization Bias $b^{\perp 0}$ [mm]
1.5
1.0
0.5
0.0
-0.5
-1.0
Localization Precision $\sigma^{\perp 0}$ [mm]
2.0
1.5
1.0
0.5
Tumor-Collimator Distance $d^{\perp 0}$ [cm]
40
30
20
10
Attenuation Survival $\gamma^{\perp 0}$
0.75
0.50
0.25
R Anterior L
Angle [θ]

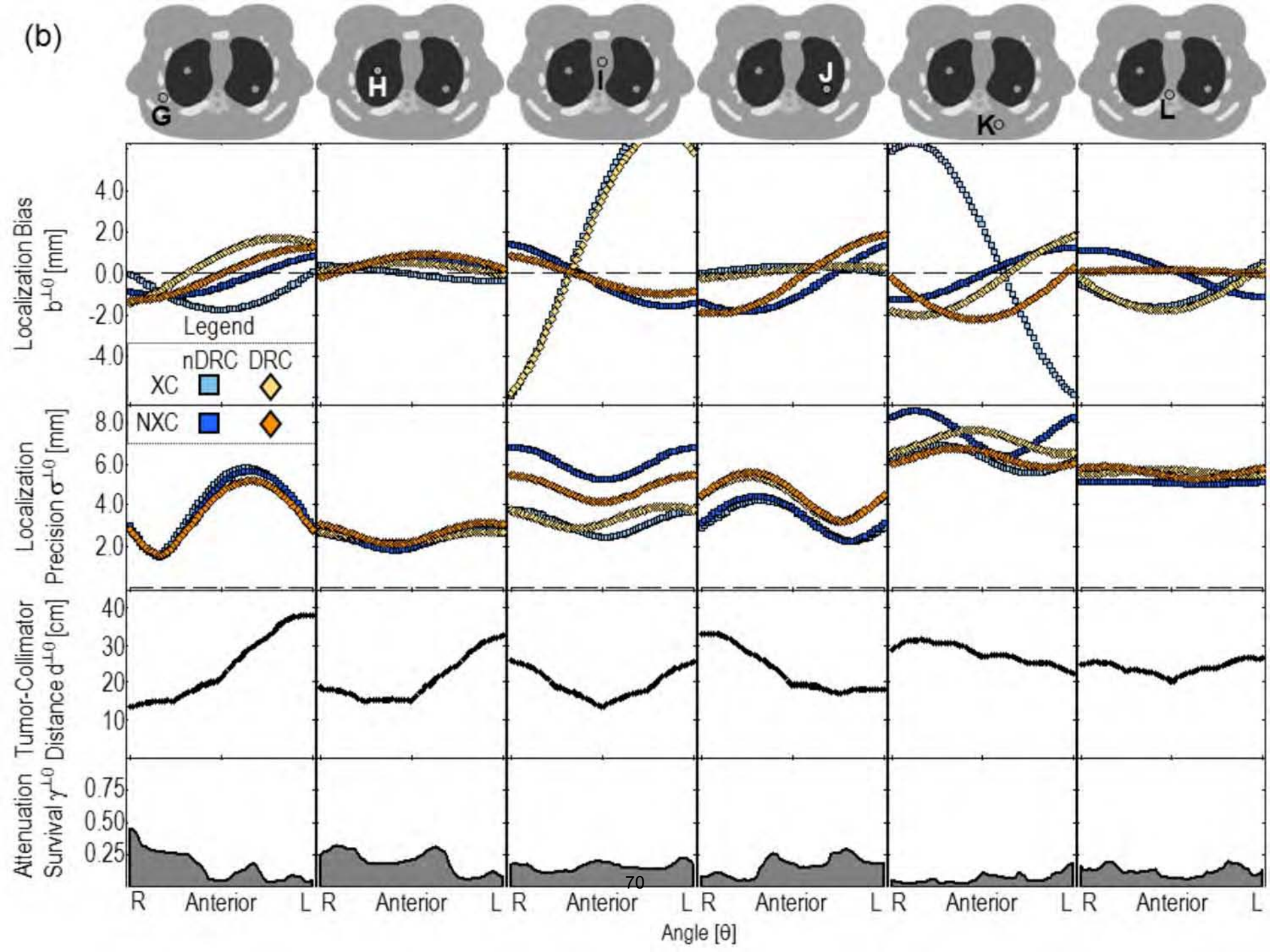
(b)
G
H
I
J
K
L
Localization Bias
b^⊥0 [mm]
4.0
2.0
0.0
-2.0
-4.0
Legend
nDRC DRC
XC
NXC
Localization
Precision σ^⊥0 [mm]
8.0
6.0
4.0
2.0
Tumor-Collimator
Distance d^⊥0 [cm]
40
30
20
10
Attenuation
Survival γ^⊥0
0.75
0.50
0.25
R
Anterior
L
Angle [θ]

	Avg. $d^{\perp\theta}$ [cm]	Avg. $\gamma^{\perp\theta}$		Avg. $d^{\perp\theta}$ [cm]	Avg. $\gamma^{\perp\theta}$
A	18.7	0.37	G	24.4	0.16
B	13.7	0.62	H	20.8	0.20
C	15.0	0.42	I	19.7	0.16
D	13.8	0.54	J	23.2	0.17
E	16.7	0.29	K	27.9	0.07
F	21.9	0.39	L	24.0	0.12
avg	16.6	0.44	avg	23.3	0.15

Appendix D

Quantitative Analysis of a Compact On-board SPECT Detector for ROI Reconstruction

JR Roper, JE Bowsher, FF Yin

Purpose: Single photon emission computed tomography (SPECT) imaging on-board radiation therapy machines may enhance radiation therapy. Use of a light-weight, compact detector would be desirable because of maneuverability, yet is challenged by truncation and consequently reconstruction artifacts. We hypothesize that, for a sizeable volume surrounding the tumor target, and with properly chosen detector trajectories, compact detectors can provide image quality that is comparable to that of full-size SPECT detectors.

Methods and Materials: On-board SPECT imaging was computer simulated for detectors with active surface widths of 21.2 and 40.0 cm. Detector trajectories were selected such that the common volume encompassed an 8-cm-diameter ROI surrounding each tumor in the torso of a NCAT phantom. For deep tumors, two common volumes – interior and partially exterior – were investigated. Radiotracer distribution was modeled for 99mTc-Sestamibi. Noise-free and noisy projection images were generated with an analytical simulator that models non-uniform attenuation, collimator & detector efficiency, and spatially-varying spatial resolution. Images were reconstructed by OSEM. In reconstructed images, root mean square error and recovered tumor activity were analyzed as a function of detector width and detector trajectory.

Results: Image truncation reduced overall image quality. For example, RMS error over an entire noise-free image slice was 18 – 35% worse with the 21-cm-wide detector versus the larger detector. However, for regions within the common volume for both detector widths, RMS errors differed by less that 2%. Similar results were observed for noisy images. Moreover, the recovered fraction of tumor activity was comparable, except for when the smaller-detector common volume was interior – the recovered activity was reduced by 11%.

Conclusions: Preliminary results show that an 8-cm-diameter ROI can be reconstructed using 21 or 40-cm-wide detectors with comparable RMS errors and recovered tumor activities, supporting the proposal that on-board target localization could be accomplished using compact SPECT detectors.

Appendix E

Are post-RT cardiac perfusion defects due to cardiac toxicity,
or are they artifacts from attenuation changes in surrounding soft tissues?

JR Roper, AA Manzoor, JB Bowsher, FF Yin, S-M Zhou, TZ Wong, S Borges-Neto, JL Hubbs, S Demirci, LB Marks.

Purpose: Following RT for left-sided breast cancer, perfusion defects (i.e. cold regions) are often noted on SPECT images. Almost all new defects are in the cardiac apex. Since SPECT is not absolutely quantitative, defects are detected by comparing regional intensities on pre-RT and post-RT images. Further, as SPECT images are not corrected for attenuation, and since RT may increase soft tissue density, apparent defects may be, at least partially, attributable to changes in attenuation of surrounding soft tissue. We herein perform a series of computer-based simulations to assess this possibility.

Methods: The perfusion tracer ^{99m}Tc-Sestamibi was simulated in a female NCAT phantom. Two tangential breast fields were considered: the deep border of one excluded the heart while a second included 2.5 cm of anterior heart. Within RT fields, tissue densities were increased in increments of 10% up to 50%. Noise-free images were simulated for a cardiac SPECT protocol – 180^{o} circular orbit, 60 views, parallel hole collimation – by modeling photon detection efficiency, distance-dependent spatial resolution, and non-uniform attenuation. Images were reconstructed without attenuation correction by OSEM (10 subsets, 20 iterations) onto a grid with 0.36 cm wide voxels. For varying degrees of change in soft tissue density, apparent reductions within the apex were noted, and compared with effects elsewhere. Simulations were repeated with the left (222 ml) breast removed to model mastectomy.

Results: As tissue density is increased by 10, 20, 30, 40, and 50%, corresponding reductions in apparent apical perfusion, for the different scenarios, are, respectively:

intact breast, 2.5 cm heart in field	13, 24, 34, 42, 50%;
intact breast, heart sparing	8, 15, 22, 28, 34%;
mastectomy, 2.5 cm heart in field	10, 19, 26, 34, 40%;
mastectomy, heart sparing	5, 9, 14, 18, 21%.

Changes in cardiac perfusion were not uniform; the apex was affected more than other areas.

Conclusion: RT-induced increases in soft-tissue attenuation can cause apparent changes in apical perfusion that might account for some of the defects seen clinically. However, the simulations also suggest that apparent defects should be seen even if the heart is excluded from the RT beam. Since perfusion defects are rarely seen in patients with no heart in the field, the possible changes in soft tissue attenuation/density are likely not the primary cause of perfusion defects seen clinically. Additional work is needed to understand the degree and impact of RT-induced soft tissue changes.

Appendix F

On-board SPECT Imaging: Improved Target Localization via Spatial Resolution Compensation

JR Roper, JE Bowsher, FF Yin

Purpose: Single photon emission computed tomography (SPECT) is being investigated for imaging on-board radiation therapy machines to localize biological targets. SPECT spatial resolution degrades as distance increases between the detector and radiotracer, an effect of collimation which results in spatially-varying, asymmetric blurring. Here we assess localization accuracy in noisy images that were reconstructed with and without spatial resolution compensation.

Methods: Uptake of ^{99m}Tc-Sestamibi was simulated in a female NCAT phantom. Twenty, 1.4-cm-diameter biological targets were simulated in the torso. Target activity ratios were 3:1 and 6:1 relative to a background concentration of 0.25 μCi/ml. Spatially-varying spatial resolution was modeled in projection images for a half-circular anterior orbit. An ensemble of 25 noisy projection images was degraded with Poisson noise to simulate 8 minute scans. Images were reconstructed using 10-subset, 5-iteration OSEM with and without spatial resolution compensation. Compensation involved tracing cones of 49 rays through the collimator acceptance angle, as opposed to tracing 1 central ray. Nonprewhitening matched filters were used to measure target centroids within 3D, 2.9-cm-diameter search volumes. Localization accuracy was calculated as the mean distance between measured and true target centroids over the ensemble.

Results: Localization accuracy was less than 4 mm for 6 targets using either reconstruction method. For these targets, spatial resolution compensation always improved localization accuracy. On average, localization accuracy improved from 2.5 mm to 1.9 mm. The maximum improvement was 1 mm. With spatial resolution compensation, two targets were localized with 1 mm accuracy.

Conclusion: Preliminary results show improved localization in on-board SPECT images with spatial resolution compensation during reconstruction. These findings are important for assessing the feasibility of on-board SPECT imaging and warrant further investigation.

Appendix G

On-board SPECT: Localization Study using Scanner-acquired Data

JR Roper, JM Wilson, JE Bowsher, TG Turkington, FF Yin

Purpose: In previous computer-simulation studies we have shown that on-board SPECT imaging is a promising approach to localizing biological structure. The purpose of this study is to investigate SPECT localization using scanner-acquired data.

Method and Materials: A torso phantom was filled with 0.75μCi/ml of ^{99m}Tc. Five targets (A-E) of 6:1 activity ratio – diameters of 22 to 34mm – were positioned in phantom. SPECT data were acquired with one Trionix Triad detector. The product of activity and 1.5-minute count time models a 4.5-minute clinical scan. Ensembles of 10 images were reconstructed using MLEM for 3 detector trajectories: 360^o, 180^o left lateral, and 180^o right lateral. Localization was assessed across the noisy ensembles using non-prewhitening observers that were forced to select the most suspicious target location from a 3.6-cm diameter search region centered on target. True centroids were derived from a 12-hour SPECT scan that registered with CT to within 1/3mm. Localization error was calculated as the distance between true and measured centroids. Significance was assessed with the Wilcoxon rank sum test.

Results: Mean localization errors for targets (A-E) are A) 0.80mm, B) 1.2mm, C) 1.9mm, D) 1.2mm, and E) 0.90mm using the 180^o trajectory more proximal to each target. With the 360^o trajectory, mean errors are A) 1.3mm, B) 1.3mm, C) 2.1mm, D) 2.2mm, and E) 1.5mm. Differences between the above 180^o and 360^o trajectories are significant ($p < 0.05$) at A, D, and E. Mean error is typically much worse using the more distal 180^o trajectory: A) 4.5mm, B) 3.1mm, C) 2.8mm, D) 4.4mm, and E) 6.9mm.

Conclusion: This study, using scanner-acquired SPECT data, demonstrates mean localizations to within 1 or 2mm with 4.5-minute scans. The study also shows that detector trajectory can substantially affect target localization and should be optimized for specific target sites.